

## Topical Review

# Recent progress in bio-inspired macrostructure array materials with special wettability—from surface engineering to functional applications

Zhongxu Lian<sup>2,3,5,\*</sup> , Jianhui Zhou<sup>2,3</sup>, Wanfei Ren<sup>2,3</sup>, Faze Chen<sup>4</sup> , Jinkai Xu<sup>2,3</sup> , Yanling Tian<sup>5</sup> and Huadong Yu<sup>1,\*</sup> 

<sup>1</sup> School of Mechanical and Aerospace Engineering, Jilin University, Changchun 130022, People's Republic of China

<sup>2</sup> Ministry of Education Key Laboratory for Cross-Scale Micro and Nano Manufacturing, Changchun University of Science and Technology, Changchun 130022, People's Republic of China

<sup>3</sup> College of Mechanical and Electrical Engineering, Changchun University of Science and Technology, Changchun 130022, People's Republic of China

<sup>4</sup> School of Mechanical Engineering, Tianjin University, Tianjin 300350, People's Republic of China

<sup>5</sup> School of Engineering, University of Warwick, Coventry CV4 7AL, United Kingdom

E-mail: [lianzhongxu@cust.edu.cn](mailto:lianzhongxu@cust.edu.cn) and [yuhd@jlu.edu.cn](mailto:yuhd@jlu.edu.cn)

Received 11 May 2023, revised 7 July 2023

Accepted for publication 17 October 2023

Published 10 November 2023



CrossMark

## Abstract

Bio-inspired macrostructure array (MAA, size: submillimeter to millimeter scale) materials with special wettability (MAAMs-SW) have attracted significant research attention due to their outstanding performance in many applications, including oil repellency, liquid/droplet manipulation, anti-icing, heat transfer, water collection, and oil–water separation. In this review, we focus on recent developments in the theory, design, fabrication, and application of bio-inspired MAAMs-SW. We first review the history of the basic theory of special wettability and discuss representative structures and corresponding functions of some biological surfaces, thus setting the stage for the design and fabrication of bio-inspired MAAMs-SW. We then summarize the fabrication methods of special wetting MAAs in terms of three categories: additive manufacturing, subtractive manufacturing, and formative manufacturing, as well as their diverse functional applications, providing insights into the development of these MAAMs-SW. Finally, the challenges and directions of future research on bio-inspired MAAMs-SW are briefly addressed. Worldwide efforts, progress, and breakthroughs from surface engineering to functional applications elaborated herein will promote the practical application of bio-inspired MAAMs-SW.

\* Authors to whom any correspondence should be addressed.



Original content from this work may be used under the terms of the [Creative Commons Attribution 4.0 licence](https://creativecommons.org/licenses/by/4.0/). Any further distribution of this work must maintain attribution to the author(s) and the title of the work, journal citation and DOI.

Keywords: macrostructure arrays, superhydrophobic, 3D printing, laser, droplet manipulation

## 1. Introduction

Natural and artificial objects exist across different scales, encompassing macroscopic, microscopic, and nanoscale dimensions (figure 1) [1–9]. Depending on their sizes, the structures of solid surfaces can be divided into these three scales, specifically, macrostructures, microstructures, and nanostructures. Recently, biological structures have served as inspiration for designing artificial structures with specific characteristics [10–16]. Inspired by lotus leaves, cicada wings, mosquito compound eyes, butterfly wings, water strider legs, fish scales, shark skin, red rose petals, and gecko feet [17–30], wettable surfaces with micro/nanostructure arrays (size: 1 nm–100  $\mu\text{m}$ ) have drawn significant attention from researchers. Numerous research results have been reported on methods for fabricating wettability surfaces with micro/nanostructure arrays [31–38]. Due to their structural characteristics, these surfaces demonstrate excellent performance across various domains, including superwettability [10, 37, 39–41], anti-reflection [42, 43], anti-fogging [44, 45], anti-icing [46–49], heat transfer [50, 51], liquid/droplet/bubble manipulation [16, 52–55], anti-fouling [56, 57], drag reduction [58], oil–water separation [59, 60], fog collection [61–63], anti-bacterial properties [64, 65], and blood repellency [66].

In addition to micro/nanostructure arrays, many biological surfaces contain macrostructure arrays (MAAs), spanning from 100  $\mu\text{m}$  to a few millimeters (submillimeter and millimeter scales). Examples include rice leaves, *Salvinia* leaves, desert beetle elytra, cacti, pine needles, and *Araucaria* leaves [26, 67–71]. Inspired by macrostructures and micro/nanostructures found in nature [72–75], researchers have developed numerous macrostructure array materials with special wettability (MAAMs-SW) [76–85] and revealed that these surfaces can achieve comparable performance to micro/nanostructure arrays in various fields, such as oil repellency [79, 80], liquid/droplet manipulation [16, 86], anti-icing [87, 88], heat transfer [89], water collection [90, 91], oil–water separation [92, 93], drag reduction [94, 95], air retention under water [96], smart wettability [97], and mechanical stability [98]. MAAMs-SW exhibit superior performance across various fields. For example, macro groove arrays inspired by rice leaves display distinct anisotropic characteristics, conferring unique advantages for droplet manipulation [86]. Convex millimeter-sized surface structures can promote condensation, resulting in an improved water collection performance [90]. In anti-icing applications, superhydrophobic surfaces with macro post or stripe arrays can greatly reduce the contact time between the droplets and the surface, preventing droplets from freezing before detaching from the surface [99, 100]. In oil–water separation processes, traditional microporous or nanoporous meshes/membranes with special wettability will be prone to blockage when separating a high-viscosity oil and water mixture. However, cactus-inspired

macro needle arrays can avoid this problem [92]. In terms of mechanical stability, an MAA consisting of an interconnected frame acting as ‘armor’ can provide protection against the deterioration of water repellency for fragile superhydrophobic nanostructures/coatings [98]. Notably, many studies describe structures with sizes of 100–1000  $\mu\text{m}$  as microstructures. In the present review, we classify these structures as macrostructures. Despite demonstrating superior performance in many fields, the development of bio-inspired MAAMs-SW still faces challenges. Specifically, these MAAMs-SW cannot be fully utilized in practical applications due to possible limitations, such as a lack of ideal design and optimization, industrial fabrication strategies, and mechanical durability. Therefore, it is imperative to provide guidance for researchers, learn from nature, and even surpass nature to design ideal MAAMs-SW, as well as develop efficient and green methods for scalable and large-area fabrication.

Many studies on bio-inspired MAAMs-SW have been published. However, systematic reviews regarding bio-inspired MAAMs-SW have been rarely reported. In this review, we have compiled and classified current research findings to comprehensively cover the recent research in the theory, design, fabrication, and application of bio-inspired MAAMs-SW (figure 2). We first briefly discuss the fundamentals of special wettability, and then review natural biological surfaces with representative structures, providing a framework for guiding the design of bio-inspired MAAMs-SW. Next, we summarize three fabrication approaches for special wetting MAAs, namely, (1) additive manufacturing (three-dimensional (3D) printing), (2) subtractive manufacturing (laser etching, wire electrical discharge machining, micro-mechanical cutting machining, and electrochemical machining), and (3) formative manufacturing (template and imprinting methods), and compare the main advantages and limitations of each strategy. We then demonstrate the potential applications of MAAMs-SW, and finally, we discuss the challenges and directions for the future design of MAAMs-SW. We intend to provide researchers with a broader and deeper understanding by outlining these advances and providing our perspectives to pave the way for the practical application of bio-inspired MAAMs-SW.

## 2. Theoretical basis

Surface wettability refers to the ability of a liquid to spread on a solid surface, representing an important surface attribute. Distinct wettability characteristics form when surfaces are endowed with special structures or chemical compositions. The fundamental principles of wettability offer insights into elucidating the underlying mechanism responsible for special wettability. Therefore, in this section, we introduce typical wetting theories (including the Young’s equation, Wenzel model, Cassie–Baxter model, and Re-entrant model) and basic

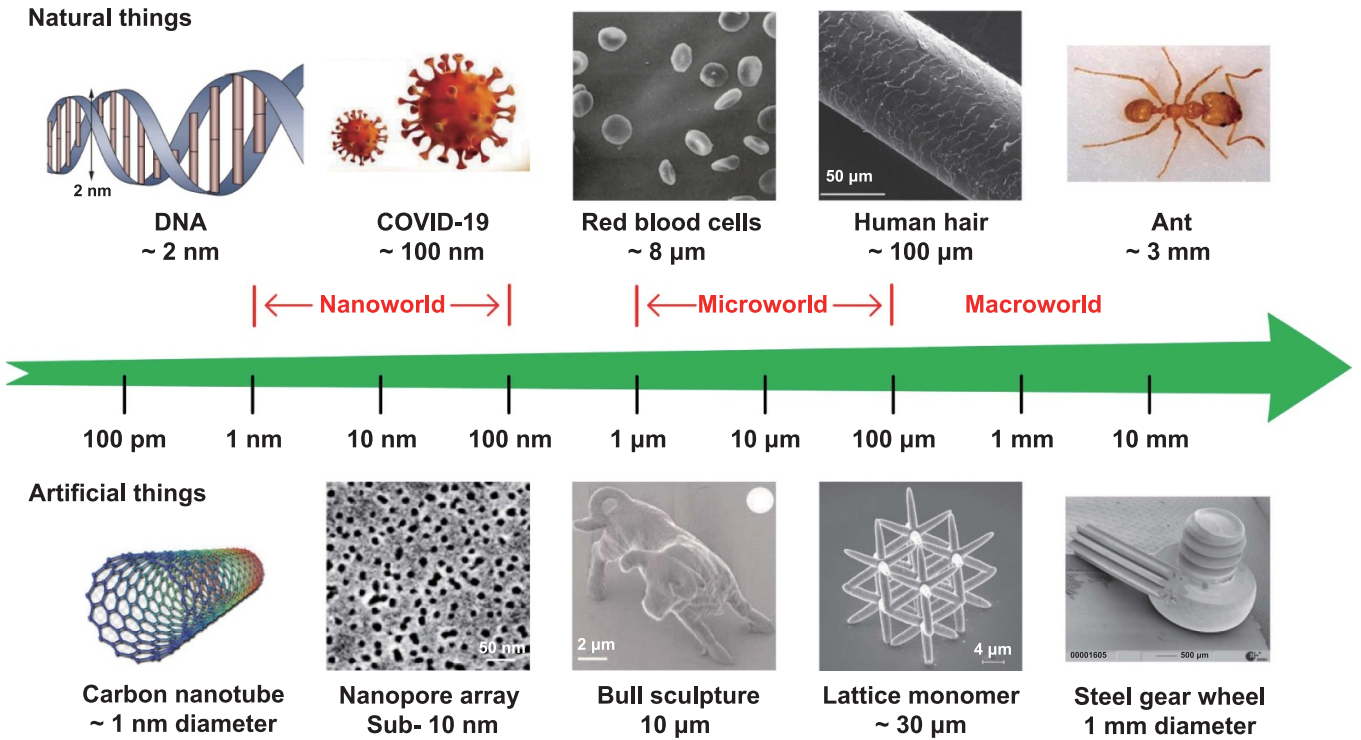


**Figure 1.** Object scales. DNA, ant, and bull sculpture: Reproduced from [1, 4, 7], with permission from Springer Nature. Red blood cells and steel gear wheel: Reproduced from [2, 9], with permission from Springer Nature. Human hair and carbon nanotube: Reproduced from [3, 5]. CC BY 4.0. Reproduced from [6, 8]. The Author(s). CC BY 4.0.

theories of special wetting behaviors (including surface energy gradients and Laplace pressure differences).

### 2.1. Typical wetting theories

**2.1.1. Young's equation and contact angle.** In 1805, Young [101] proposed the wetting theory of droplets on smooth solid surfaces. For an ideal smooth solid surface, a solid–liquid–gas three-phase system will form when a droplet comes into contact with the surface (figure 3(a)). In a three-phase system in equilibrium, Young's equation can be obtained by balancing the surface tensions in the horizontal direction:

$$\gamma_{sg} = \gamma_{sl} + \gamma_{gl} \times \cos \theta_Y, \quad (1)$$

where  $\gamma_{sg}$ ,  $\gamma_{sl}$ , and  $\gamma_{gl}$  represent the surface tensions of the solid–gas, solid–liquid, and gas–liquid interfaces, and  $\theta_Y$  is the intrinsic contact angle of the solid surface. The intrinsic contact angle  $\theta_Y$  can be expressed by:

$$\cos \theta_Y = \frac{\gamma_{sg} - \gamma_{sl}}{\gamma_{gl}}. \quad (2)$$

Young's equation suggests that the contact angle  $\theta_Y$  depends on the surface tension. For the contact angle  $\theta_Y$  of a water droplet, the boundary between hydrophilic and hydrophobic is  $90^\circ$ . A surface can be classified as hydrophilic when  $\theta_Y < 90^\circ$  and hydrophobic when  $\theta_Y > 90^\circ$ . Currently, a maximum contact angle of water droplets on a smooth surface

is approximately  $130^\circ$  [102]. Notably, with a contact angle of less than  $10^\circ$ , the surface is considered superhydrophilic, and with a contact angle of greater than  $150^\circ$ , the surface is considered superhydrophobic [12]. Comparable terms can be applied to oils, with corresponding terms of superoleophilic, oleophilic, oleophobic, and superoleophobic [103].

**2.1.2. Wenzel model.** Although Young proposed the contact angle theory for smooth surfaces, actual solid surfaces are not ideal smooth surfaces and instead possess varying degrees of roughness. Consequently, in 1936, Wenzel [104] introduced the geometric parameters of roughness into the analysis of the surface wettability. Wenzel's equation is given by:

$$\cos \theta_w = r \frac{\gamma_{sg} - \gamma_{sl}}{\gamma_{gl}} = r \cos \theta_Y \quad (3)$$

and

$$r = S_a / S_b, \quad (4)$$

where  $\theta_w$  represents the apparent contact angle,  $r$  is the roughness factor,  $S_a$  denotes the actual surface area of the rough structure on the material surface, and  $S_b$  is the projected area. In the Wenzel state, the droplet completely fills the rough surface structure (figure 3(b)). Because  $r$  will always be greater than 1, roughness will amplify the wetting and non-wetting behavior of rough surfaces in the Wenzel state. As a result, roughness makes hydrophilic surfaces more hydrophilic and hydrophobic surfaces more hydrophobic.

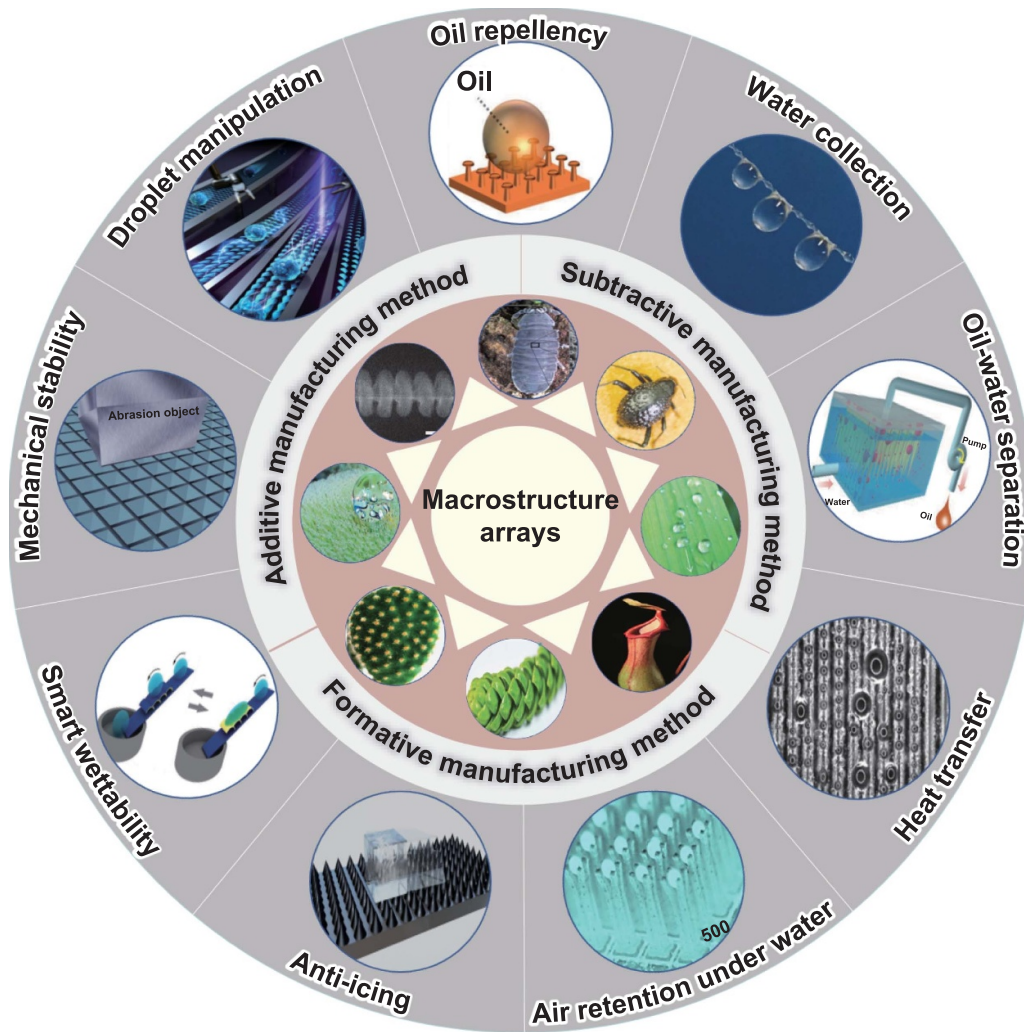


**Figure 2.** Schematic summary of bio-inspired MAAMs-SW, as well as their fabrication strategies and applications. Rice leaves: Reproduced from [26] with permission from the Royal Society of Chemistry. Droplet manipulation, Salvinia leaves, oil–water separation, and smart wettability: Reproduced from [16]. CC BY 4.0. [67] John Wiley & Sons. Copyright © 2010 WILEY-VCH Verlag GmbH & Co. KGaA, Weinheim. [93] John Wiley & Sons. © 2022 Wiley-VCH GmbH. [97] John Wiley & Sons. © 2019 WILEY-VCH Verlag GmbH & Co. KGaA, Weinheim. Desert beetle elytra, cactus, spider silk, *Nepenthes alata*, and mechanical stability: Reproduced from [68, 69, 73, 74, 98], with permission from Springer Nature. Springtail skin and water collection: Reproduced from [72, 91]. CC BY 4.0. Araucaria leaves: From [71]. Reprinted with permission from AAAS. Oil repellency and heat transfer: Reprinted from [80], © 2020 Elsevier Ltd. All rights reserved. Reprinted from [89], © 2020 Elsevier B.V. All rights reserved. Air retention under water: Reprinted with permission from [96]. Copyright (2022) American Chemical Society.

**2.1.3. Cassie–Baxter model.** The Wenzel model, which is only valid for the complete infiltration of droplets into a surface structure, cannot elucidate excellent water repellency in nature. In 1944, Cassie and Baxter [105] suggested a composite contact model to investigate the wettability of rough surfaces (figure 3(c)). The formed composite contact interface was composed of a solid–liquid interface and a gas–liquid interface. The apparent contact angle of a rough surface in this state can be described by:

$$\cos \theta_{CB} = f_1 \cos \theta_1 + f_2 \cos \theta_2, \tag{5}$$

where  $\theta_{CB}$  is the apparent contact angle under the Cassie–Baxter model,  $\theta_1$  is the contact angle of the smooth surface,  $\theta_2$  denotes the intrinsic contact angle between the liquid and air

( $180^\circ$ ), and  $f_1$  and  $f_2$  represent the area fractions of the solid–liquid interface and the gas–liquid interface in the composite contact interface ( $f_1 + f_2 = 1$ ), respectively. This equation can also be written as:

$$\cos \theta_{CB} = f_1 (\cos \theta_1 + 1) - 1. \tag{6}$$

The Cassie–Baxter model signifies that if the area fraction of the solid–liquid interface is sufficiently low, an apparent contact angle  $\theta_{CB}$  with much greater than  $90^\circ$  can be obtained. Hence, the formation of the Cassie–Baxter state may lead to the realization of superhydrophobicity. In addition, surfaces with a lower area fraction of the solid–liquid interface in the Cassie–Baxter state show low adhesion for droplets. Therefore, ensuring that droplets are in the Cassie–Baxter state on rough surfaces is critical for designing superhydrophobic



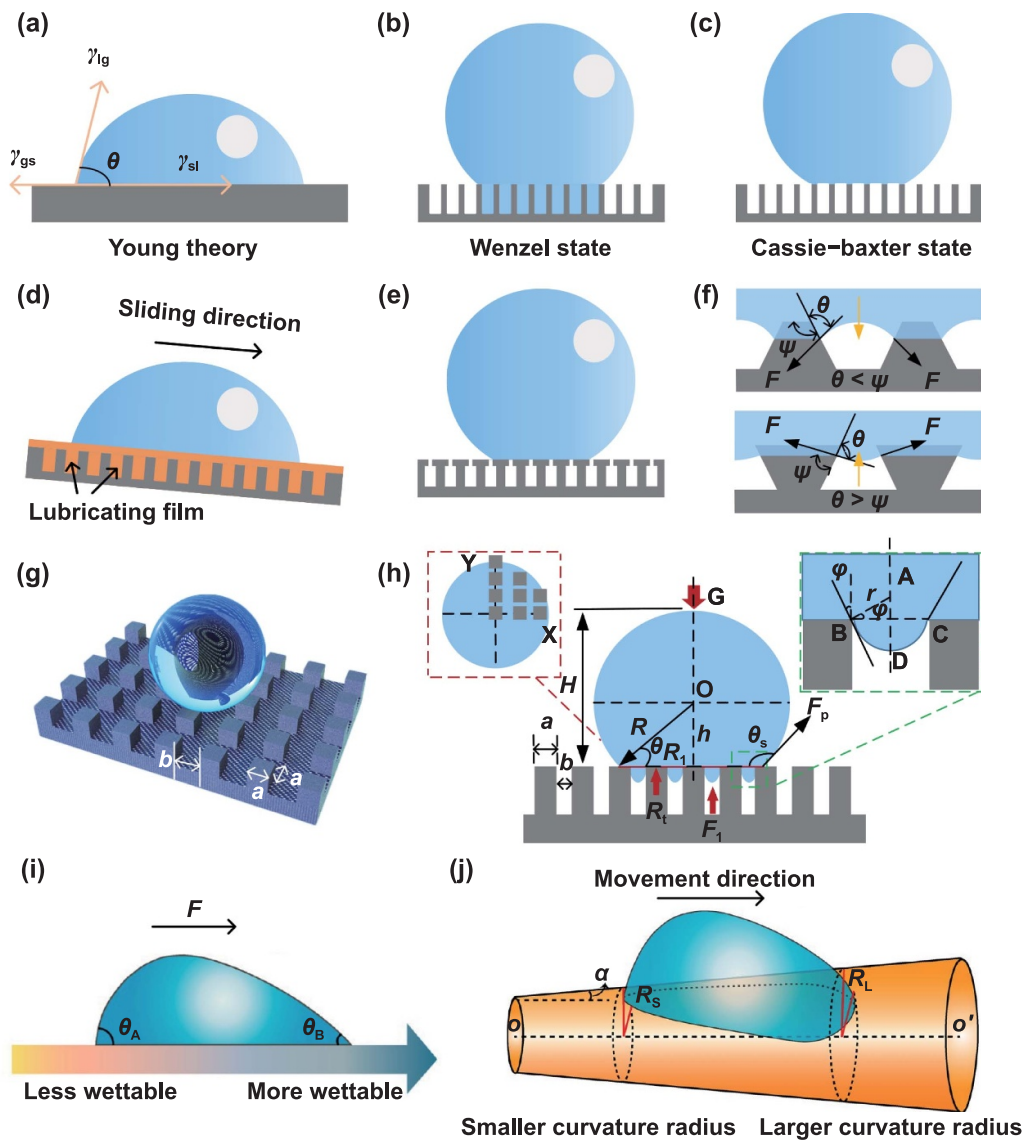


**Figure 3.** Theoretical basis of special wettability. (a) Young’s theory. (b) Wenzel state. (c) Cassie–Baxter state. (d) Sliding behavior of a droplet on a slippery liquid infused porous surface. (e) Cassie–Baxter state on a rough surface with a re-entrant topography. (f) Wetting behavior of a droplet on trapezoidal and inverted trapezoidal structures. (g) Droplet resting on a macro square pillar array. (h) Diagram showing the force analysis of a droplet on the macro square pillar array. (i) Driving force arising from a surface energy gradient. (j) Laplace pressure difference on a convex surface with a cone structure. (i) and (j) Reprinted with permission from [109]. Copyright (2014) American Chemical Society.

surfaces with a high contact angle and a low sliding angle. As a typical surface with special wettability, a recently developed slippery liquid infused porous surface by Wong *et al* [106] had a low sliding angle, however, its water repellency mechanism was difficult to describe using the Wenzel and Cassie–Baxter models. The slippery liquid infused porous surface was formed by injecting lubricating oil with a low surface energy to form a smooth and stable interface and reduce the adhesion of most liquids (figure 3(d)).

**2.1.4. Critical role of the re-entrant topography.** In reality, the complexities of wetting phenomena are not as straightforward as described in these theories. A transition state between the Cassie–Baxter state and the Wenzel state will

often occur. Studies have demonstrated that the stability of the Cassie–Baxter state largely depends on the surface morphology. Therefore, to achieve a stable Cassie–Baxter state, the re-entrant topography is often introduced during the design and fabrication process of a rough surface (figure 3(e)). In addition, the re-entrant topography can lead to a Cassie–Baxter state with low-surface-tension liquids (such as oil, alcohol, or other organic solvents). Tuteja *et al* [107, 108] first proposed that the re-entrant topography could play a pivotal role in fabricating superoleophobic surfaces. To illustrate the critical role of the re-entrant topography, the contact behaviors of droplets with a trapezoidal structure (structural angle  $\psi > 90^\circ$ ) and an inverted trapezoidal structure (re-entrant topography, structural angle  $\psi < 90^\circ$ ) were analyzed (figure 3(f)). The structural surface generated a stable Cassie–Baxter state only when

$\psi > \theta$  (Young's contact angle). If  $\psi < \theta$ , a downward traction force was generated at the gas–liquid interface under the action of a capillary force, prompting the droplet to fill the rough surface structure and form a Wenzel state. Therefore, designing a reasonable re-entrant topography on the surface can not only improve the stability of the superhydrophobicity but also be used to construct superoleophobic surfaces.

**2.1.5. Mathematical model for contact angle on MAAs.** The contact angles ( $\theta_s = \theta + 90^\circ$ ) of droplets resting on surfaces with MAAs can be predicted by a mathematical model. For this discussion, a macro square pillar array was adopted. Figure 3(g) shows the droplet resting on a macro square pillar array, where  $a$  is the width of each square pillar, and  $b$  is the gap width between the pillars. To simplify the model, the following assumptions were made:

1. The macro pillar structures were evenly distributed, and the sizes and shapes of each pillar structure were identical.
2. The state of the droplet on the pillar array was an ideal Cassie–Baxter state.
3. The radius of the droplet resting on the pillar array remained constant.
4. The projection area where the droplet contacted the pillar array was circular.
5. The surface without the macro square pillar arrays was hydrophobic.
6. The weight of the droplet was evenly distributed over the projection area.
7. The droplet did not penetrate between the pillars.
8. The cohesion inside the droplet was a constant value.

The droplet remained in equilibrium on the square pillar array. Therefore, based on a force balance method, the different forces supporting the weight  $W$  of the droplet can be expressed by:

$$W = R_t + F_1 + F_p \cos \theta, \quad (7)$$

where  $R_t$  is the reaction force supplied by the pillars,  $F_p$  represents the peripheral surface tension force,  $F_1$  is the surface tension caused by the droplet sagging between pillars, and  $\theta$  represents the angle between  $R$  and  $R_1$  (figure 3(h)).

The weight  $W$  of the droplet can be expressed as:

$$W = (\text{Volume of droplet}) \times \rho g = \left(\frac{4}{3}\pi R^3\right) \rho g, \quad (8)$$

where  $R$  represents the radius of the spherical droplet,  $\rho$  is the density of the droplet, and  $g$  represents the acceleration of gravity.

The reaction force  $R_t$  supplied by the pillars can be given by:

$$R_t = (h_L + y_L) \times a^2 \times \frac{\pi R_1^2}{(a+b)^2} \times \rho g, \quad (9)$$

where  $(h_L + y_L)$  is the average height of the water column above the pillars,  $a^2$  represents the area of one pillar,  $R_1$  is

the radius of the three-phase contact line of the droplet on the macro structure, and  $\pi R_1^2 / (a+b)^2$  is the number of pillars in the droplet contact area.

The shape of the droplet on the pillar array consisted of a circular defect, expressed as  $x^2 + y^2 = S^2$ . At the center of the droplet (i.e. if  $x = 0, y = S$ ), as  $x$  increased, the value of  $y$  changed accordingly. The expression for  $y_L$  is given by:

$$y_L = \frac{\sum_{i=0}^n y_n}{n} = \frac{\sum_{i=0}^n \sqrt{R^2 - i^2(a+b)^2}}{n}. \quad (10)$$

Therefore,  $R_t$  can be written as:

$$R_t = \left( h + \frac{\sum_{i=0}^n \sqrt{R^2 - i^2(a+b)^2}}{n} \right) \times a^2 \times \frac{\pi R_1^2}{(a+b)^2} \times \rho g. \quad (11)$$

The surface tension caused by the droplet sagging between pillars  $F_1$  can be expressed by:

$$F_1 = \frac{\pi R_1^2}{(a+b)^2} \times 4a \times \sigma_{gl} \times \sin \varphi, \quad (12)$$

where  $\sigma_{gl}$  represents the gas–liquid surface tension coefficient, and  $\varphi$  represents the angle between the arctangent of the droplet in the macrostructure gap and the vertical direction (figure 3(h)).

The peripheral surface tension force  $F_p$  can be expressed by:

$$F_p = 2\pi R \cos \theta \times \sigma_{gl}. \quad (13)$$

## 2.2. Basic theories of special wetting behaviors

**2.2.1. Surface energy gradient.** A surface energy gradient signifies a varying change in surface energy on a material surface due to changes in position. Normally, the surface energy of a material will be uniformly distributed, implying that the surface energy can maintain the same value throughout the entire surface [16]. Nevertheless, by using appropriate treatment methods, an uneven surface energy distribution can be introduced on the material surface, leading to the formation of a surface energy gradient. A surface energy gradient can guide the spontaneous transport of droplets on the surface. During this process, the surface tension of the droplet is unbalanced on the contact lines on both sides of the solid surface due to the surface energy gradient, resulting in a driving force that causes the droplets to move in the direction of the smaller contact angle (figure 3(g)). The driving force  $F$  can be described by [109]:

$$F = \pi R_0 \gamma_{gl} (\cos \theta_B - \cos \theta_A), \quad (14)$$

where  $R_0$  is the radius of the droplet, and  $\theta_A$  and  $\theta_B$  denote the contact angles of the side with lower wettability and higher wettability of the droplet, respectively.

**2.2.2. Laplace pressure difference.** In addition to a surface energy gradient, a Laplace pressure difference serves as another driving force for droplet transport on a convex structure [109]. Laplace pressure difference consists of pressure difference between the surface and the interior of a droplet caused by curvature. During droplet formation, transport, and stability, the curvature of the droplet surface will have a direct effect on the Laplace pressure difference. As an example, for a water droplet on a convex surface with a cone structure (figure 3(h)), the Laplace pressure difference  $\Delta P$  can be expressed by:

$$\Delta P = - \int_{R_S}^{R_L} \frac{2\gamma}{(R + R_0)^2} \sin \alpha dz, \quad (15)$$

where  $R$  represents the local radius of the cone structure ( $R_S$  and  $R_L$  denote the local radii of the cone structure at two sides of the droplet),  $\alpha$  is the half apex angle of the cone structure, and  $dz$  is the minute incremental radius along the cone structure. According to equation (15),  $\Delta P > 0$  because  $R_S < R_L$ . In this case, the Laplace pressure difference generated by geometric heterogeneity will cause the droplet to move in the direction from the tip to the bottom of the cone structure.

Overall, special wettability observed in nature can be closely related to these basic theories. In past years, researchers have developed advanced wetting models based on the classic Wenzel and Cassie–Baxter models, and these breakthroughs have often been used to explain static wetting and dynamic wetting behaviors. However, the complexity and diversity of the material surface under actual conditions introduce certain challenges that can hinder the research process of existing wetting theories. Therefore, additional research on the wetting mechanisms, the exploration of new theoretical models, and the combination of advanced computer tools is needed for elucidating wetting phenomena in nature, as well as the rational design of surfaces with special wettability.

### 3. Representative structures in nature

To adapt to different complex environments, both animals and plants have evolved various structures, which have served as inspiration and strategies for researchers to design and fabricate MAAMs-SW, making them a prominent research topic in the field of surfaces and interfaces. In this section, we summarize the representative structures in nature, including macrostructures on the biological surfaces of rice leaves, *Salvinia* leaves, desert beetle elytra, cactus, pine needles, and *Araucaria* leaves, as well as micro/nanostructures on biological surfaces of springtail skin, spider silk, *Nepenthes alata*, butterfly wings, and shark skin (figure 4). Several biological surfaces with representative structures and special wettability are listed in table 1.

#### 3.1. Biological surfaces with macrostructures

**3.1.1. Rice leaves.** Isotropic superhydrophobicity is characterized by water droplets that can roll freely in all directions on a surface. However, rice leaves exhibit unique

anisotropic superhydrophobicity (figure 4(a)) [26]. Rice leaf surfaces contain three structures with different sizes, namely, sub-millimeter-scale groove arrays, microscale papillae, and nanostructures [76]. The spacing and height of the sub-millimeter-scale groove arrays reach 200  $\mu\text{m}$  and 45  $\mu\text{m}$ , respectively. Water droplets on rice leaf surfaces most easily roll along the direction parallel to the leaf edge. This is reflected in the sliding angle parallel to the direction of the leaf edge, with a value of  $3^\circ$ , while the sliding angle perpendicular to the direction of the leaf edge has a value of  $9^\circ$ . Therefore, rice leaves exhibit anisotropic superhydrophobicity. The main reason for this involves the macro-scale groove arrays, which provide different wetting energy barriers in directions parallel and perpendicular to the leaf edge.

**3.1.2. *Salvinia* leaves.** Although *Salvinia molesta* is a floating plant, its leaves remain dry when removed from water, primarily due to excellent superhydrophobicity (figure 4(b)) [67]. Scanning electron microscopy (SEM) observations have shown that the upper side of *S. molesta* leaves is densely covered with complex multicellular hairs, with sets of four hairs connected to form a macrostructure similar to an eggbeater, for a total height of approximately 2 mm. The surfaces of *S. molesta* leaves are covered with layers of waxy nanocrystalline structures, which also contribute to superhydrophobicity. However, the top of the eggbeater structure of *S. molesta* lacks waxy nanocrystalline structures, leading to hydrophilic patches that render the top of the eggbeater structure susceptible to water absorption. These hydrophilic patches on the eggbeater structure effectively fix the air–water interface, endowing the *S. molesta* surface with an excellent underwater air retention ability.

**3.1.3. Desert beetle elytra.** In the arid and hot climate of the Namib Desert, where rainfall is scarce, desert beetles have evolved the ability to collect water from fog, allowing them to survive in this harsh environment [68]. Figure 4(c) shows the dorsal view of an adult female desert beetle. At the macroscopic level, the beetle elytra are covered with numerous bumps, each with a diameter of  $\sim 500 \mu\text{m}$ , and the distance between adjacent bumps ranges from 0.5 mm to 1.5 mm. The top of each bump exhibits hydrophilic properties, while the sloped sides are covered with a layer of hydrophobic substances. Many flat hemispherical structures on the hydrophobic surface can be seen upon further magnification, with each hemisphere measuring 10  $\mu\text{m}$  in diameter. When the beetle is exposed to humid air, the hydrophilic tops of these bumps serve as sites for continuous fog condensation, facilitating the rapid growth of droplets. Once the water droplets reach  $\sim 5 \text{ mm}$  in size, they fall from the elytra. However, Park *et al* [90] proposed a different view, suggesting that even in the absence of local chemical patterns or micro/nanostructures, the surface structures were only convex millimeters in size, with specific geometric shapes that could promote condensation. Inspired by the bumps on desert beetle elytra, artificial structures with various applications have received widespread attention, including fog harvesting



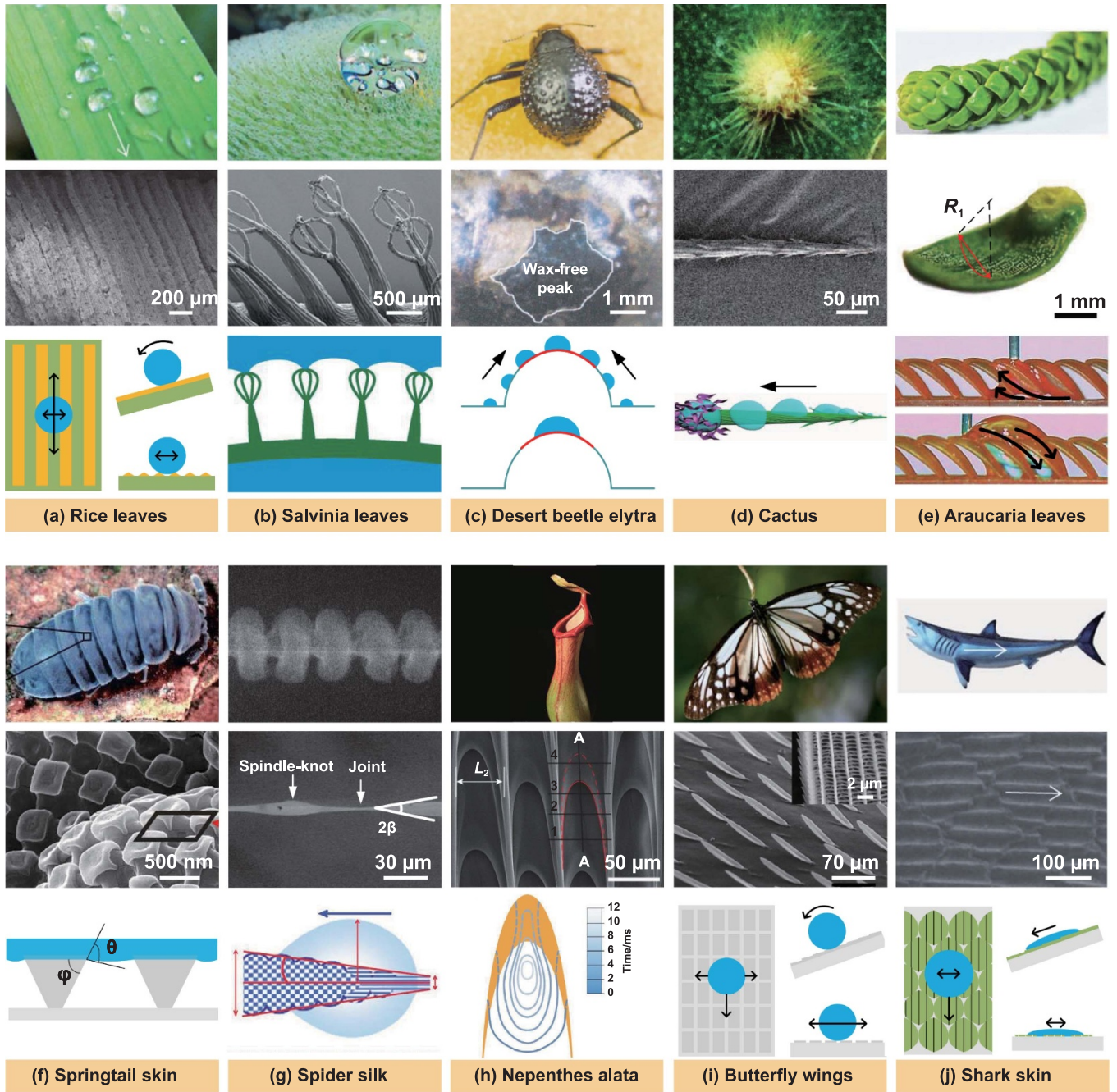


**Figure 4.** Overview of typical biological surfaces with special wettability. (a) Rice leaves. Top: Reproduced from [26] with permission from the Royal Society of Chemistry. Middle: [76] John Wiley & Sons. Copyright © 2011 WILEY-VCH Verlag GmbH & Co. KGaA, Weinheim. (b) Salvinia leaves: [67] John Wiley & Sons. Copyright © 2010 WILEY-VCH Verlag GmbH & Co. KGaA, Weinheim. (c) Desert beetle elytra: Reproduced from [68], with permission from Springer Nature. (d) Cactus: Reproduced from [69], with permission from Springer Nature. (e) Araucaria leaves: From [71]. Reprinted with permission from AAAS. (f) Springtail skin: Reproduced from [72]. CC BY 4.0. (g) Spider silk: Reproduced from [73], with permission from Springer Nature. (h) *Nepenthes alata*: Reproduced from [74], with permission from Springer Nature. (i) Butterfly wings: Reproduced from [75], with permission from Springer Nature. (j) Shark skin: Reproduced from [26] with permission from the Royal Society of Chemistry.

[63, 110–112], anti-icing [113, 114], and oil–water separation [115–117].

**3.1.4. Cactus.** Cacti, which thrive in desert conditions, display directional transport of liquid droplets and good water collection due to their unique surface structures [69, 118].

An illustration of the *Opuntia microdasys* stem is shown in figure 4(d), indicating the structural characteristics of the cactus [69]. The trichome features approximately 100 spines with lengths of 800–2500  $\mu\text{m}$  and diameters of 30–65  $\mu\text{m}$ . Each cactus spine consists of three parts: the oriented barbs at the tip, gradual gradient grooves in the middle, and belt-structured trichomes at the bottom. A study on the



**Table 1.** A selection of biological surfaces with representative structures and special wettability.

| Scale of structure   | Biological surfaces     | Structure characteristics   | Special wettability   | Additional functionalities                                     | References |
|----------------------|-------------------------|---|---|--|------------|
| Macrostructures      | Rice leaves             | Groove arrays (period: 200 $\mu\text{m}$ , height: 45 $\mu\text{m}$ )   | Superhydrophobicity, anisotropic wettability  | Drag reduction   | [26, 76]   |
|                      | <i>Salvinia</i> leaves  | Eggbeater structures (height: 2 mm)   | Superhydrophobicity, hydrophilicity   | Underwater air retention, drag reduction                       | [67]       |
|                      | Desert beetle elytra    | Bump structures (diameter: 500 $\mu\text{m}$ )  | Hydrophobic/hydrophilic patterns, or structure-induced condensation droplet aggregation | Water collection   | [68]       |
|                      | Cactus                  | Spine structures (length: 800–2500 $\mu\text{m}$ , diameter: 30–65 $\mu\text{m}$ )                                  | Structure- and surface-energy-induced self-driving of droplets                          | Directional transport, water collection                        | [69]       |
|                      | Pine needles            | Conical and inclined macro needle arrays with a height gradient and Janus structure                                 | Structure-induced self-driving of droplets  | Directional transport, water collection, heat transfer         | [70]       |
|                      | <i>Araucaria</i> leaves | Ratchet arrays (height: 2 mm, pitch: 3 mm, length: 2.6 mm)  | Structure-induced self-driving of liquid  | Directional liquid transport                                   | [71]       |
|                      | Fish scale              | Sector-like scale arrays (diameter: 4–5 mm)   | Superhydrophilicity, underwater superoleophobicity                                      | Drag reduction   | [25]       |
| Micro/nanostructures | Springtail skin         | Re-entrant structure arrays (diameter: 0.3–1 $\mu\text{m}$ )  | Superoleophobicity  | Oil repellency   | [72]       |
|                      | Spider silk             | Alternating spindle-knots and joints (period: $(89.3 \pm 13.5) \mu\text{m}$ )                                       | Structure- and surface-energy-induced self-driving of droplets                          | Directional transport, water collection, mechanical properties | [73]       |
|                      | <i>Nepenthes alata</i>  | Arch-shaped microcavities (average size: 50 $\mu\text{m}$ )   | Structure- and surface-energy-induced self-driving of droplets                          | Directional transport, water collection                        | [74]       |
|                      | Butterfly wings         | Scaly structures with directional arrangement (length: $(85 \pm 6) \mu\text{m}$ , width: $(14 \pm 1) \mu\text{m}$ ) | Superhydrophobicity, directional adhesion of droplets                                   | Structural color, antireflection, self-cleaning                | [21, 75]   |
|                      | Shark skin              | Riblets (period: 30–50 $\mu\text{m}$ )  | Superhydrophilicity, underwater oleophobicity   | Drag reduction, anti-biofouling                                | [26]       |

fog collection performance of this cactus revealed that, even if the tip was pointed vertically downward, water droplets would be directionally driven from the tip to the base of the spine, resulting from two forces generated by the Laplace pressure difference [119, 120] and surface energy gradient [121, 122] on the spine, driving the directional transport of water droplets. This multifunctional integrated water collection system embodied by the cactus has inspired the design and fabrication of artificial continuous water collectors for large-scale water collection.

**3.1.5. Pine needles.** Pine needles (*Sabina chinensis*) exhibit four types of asymmetry, which contribute to the directional transport of water droplets [70]. *S. chinensis* needles are conical and inclined, with a height gradient and Janus structure, and the two sides of the needle are flat and curved. The needles possess a height gradient of  $30^\circ$  and a tilt angle of  $50^\circ$ . By comparing and observing the coalescence events at the Janus and conical pillar tips, studies have shown that the droplets generated after coalescence will always flip on Janus pillars, regardless of the ratio of the droplet radius before coalescence.

Consequently, these droplets will congregate on the curved side of the pillar. This phenomenon, known as the Janus characteristic, serves as the main reason for the directional transport of water droplets, helping to overcome the natural tendency for smaller droplets to empty into larger droplets and leading to tip-induced flipping (TIF). The TIF effect offers substantial promise and important application value in microfluidic devices and water collection systems.

**3.1.6. Araucaria leaves.** Araucaria, a type of tree that thrives in warm and humid climates, is not resistant to drought and cold. Araucaria leaves are covered with 3D ratchets arranged periodically (figure 4(e)) [71], where the height  $h$  of each ratchet is  $\sim 2$  mm, with a pitch  $p$  of  $\sim 3$  mm, length  $l$  of  $\sim 2.6$  mm, and tilting angle  $\alpha$  of  $\sim 40^\circ$ . The ratchets have a transverse curvature of radius  $R_1$  and a longitudinal curvature of radius  $R_2$ . The leaves of Araucaria exhibit hydrophilicity, with water and ethanol contact angles of  $59^\circ$  and  $21^\circ$ , respectively. Ethanol will diffuse along the inclined direction of the ratchet, while water will propagate in the opposite direction. Researchers have observed that liquids with low surface energies exhibit bottom-to-top wicking at solid/liquid interfaces, while liquids with high surface energies exhibit top-to-bottom wicking. Directional liquid transport inspired by Araucaria leaves holds significant promise for various practical applications such as chemical reactions, water collection, and enhanced heat transfer.

### 3.2. Biological surfaces with micro/nanostructures

**3.2.1. Springtail skin.** Springtails generally inhabit humid environments that contain various harmful microorganisms and surface-active ingredients, resulting in liquid with low surface tension in these environments. Because springtails rely on their skin to breathe, it is imperative that they prevent their skin from becoming wetted by liquids. Investigations have revealed that springtails possess superhydrophobic and superoleophobic skin [72]. In aquatic or oily environments, the skin of springtails will form a stable air layer, promoting their ability to breathe. SEM images have unveiled that the skin of a springtail contains many re-entrant nanostructures (figure 4(f)). These nanostructures with re-entrant curvature are arranged in a rhombus pattern array, serving as the foundation of the springtail's superoleophobic skin [72, 123, 124]. Due to the negative curvature of the re-entrant profile, the advancing liquid phase must overcome the energy barrier. These findings have inspired novel strategies for the development of superoleophobic surfaces.

**3.2.2. Spider silk.** Spider silk has remarkable mechanical properties with broad application prospects in various fields, such as aviation, textiles, construction, and medicine [125–127]. The directional water collection mechanism of spider silk was revealed in 2010. Spider silk is composed of alternating spindle-knots and joints with a periodicity of  $(89.3 \pm 13.5)$   $\mu\text{m}$  [73]. The apex angle  $2\beta$  of the spindle-knots is  $\sim 19^\circ$ , and the diameters of the spindle-knots and joints are  $(21.0 \pm 2.7)$

and  $(5.9 \pm 1.2)$   $\mu\text{m}$ , respectively (figure 4(g)). Spider silk can capture fog, leading to the formation of tiny water droplets. With increasing volume, the water droplets move from the joints to the spindle-knots. During this process, tiny water droplets will be driven from the joints toward the spindle-knots by a surface energy gradient and Laplace pressure difference. Inspired by spider silk, directional droplet transport has found potential applications in the fields of water harvesting [128, 129] and oil–water separation [130, 131].

**3.2.3. *N. alata*.** *N. alata* can capture insects by using the microstructure and wettability of their peristome surface (figure 4(h)) [74]. The peristome of *N. alata* contains a two-level grooved structure. The size of the first-order microgroove is large, with a width  $L_1$  of  $(461.72 \pm 49.93)$   $\mu\text{m}$ . Each first-order microgroove contains approximately 10 s-order microgrooves. The size of the second-order microgroove is small, with a width  $L_2$  of  $(50.18 \pm 6.18)$   $\mu\text{m}$ . Numerous arch-shaped microcavities are regularly arranged in each two-layer microstructure, and water on the peristome surface can overcome its own gravitational force and be transported upward. During this process, the second-order microgrooves composed of arch-shaped microcavities can transport water, with the microcavity structure directionally strengthening the capillary rise in the transport direction while preventing backflow by pinning the liquid. Without a surface energy gradient, the liquid will exhibit high-speed one-way flow on the peristome surface. The bionic research of *N. alata* has shown broad application prospects in applications such as liquid/bubble transport [132–134], water harvesting [135, 136], medical devices [137, 138], and desalination [139].

**3.2.4. Butterfly wings.** Butterfly wings have the ability to remain clean and dry in heterogeneous environments. Goodwyn *et al* [75] studied the wettability and microstructure of *Parantica sita* wings (figure 4(i)) and found that the wing surface was superhydrophobic with self-cleaning properties. The white translucent regions of *P. sita* were highly ordered and organized in lines, forming periodic and parallel porous microstructures. The multiscale structure on the surface of a butterfly wing was found to be responsible for superhydrophobicity, as well as the colors of the wing. Prum *et al* [140] reported the colors and microstructures of 12 butterfly wings and observed that different structures on the wings produced different visible colors, such as blue, green, or purple. Superhydrophobicity with directional adhesion was observed on *Morpho aega* wings, which was caused by the direction-dependent arrangement of flexible nanotips on overlapped nanostripes and microscales [21]. In this arrangement, water droplets can easily roll off the wings along the outward direction of the body, as shown in the schematic diagram in figure 4(i), but will remain fixed when moving inwards [26, 141].

**3.2.5. Shark skin.** Unlike other large organisms in the ocean, sharks possess natural anti-fouling abilities, making it difficult for algae, barnacles, and other marine organisms to

adhere to their skin. Additionally, sharks exhibit a low drag coefficient, allowing them to move efficiently through water. Bixler and Bhushan [26] observed that the surface of shark skin was composed of non-packed tooth-like scales (dermal denticles) covered with micro riblets (period: 30–50  $\mu\text{m}$ ) (figure 4(j)). The study examined the wettability of shark skin with and without the natural mucous layer, and the results showed that shark skin with and without natural mucosa could absorb water droplets and exhibit superhydrophilicity. Due to the parallel arrangement of the riblets with water flow, the resistance of the sharks during movement decreased due to the reduction of vortex formation. Therefore, the presence of this unique structure could increase the speed of shark movement.

In summary, various unique structures and functions are found on biological surfaces with special wettability, endowing organisms with good environmental adaptability. Combining multiple disciplines may uncover more biological surfaces and functions, and by studying the relationships between structures and functions of these biological surfaces, researchers have illuminated some of the mechanisms underlying special wettability. Furthermore, the imitation of biological macro/micro/nanostructures has led to surfaces with special wettability, which can provide practical functions such as self-cleaning, drag reduction, and anti-icing abilities. These achievements may provide a direction for future research and serve as a good foundation for the application of bio-inspired MAAMs-SW in the aviation, navigation, energy, environment, and biomedical fields.

#### 4. Fabrication of bio-inspired MAAMs-SW

In the manufacturing industry, three fundamental techniques for producing parts have emerged, namely additive manufacturing, subtractive manufacturing, and formative manufacturing (figure 5) [142–144]. These three methods have been frequently used to fabricate bio-inspired special wetting MAAs. In the process of fabricating these materials, the commonly used additive manufacturing method is 3D printing; the commonly used subtractive manufacturing methods include laser etching, wire electrical discharge machining, micro-mechanical cutting, and electrochemical machining; and the commonly used formative manufacturing methods include the template method and imprinting method. This section summarizes recently developed strategies for the fabrication of bio-inspired MAAMs-SW.

##### 4.1. Additive manufacturing method

Additive manufacturing, also known as 3D printing, is a type of rapid prototyping technology that uses powder metal, plastic, or other adhesive materials to construct objects using layer-by-layer printing. 3D printing has shown to be an effective strategy for fabricating multiscale and multifunctional structures for wide applications in industry, academia, and daily use [145–148]. The common 3D printing technologies for fabricating MAAMs-SW include fused deposition molding, selective laser sintering/melting, direct ink writing,

stereolithography, and projection micro stereolithography [36, 38, 149–158]. Sun *et al* [159] fabricated an inverted trapezoidal structure using selective laser melting, and figures 6(a)–(c) shows the SEM and optical images of the fabricated inverted trapezoidal structure. After aging treatment, the contact angle of the water droplet on the inverted trapezoidal structure was  $156^\circ$ , and the inverted trapezoidal structure had excellent corrosion resistance and wear resistance. Using the direct ink writing method, Ling *et al* [160] prepared  $\text{Al}_2\text{O}_3$ -based hierarchically porous composite ceramics reinforced with SiC. The surfaces exhibited hierarchically porous structures with millimeter and micrometer-scale pores (figures 6(d)–(f)), and the wettability of aluminum on the surfaces of the composite ceramics was enhanced compared to pure alumina ceramics. Wang and Willenbacher [161] presented a high-resolution direct ink writing method based on a phase-change-induced strategy to fabricate soft silicon objects with good shape fidelity (figure 6(g)). This method could quickly control the rheological properties of viscoelastic ink and prevent deformation of the structure caused by gravity. Inspired by rice leaves, the researchers printed a soft silicone film with macro groove arrays (figures 6(h) and (i)). After depositing carbon nanotubes, the macro groove arrays with a dual-scale structure (figures 6(j) and (k)) exhibited good superhydrophobicity with a contact angle of  $(160.1^\circ \pm 2.3^\circ)$  (figures 6(l) and (m)).

In contrast to the above-mentioned 3D printing technologies, stereolithography and projection micro stereolithography have been achieved by transferring liquid polymer resin to solidified voxels. Li *et al* [162] used multiscale stereolithography to print bioinspired functional surfaces with MAAs. Printed shark skin with riblet arrays (figures 7(a) and (b)) exhibited an average fluid drag reduction of 10% in a pipe flow experiment. The printed lotus leaf-inspired surface with a pillar pitch of 300  $\mu\text{m}$  demonstrated good hydrophobic properties (figure 7(c)). Sun *et al* [163] developed dual-scale re-entrant ratchets utilizing projection micro stereolithography (figure 7(d)), composed of a macro inclined ratchet array with a re-entrant tip and micro groove array on the ratchet structure surface. Figure 7(e) shows the SEM image of the printed macro re-entrant ratchet array with top and bottom widths of 100  $\mu\text{m}$  and 400  $\mu\text{m}$ , a length of 600  $\mu\text{m}$ , and an inclined angle of  $45^\circ$ . Figures 7(f) and (g) shows SEM images of two different micro grooves arranged perpendicular and parallel to the inclined direction of the macro ratchet structure. The study demonstrated the spreading dynamics of water–ethanol mixtures on the ratchet arrays with perpendicular and parallel micro groove structures (figures 7(h) and (i)). The results revealed the water–ethanol mixture spread forward along the inclined direction of the macro ratchet structure on a ratchet array with perpendicular micro groove structures, but flowed backward on the ratchet array with parallel micro groove structures. Yang *et al* [77] fabricated a superhydrophobic eggbeater structure inspired by *S. molesta* leaves using another projection micro stereolithography based 3D printing approach—immersed surface accumulation 3D (ISA-3D) printing (figure 7(j)). To study the effects of the structure on wettability, eggbeater structures with different numbers

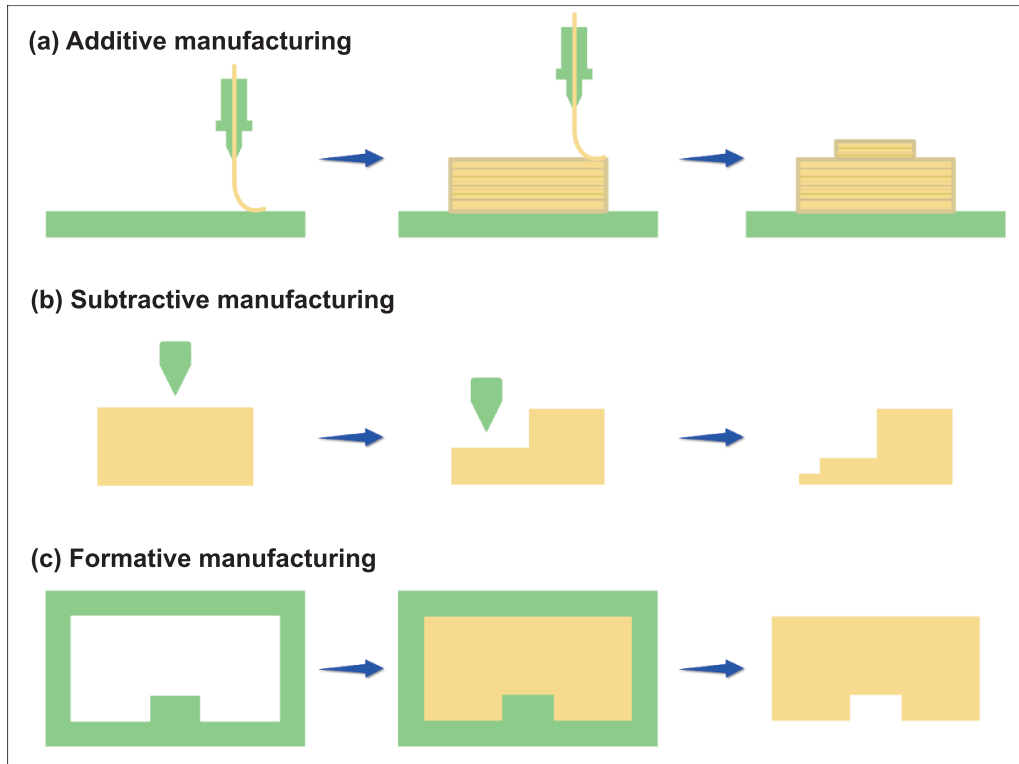


**Figure 5.** Schematic diagram of different processes. (a) Additive manufacturing. (b) Subtractive manufacturing. (c) Formative manufacturing.

of arms were fabricated (figure 7(k)). The study unveiled a correlation between superhydrophobicity, the number of eggbeater arms  $N$  and the gap distance  $d$  between the eggbeater structures. The fabricated surfaces were superhydrophobic with a contact angle of either  $170^\circ$  ( $N = 2$  and  $d = 0.5$  mm) or  $152^\circ$  ( $N = 4$  and  $d = 0.4$  mm). Due to high oil absorption, the superhydrophobic eggbeater structure could also be used to effectively separate oil from water.

In addition to printing two-dimensional (2D) MAAs on a flat surface, 3D printing technology can easily prepare 3D MAAMs-SW. Wang *et al* [164] developed initiator integrated 3D printing by adding a vinyl-terminated initiator to an ultraviolet (UV) curable resin, generating complex micro-lattices with a feature size of  $\sim 300$   $\mu\text{m}$  (figure 8(a)). Due to the enhanced roughness, the Lattices became superhydrophobic after poly(FOMA) modification and a perfectly spherical water droplet could form on the poly(FOMA) grafted Lattice (figure 8(b)). The printed mesh ball exhibited outstanding superhydrophobicity due to the rough micro riblet structures (figure 8(c)) and could be filled with water without any leakage (figure 8(d)). Dong *et al* [165] presented a new material concept for printing superhydrophobic objects based on a combination of digital light processing and polymerization-induced phase separation, and complex-shaped superhydrophobic structures (gyroid and spherical lattice) were printed to demonstrate the advantages of 3D printing (figures 8(e) and (f)). As shown in figure 8(g), the oil absorption performance of the printed hierarchically macro-nano porous

lattice was demonstrated based on superhydrophobicity and superoleophilicity.

These reports showed that the emergence of 3D printing technology has overcome certain challenges associated with the fabrication of complex structure arrays. Compared to traditional subtractive manufacturing methods, 3D printing technology offers significant advantages in prototyping and small-scale production. However, its disadvantages cannot be ignored, including the poor universality of the materials, low strengths of formed materials, and certain drawbacks in large-scale production. Despite these limitations, 3D printing technology will undeniably occupy an important position in the fabrication of MAAMs-SW due to its rapid development and unique processing.

#### 4.2. Subtractive manufacturing method

**4.2.1. Laser etching.** High-energy pulsed laser beams can be used to etch structures on materials with a width of 10–500  $\mu\text{m}$  and depth of 5–1000  $\mu\text{m}$ . Due to its precision and control, laser etching has emerged as a cutting-edge processing method for creating functional surfaces, offering versatility across various machinable materials and suitability for mass production [31, 32, 166]. Recently, femtosecond laser etching has been used to obtain macro-structures with special wettability [86, 167]. Figures 9(a) and (b) shows a femtosecond laser processing system and schematic diagram of interactions between the femtosecond



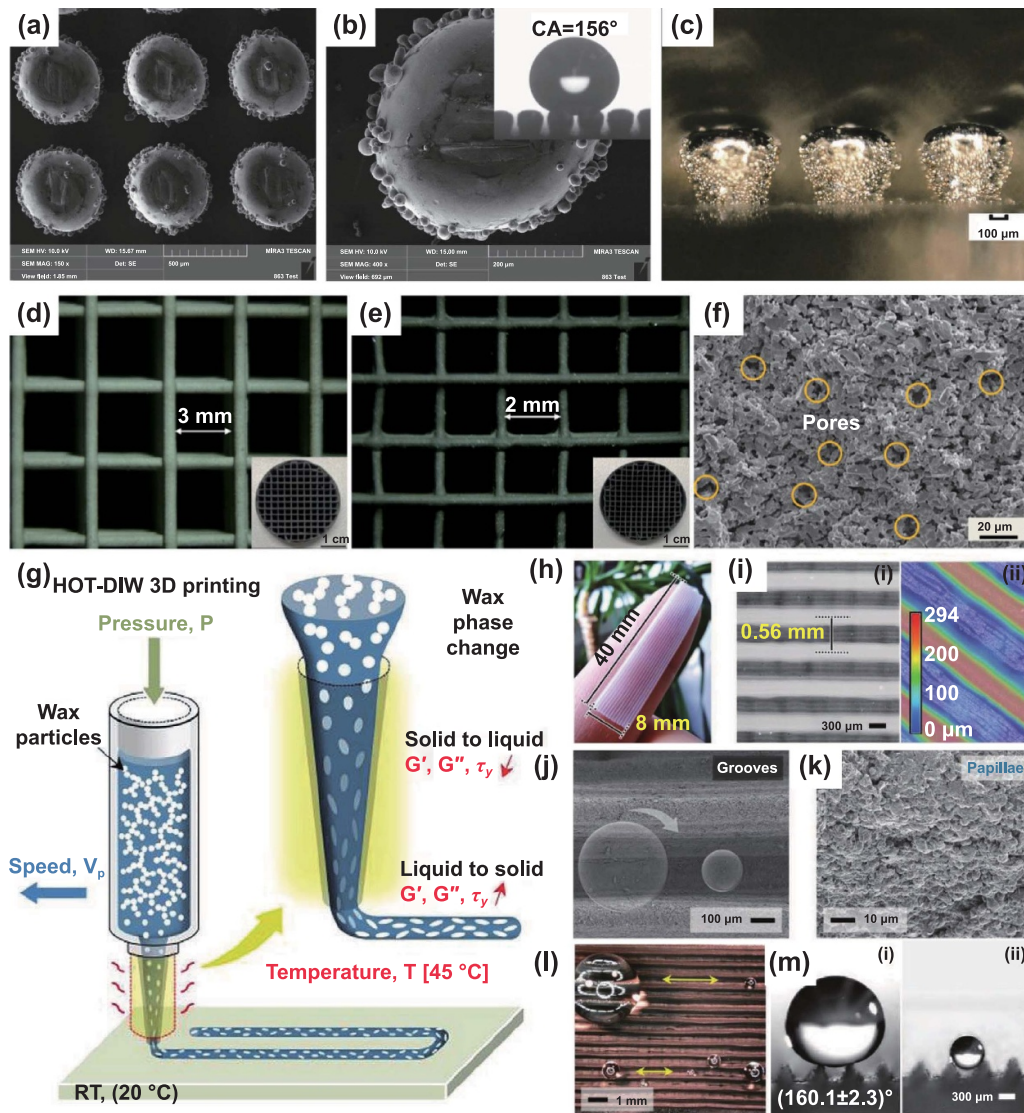


**Figure 6.** MAAMs-SW fabricated using selective laser melting and direct ink writing. (a) and (b) SEM images of the inverted trapezoidal structure. (c) Optical image of the side of the inverted trapezoidal structure. (a)–(c) Reprinted from [159], © 2020 Elsevier B.V. All rights reserved. (d)–(f) Optical images and SEM image of the hierarchically porous structure. Reprinted from [160], © 2022 The Society of Manufacturing Engineers. Published by Elsevier Ltd. All rights reserved. (g) Schematic illustration of the high-resolution direct ink writing process. (h) Groove structures inspired by rice leaves. (i) Microscopy images of the groove structures. (j) and (k) SEM images of the multiscale structures. (l) Optical image of water droplets on the groove structures. (m) Side view images of large and small water droplets on the groove structures. (g)–(m) [161] John Wiley & Sons. © 2022 The Authors. Advanced Materials published by Wiley-VCH GmbH.

laser pulse and the substrate [168]. Fang *et al* [169] employed femtosecond laser etching technology to fabricate a polydimethylsiloxane (PDMS) surface with MAAs. Inspired by rice leaves, a bidirectional anisotropic sliding surface was created with macro-groove arrays and coral-like microstructures (figures 9(c) and (d)). The sliding angle of the surface was  $(1.4^\circ \pm 0.1^\circ)$  in the parallel direction and  $(11.6^\circ \pm 0.3^\circ)$  in the vertical direction (figure 9(e)). Moreover, a ‘step’ structure was introduced into the macro-grooves. There were three rough steps in each macro-groove whose width  $L$  was  $300 \mu\text{m}$ , and the laser-induced steps possessed microscale and nanoscale structures (figures 9(f) and (g)). The step-like structures in the macro-groove arrays

also possessed tridirectionally anisotropic sliding superhydrophobicity (figure 9(h)). Bi/tridirectionally anisotropic sliding properties have enormous potential applications in smart microfluidic systems. Cai *et al* [86] reported a tridirectionally anisotropic slippery surface with step-like macro groove arrays, which were fabricated using two-round femtosecond laser ablation on a copper substrate. After chemical oxidation, the surface of the step-like macro groove array was uniformly covered with micro particles and nano needles (figure 9(i)), and with subsequent fluorination and injection with silicone oil, slippery surfaces with step-like macro groove arrays were obtained under different spinning speeds (figures 9(j)–(l)).

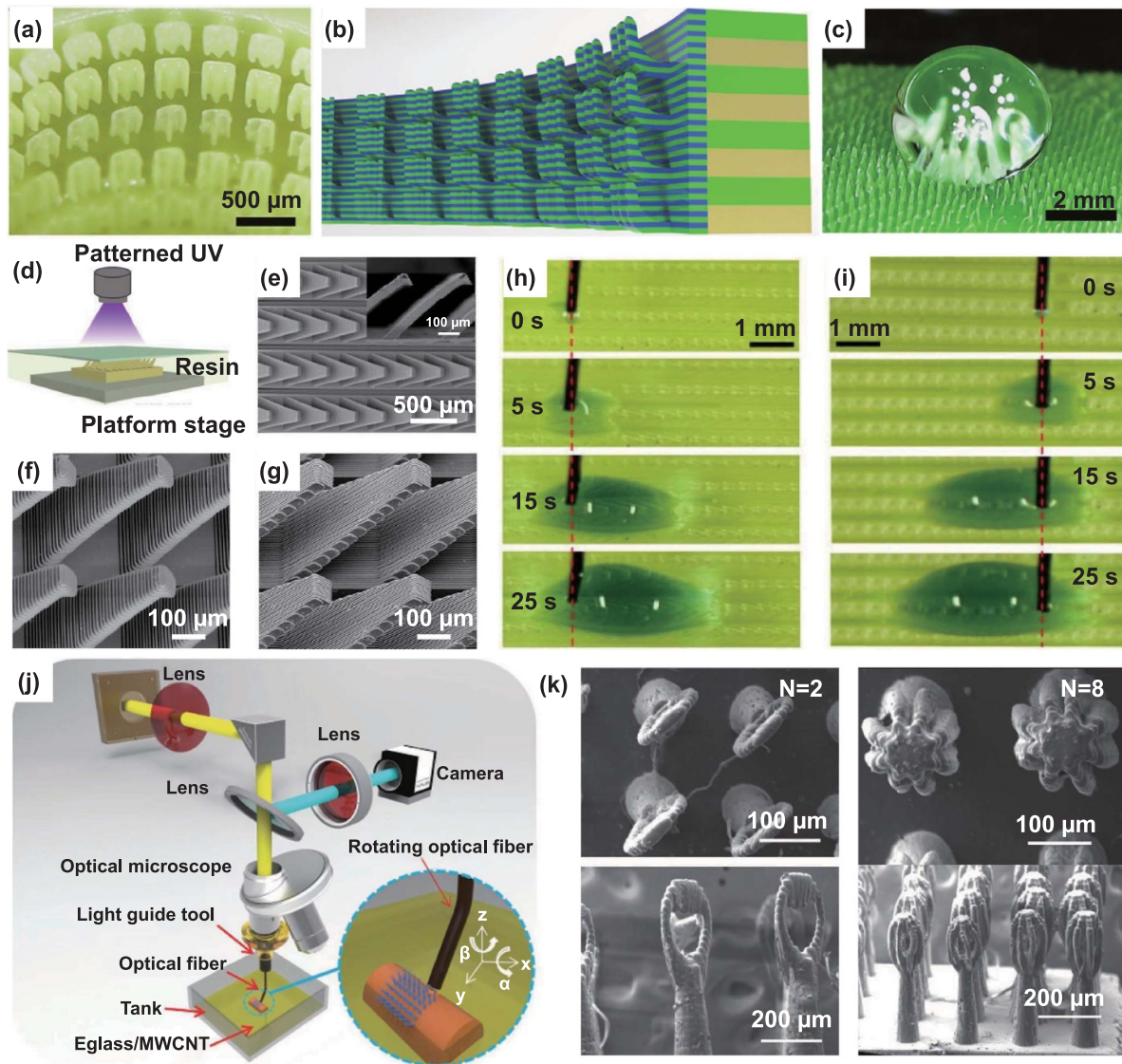


**Figure 7.** MAAMs-SW fabricated by stereolithography and projection micro stereolithography. (a) Shark skin printed by the multiscale stereolithography. (b) Schematic diagram of multiscale printing of shark skin. (c) Printed lotus leaf-inspired surface with good hydrophobic properties. (a)–(c) [162] John Wiley & Sons. © 2019 WILEY-VCH Verlag GmbH & Co. KGaA, Weinheim. (d) Schematic illustration of projection micro stereolithography. (e) SEM images of the printed macro re-entrant ratchet array. (f) and (g) SEM images of two different micro grooves arranged perpendicular and parallel to the inclined direction of the macro ratchet structure. (h) and (i) Spreading dynamics of water–ethanol mixtures on ratchet arrays with perpendicular and parallel micro groove structures. (d)–(i) Reproduced from [163]. The Author(s). [CC BY 4.0](#). (j) Schematic diagram of ISA-3D printing system. (k) SEM images of macro eggbeater arrays with different numbers of arms ( $N$ ) fabricated by the ISA-3D printing system. (j) and (k) [77] John Wiley & Sons. © 2018 WILEY-VCH Verlag GmbH & Co. KGaA, Weinheim.

Compared to ultrafast lasers, nanosecond lasers have lower costs, higher efficiencies, and reduced environmental condition requirements [170–174], making nanosecond laser etching technology suitable for the industrial production of bio-inspired materials with MAAs. Pan *et al* [88] used nanosecond laser etching technology to fabricate macro-conical pillar arrays (figure 10(a)), and figures 10(b) and (c) shows the SEM images of the fabricated macro-conical pillar arrays. After additional low-surface-energy modification, the macro-conical pillar arrays exhibited excellent water-repellent properties (figure 10(d)). Furthermore, macro-conical pillar arrays with different pillar tilt angles were constructed by changing

the tilt angles of the metallic substrates during the laser etching process. The results revealed that the superhydrophobic macro-conical pillar arrays demonstrated good durability, corrosion resistance, and anti-icing performance. Tran and Chun [175] fabricated grid structured arrays on pure aluminum surfaces using nanosecond laser etching technology, with the surface exhibiting excellent superhydrophobicity after boiling water treatment and silicone oil heat treatment. An extreme wettability surface with superhydrophilic and superhydrophobic patterns was obtained using a second nanosecond laser and boiling water treatment to the fabricated superhydrophobic surface. As shown in figure 10(e), the water droplets



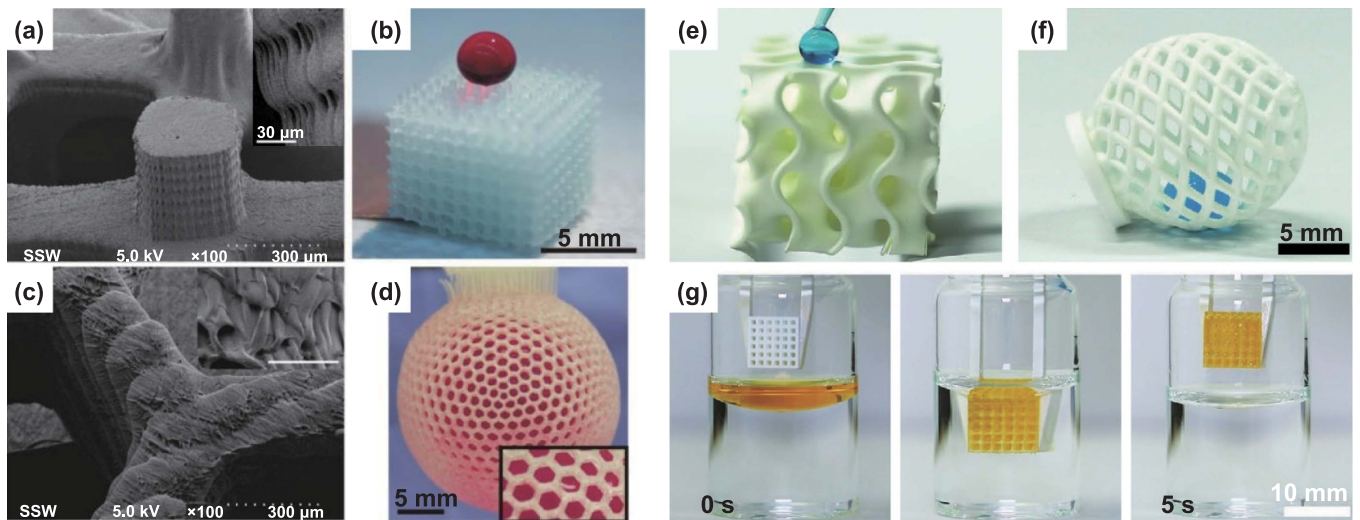


**Figure 8.** Three-dimensional MAAMs-SW fabricated using 3D printing technology. (a) SEM image of a Lattice. (b) Dyed water droplet on a poly(FOMA)-Lattice. (c) SEM image of a printed mesh ball. (d) Dyed water filled poly(FOMA)-mesh ball. (a)–(d) Reproduced from [164] with permission from the Royal Society of Chemistry. (e) and (f) Complex-shaped superhydrophobic structures. (g) Fast absorption process of soybean oil with a hierarchically macro-nano porous lattice. (e)–(g) [165] John Wiley & Sons. © 2021 The Authors. Advanced Materials published by Wiley-VCH GmbH.

formed a clear array on the superhydrophobic surface with a superhydrophilic triangular pattern. This proposed process could be used to fabricate complex superhydrophilic and superhydrophobic patterns without any additional mask or treatment (figure 10(f)).

Nevertheless, a significant challenge associated with nano-second laser etching is the large amount of heat generated, which can cause thermal damage to the material [176, 177]. This limitation has implications for the practical application of bio-inspired MAAMs-SW. Water jet-guided laser micromachining is an advanced processing technology that can not only improve the processing accuracy and efficiency of the nano-second laser, but also reduce thermal damage [178, 179]. Shi *et al* [180] used a water jet-guided laser to fabricate macro/micro textured surfaces with different grid spacings, from 25 to 225 μm. Figure 11(a) shows the water jet-guided laser processing system. This approach significantly reduced the heat-affected zone that formed on the material surface by the water jet-guided laser, compared to conventional laser processing, and the water jet-guided laser had a better processing quality and a greater material removal rate (figure 11(b)). Figure 11(c) presents the 2D and 3D morphologies of a macro grid structure array fabricated by the water jet-guided laser with a spacing of 125 μm. The wettability test results showed that the fabricated metallic surfaces were initially hydrophilic, but after 20 d of air exposure, the contact angles on the textured stainless steel, titanium, and aluminum surfaces changed, yielding hydrophobicity/superhydrophobicity.

**4.2.2. Wire electrical discharge machining.** Wire electrical discharge machining is a process that harnesses electrical and thermal energy to remove metal materials. Unlike traditional machining methods, the tool and workpiece do not physically touch during the electrical discharge machining

process. Instead, metal removal is achieved through localized and instantaneous high temperatures generated by spark discharge between the tool and workpiece [181]. This technique has been increasingly used in recent years to fabricate MAAs [182–186]. Bae *et al* [182] fabricated a superhydrophobic aluminum alloy surface with a dual-scale structure using low-speed wire electrical discharge machining (figure 12(a)). The primary macroroughness, which formed a sinusoidal profile shape with a wavelength range of 200–500 μm, was achieved by programming the wire electrical discharge machining process. The secondary microroughness in the form of crater-like structures with sizes of several micrometers was naturally generated (figure 12(b)). The fabricated surface with a wavelength of 500 μm showed superhydrophobicity with a contact angle of 156°, without additional chemical treatment (figure 12(c)). Lian *et al* [186] fabricated submillimeter-scale asymmetric bump arrays on an aluminum alloy substrate using wire electrical discharge machining. Figures 12(d)–(f) shows the SEM images and optical image of the fabricated submillimeter-scale asymmetric bump arrays. After additional low-surface-energy modification and the infusion of silicone oil, the asymmetric bump arrays exhibited good slippery characteristics. Furthermore, the slippery macro asymmetric bump arrays showed great application potential for water collection at low temperatures.

**4.2.3. Micro-mechanical cutting machining.** Micro-mechanical cutting, which uses micro-cutting tools to remove excess material from a workpiece, serves as a fundamental principle in mold manufacturing and the processing of various metal parts. Micro-mechanical cutting has also been used to process micro- or macro-structures [187, 188]. Many types of micro-mechanical cutting methods exist, such as micro-turning, micro-drilling, and micro-milling [189]. Yu *et al*

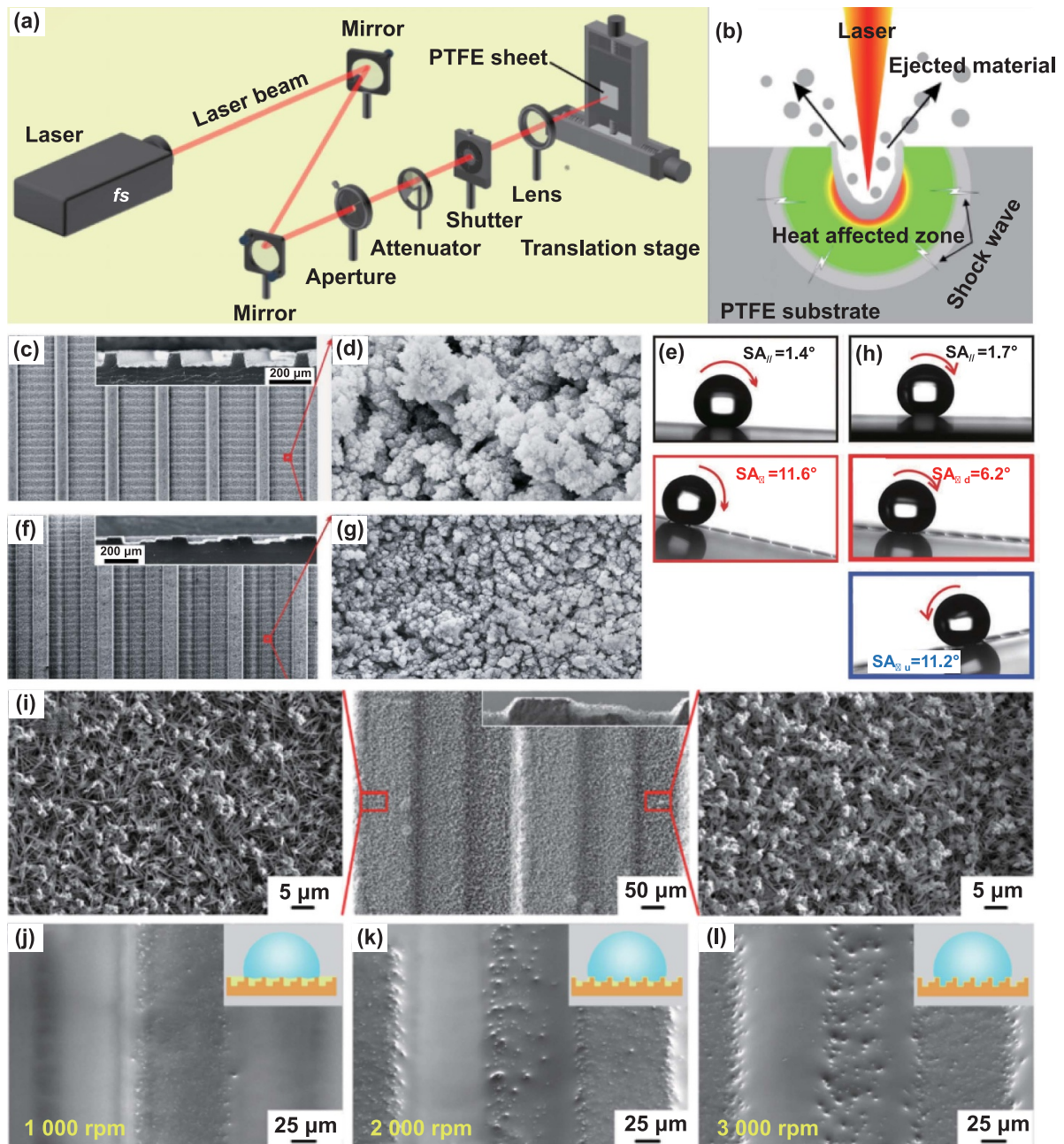


**Figure 9.** Superhydrophobic and slippery MAAs fabricated using femtosecond laser etching technology. (a) Schematic diagram of femtosecond laser processing device. (b) Schematic diagram of the interaction between the femtosecond laser pulse and the substrate. (a) and (b) Reproduced from [168]. The Author(s). CC BY 4.0. (c) SEM image and cross-sectional image of the macro-groove arrays (width  $L = 200 \mu\text{m}$ ). (d) Magnified SEM image of a macro groove. (e) Sliding behavior of water droplets on macro-groove arrays in parallel and perpendicular directions. (f) SEM image and its cross-section image of the surface with step-like structures in macro-groove arrays. (g) Magnified SEM image of the surface. (h) Sliding behaviors of water droplets in different directions. (c)–(h) [169] John Wiley & Sons. © 2018 WILEY-VCH Verlag GmbH & Co. KGaA, Weinheim. (i) SEM images of the step-like macro groove arrays with micro particles and nano needles. (j)–(l) SEM images of the lubricant oil state on the slippery surface obtained at spinning speeds of 1000, 2000, and 3000 rpm. (i)–(l) Reprinted from [86], © 2022 Elsevier B.V. All rights reserved.

[190] developed a miniature high-speed precision micro-milling machine (figure 13(a)) and fabricated submillimeter-scale groove arrays using a self-developed micro-milling machine on an aluminum alloy substrate (figures 13(b) and (c)). After abrasive belt grinding treatment, the groove arrays exhibited superhydrophobicity with a contact angle of  $(160^\circ \pm 0.7^\circ)$ . Using micro-mechanical processing, Song

*et al* [191] constructed hydrophobic macro groove and square column arrays on a polymethyl methacrylate substrate. Figures 13(d) and (e) presents the optical images of the macro groove and square column arrays. The study assessed the influence of the structural parameters of groove and square column arrays on the contact angle of water droplets using a combination of theoretical analysis and experimental methods. The



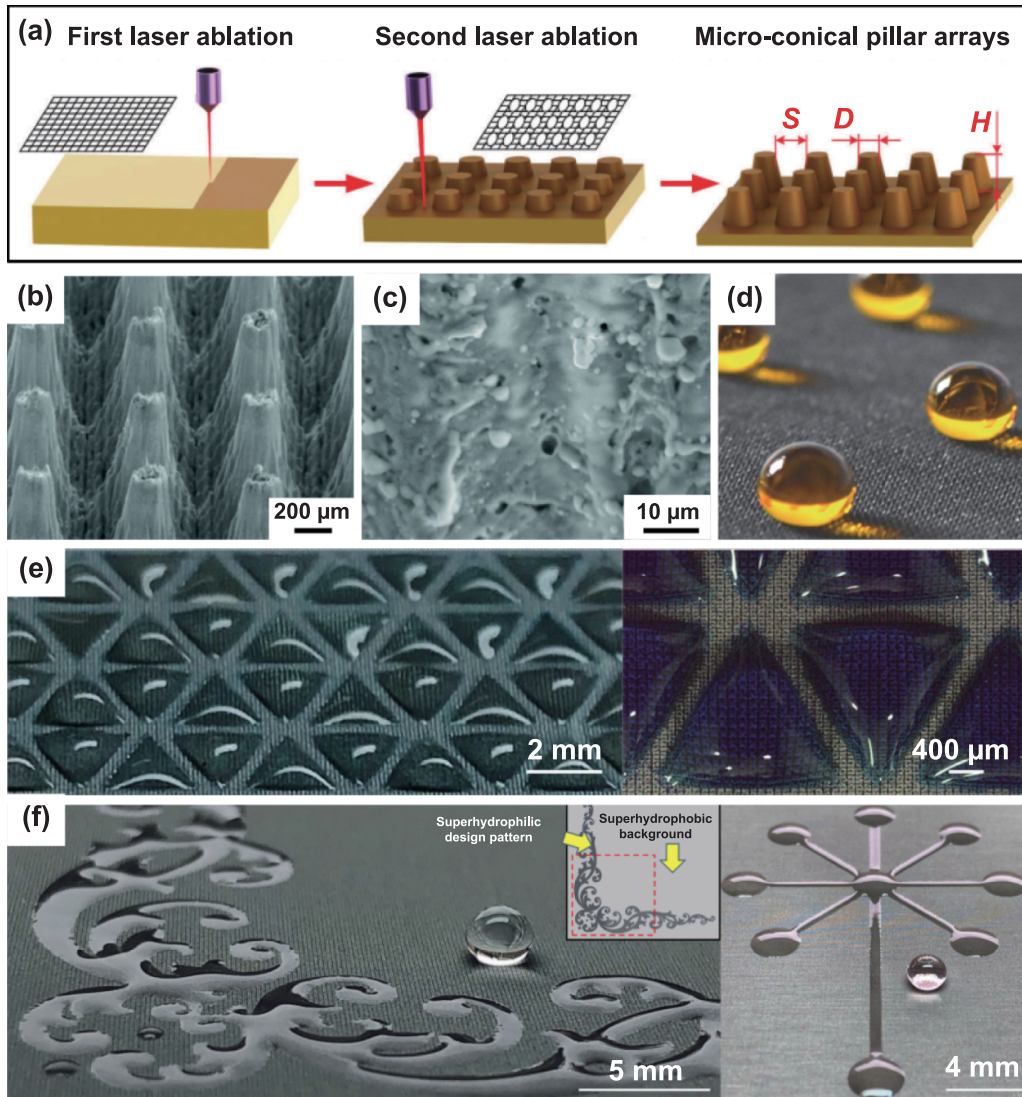


**Figure 10.** MAAMs-SW fabricated using nanosecond laser etching technology. (a) Diagram of the fabrication of macro-conical pillar arrays. (b) and (c) SEM images of the fabricated macro-conical pillar arrays. (d) Water droplets on superhydrophobic macro-conical pillar arrays. (a)–(d) Reproduced from [88] with permission from the Royal Society of Chemistry. (e) Water droplet array on the superhydrophobic surface with a superhydrophilic triangular pattern. (f) Images of complex superhydrophilic and superhydrophobic patterns. (e) and (f) Reprinted from [175], © 2021 Elsevier B.V. All rights reserved.

results showed that the contact angle increased with increasing spacing of the macrostructures and decreased with increasing width of the square column arrays. The contact angle on the macro groove array was anisotropic (perpendicular to and parallel to the groove direction), and the contact angles in these two directions affected each other. Although the water droplets had a larger contact angle on the surface with the square column array, the stability of the contact angle was not as robust as the groove array. In addition to micro milling technology, Musavi *et al* [192] developed a grinding process for fabricating hydrophobic surfaces with groove arrays. Figures 13(f)–(h) presents the top- and side-view SEM images of the groove arrays, indicating that the contact angle of the fabricated surface was  $140^\circ$ , which was 380% higher than the corresponding smooth surface ( $37^\circ$ ). The main advantages of

this technique were its lower cost and faster production rate compared to the micro-milling method.

Fly cutting and single-point diamond turning, as an ultra-precision machining technique, has been widely used for fabricating micro structure arrays [187, 193, 194]. For MAAs, Zhang *et al* [195] fabricated a macro lens array using an offset-tool-servo diamond end fly cutting process (figure 14(a)). Figure 14(b) shows the simulated and machined morphologies of the macro lens array, and the results indicated that the macro lens units were uniformly aligned into a lens array. Based on this method, a hierarchical structure with a macro lens structure and secondary pyramid microstructure was successfully fabricated, as shown in figure 14(c). Although this report did not characterize wettability, it was believed that MAAMs-SW could be obtained using ultra-precision fly cutting technology.

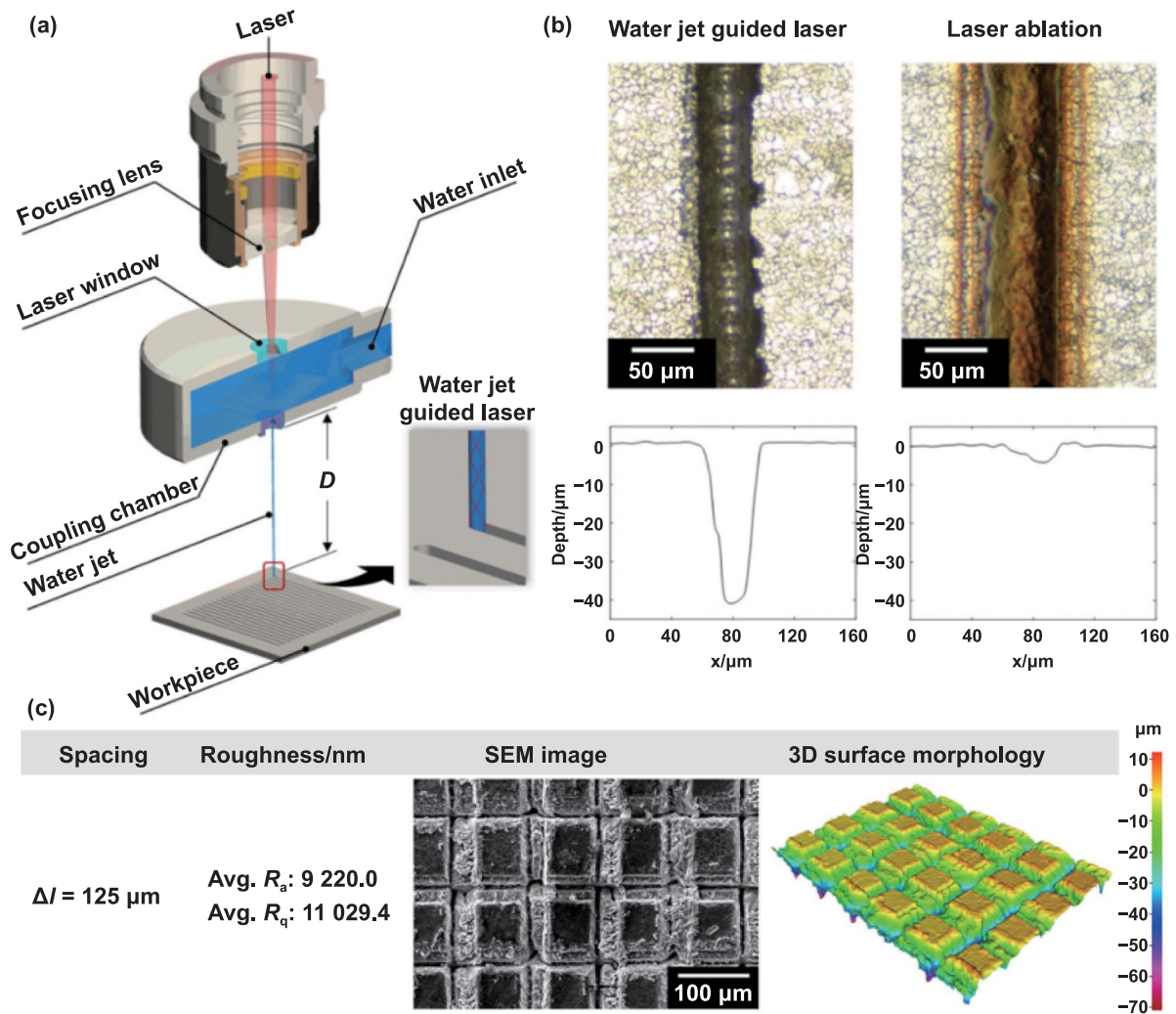


**Figure 11.** Superhydrophobic MAAs fabricated by water jet-guided laser technology. (a) Schematic diagram of the water jet-guided laser processing system. (b) Comparison of the optical image and profile between water jet-guided laser machining and conventional laser ablation. (c) 2D and 3D morphologies of the macro grid structure array with a spacing of 125  $\mu\text{m}$ . Reprinted from [180], © 2019 Elsevier B.V. All rights reserved.

Kurniawan *et al* [196] employed the 3D ultrasonic elliptical vibration texturing method to fabricate a rhombohedral pattern with pitches of 150–300  $\mu\text{m}$ . Compared to patterns formed by conventional cutting (single-crystal diamond tool), the rhombohedral patterns obtained using 3D ultrasonic elliptical vibration texturing method demonstrated a good surface finish with fewer micro defects (figures 14(d)–(g)). The anisotropic wettability of the fabricated rhombohedral patterns with different pitches was characterized, as shown in figure 14(h), indicating that the rhombohedral patterns slightly improved the wettability performance compared with the corresponding smooth surface.

**4.2.4. Electrochemical machining.** Electrochemical machining is a technique that involves machining metal materials through electrochemical reactions. Unlike mechanical machining, electrochemical machining is not limited by material hardness and toughness [197]. This relatively

mature special processing technique has been widely used in industrial fields [198, 199], and in recent years, mask electrochemical machining technology has been used to fabricate MAAs with superhydrophobicity [200]. However, in the mask electrochemical machining process, each sample requires mask production processes such as film mounting, exposure, and development, and the mask cannot be reused. Additionally, the sample can only be processed using processes such as diffusion and natural convection, due to the non-flowing nature of the electrolyte, leading to low processing efficiency and easy detachment of the mask layer. Lian *et al* [201] used maskless electrochemical machining technology to fabricate superhydrophobic square macro pit arrays on a stainless-steel substrate (figure 15(a)). First, a pyramid array was fabricated using wire electrical discharge machining, and the surface morphology is shown in figure 15(b). The obtained pyramid array as the cathode was then used to fabricate square macro pit arrays via the maskless electrochemical machining process. Figure 15(c) shows



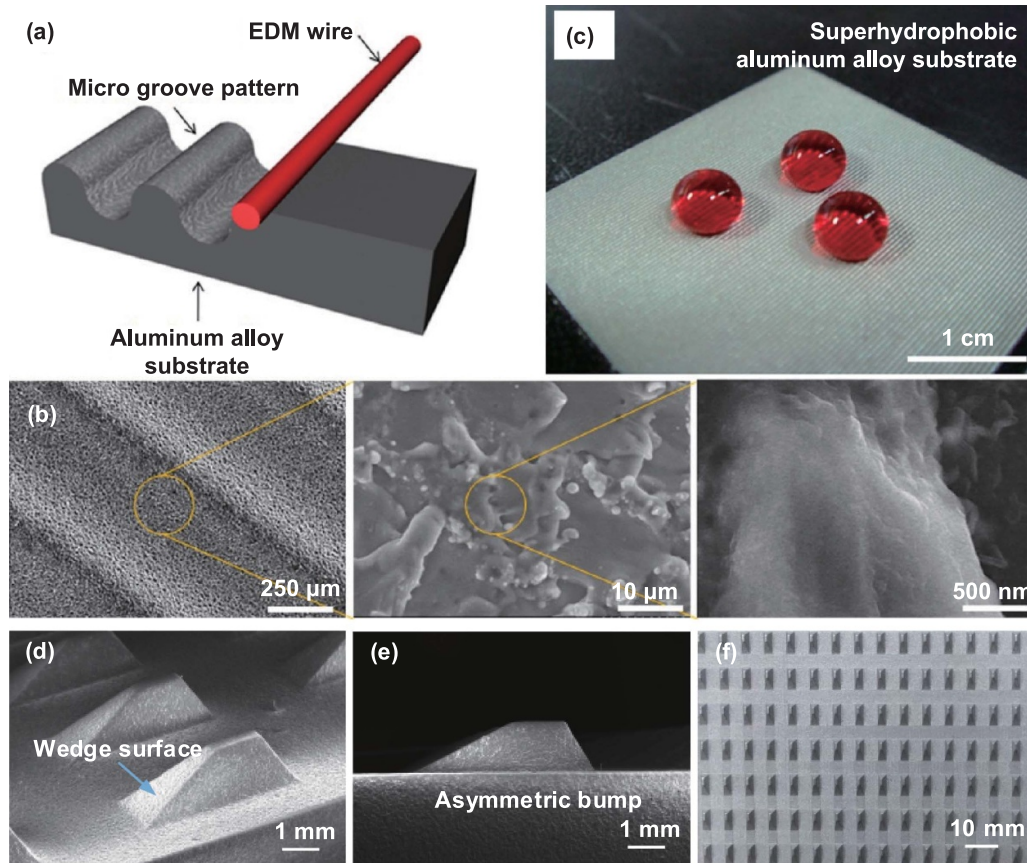


**Figure 12.** MAAMs-SW fabricated using wire electrical discharge machining. (a) Schematic diagram showing the fabrication of dual-scale structures. (b) SEM images of dual-scale structures. (c) Dyed water droplets on the fabricated surface. Reprinted with permission from [182]. Copyright (2012) American Chemical Society. (d)–(f) SEM and optical images of sub-millimeter-scale asymmetric bump arrays. Reproduced from [186], with permission from Springer Nature.

the SEM image of the square macro pit arrays on the anode surface. After storage in ambient air, the square macro pit arrays exhibited excellent superhydrophobicity (figure 15(d)). Wire-electrochemical machining technology has also been used to fabricate MAAMs-SW. Sharma and Chandraprakash [202] fabricated macro square pillar arrays on 304 stainless steel substrates using a wire-electrochemical micromachining process, and the macro square pillar arrays exhibited quasi-superhydrophobic properties with a contact angle of  $145^\circ$ .

According to the above summary, each subtractive manufacturing method possesses unique processing characteristics. For example, laser etching technology has shown to be advantageous in fabricating MAAs with superhydrophilic and superhydrophobic patterns, while femtosecond lasers are suitable for the fabrication of MAAs with high accuracy and low material damage, and nanosecond lasers are more useful for the fabrication of MAAs with low performance requirements due to their low cost and high efficiency. With a large aspect ratio, macro re-entrant arrays, and overhang arrays, wire electrical discharge machining technology has shown promise in fabricating MAAs. Due to a high degree of automation, micro-mechanical cutting machining technology has shown promise in the fabrication of highly precise

3D MAAs. Electrochemical machining technology may be suitable for the large-scale fabrication of MAAs with low material damage. Compared to emerging additive manufacturing methods, traditional subtractive manufacturing methods are more developed, with noticeable advantages in terms of process precision, automation, and efficiency. The cost can also be effectively controlled, especially in mass production, and subtractive manufacturing methods may be cheaper than additive manufacturing methods due to material costs. As a result, additive manufacturing methods cannot yet replace subtractive manufacturing methods in most fields. Moreover, the subtractive manufacturing process can accommodate a wider range of compatible materials, allowing MAAs to be fabricated on different materials, such as metals or polymers, using the same processing system.

### 4.3. Formative manufacturing method

**4.3.1. Template method.** The template method involves using a structural biological or structural artificial surface as a mold, onto which casting, pouring, or coating is performed to create microstructures on a polymer surface. After removing the material or mold, the surface of the material takes on the structure opposite of the mold. This template

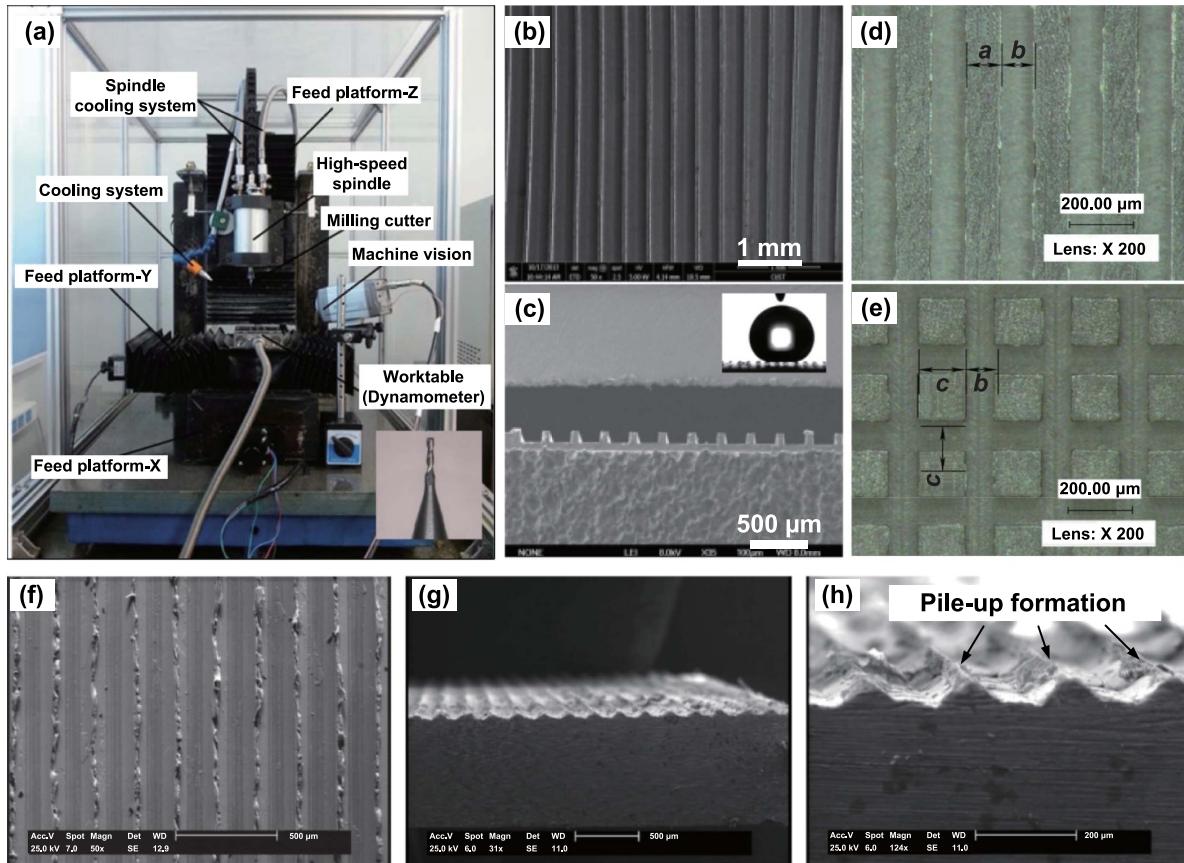


**Figure 13.** MAAMs-SW fabricated by micro-milling and grinding. (a) High-speed precision micro-milling machine. (b) SEM image of macro-groove arrays. (c) Cross-sectional image of macro-groove arrays, with the inset showing the optical image of a water droplet on microgrooves treated with abrasive belt grinding. (a)–(c) [190] [12 February 2016], reprinted by permission of the publisher (Taylor & Francis Ltd, [www.tandfonline.com](http://www.tandfonline.com).) (d) and (e) Optical images of macro groove and square column arrays. (d) and (e) Reproduced with permission from [191]. Copyright (2016) CMES. (f)–(h) Top-view and side-view SEM images of the groove arrays fabricated by grinding. (f)–(h) Reprinted from [192], © 2022 Elsevier Ltd. All rights reserved.

method is highly effective in forming macro/micro/nanostructures on a solid surface [203–208]. Kang *et al* [209] fabricated superhydrophobic polymer surfaces using the template method with a 3D-printed mold (figure 16(a)). First, a mold with supporting parts was printed using different printing angles ( $0^{\circ}$ – $90^{\circ}$ ), and then a PDMS mixture was poured onto the mold and degassed at room temperature to remove bubbles generated during the pouring process. The PDMS mixture then underwent polymerization through baking, and finally, the cured PDMS was separated from the mold. As shown in figures 16(b)–(d), the polymer surface exhibited waveform macrostructures. The influence of the printing angle on the surface wettability was experimentally studied, and the results showed that when the printing angle was greater than  $40^{\circ}$ , the contact angle of the fabricated polymer surface was greater than  $150^{\circ}$ . Song *et al* [210] obtained millimeter-scale pillar arrays using the template method (figure 16(e)). In this process, micro drilling was used to fabricate the required mold with blind hole arrays (figures 16(f) and (g)). After spraying water-repellent nanomaterials, superhydrophobic macro-pillar arrays with a diameter of 1.05 mm, height of 0.8 mm, and spacing of 0.25 mm were obtained (figures 16(h) and (i)).

**4.3.2. Imprinting method.** Imprinting technology has drawn the attention of researchers and engineers due to its low cost, high efficiency and resolution, and has been widely used in the fields of biomedical device fabrication and semiconductor processing [211, 212]. Imprinting technology can be divided into hot imprinting [213, 214], UV imprinting [215], and soft imprinting [216, 217], according to the different forming principles. Hot imprinting is currently the main method for preparing MAAs. Moon *et al* [218] used a hot imprinting process to fabricate superhydrophobic polytetrafluoroethylene (PTFE) polymer surfaces with MAAs (figures 17(a) and (b)). In this process, die surfaces with sinusoidal 2D/3D patterns, pitches of  $640 \mu\text{m}$ , and amplitudes of  $240 \mu\text{m}$ , were fabricated by a wire electrical discharge machining (figures 17(c) and (d)). Figures 17(e) and (f) shows the fabricated PTFE polymer surfaces with the 2D/3D pattern shapes, where the contact angles on the 2D patterned surface were  $158.5^{\circ}$  and  $152.0^{\circ}$  in the perpendicular and parallel directions, respectively, and the 3D patterned surface exhibited a contact angle of  $156.7^{\circ}$  (figures 17(g) and (h)). Other than using hot imprinting to fabricate MAAs, transferring the macrostructure from the mold surface directly to the substrate can be achieved by



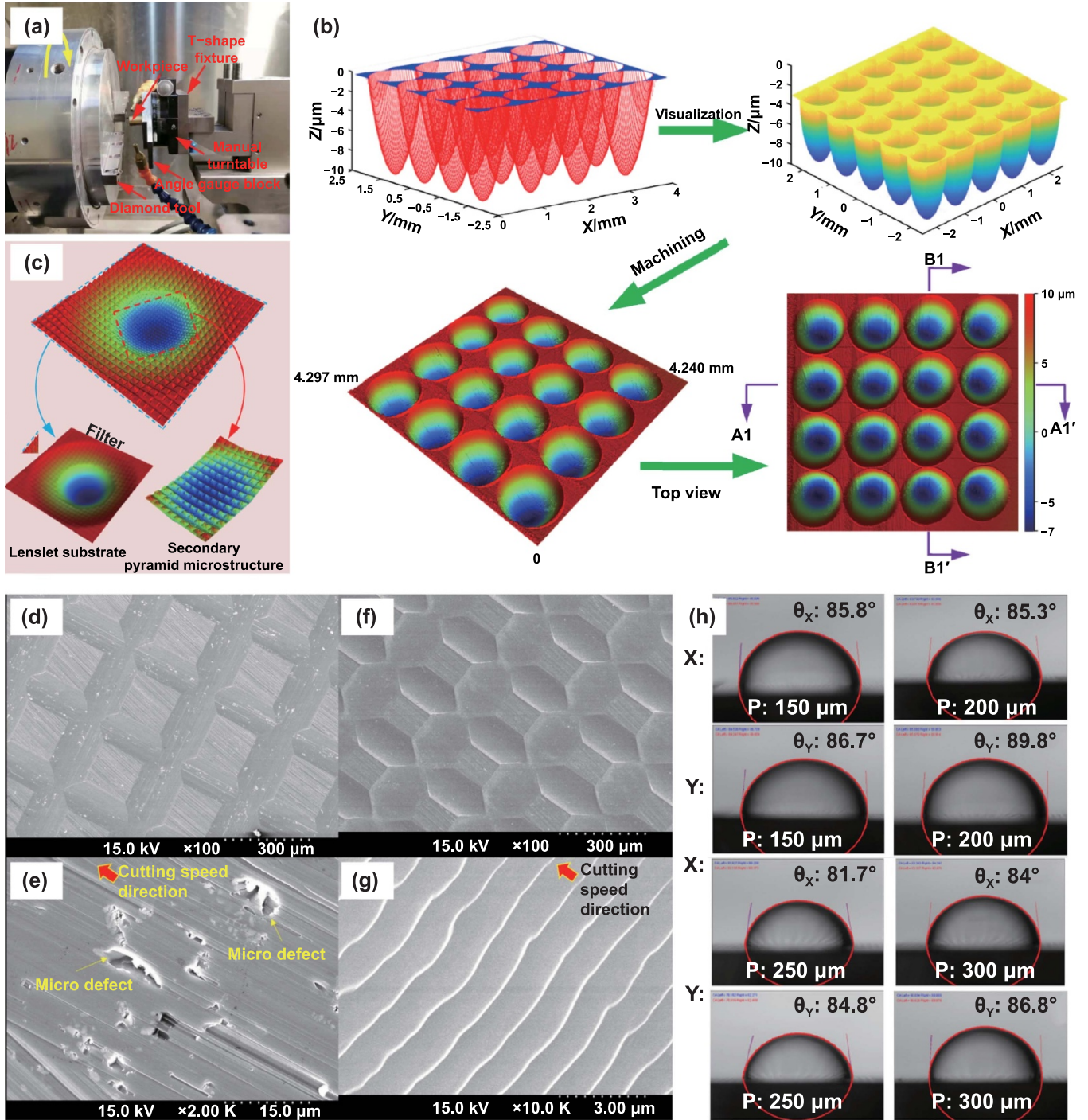


**Figure 14.** MAAMs-SW fabricated using fly cutting and single-point diamond turning. (a) Experimental setup of fly cutting. (b) Simulation and machining of a macro lens array. (c) Decomposition of hierarchical structures. (a)–(c) Reprinted from [195], © 2022 Elsevier Ltd. All rights reserved. (d) and (e) SEM images of the rhombohedral pattern with a pitch of  $300\ \mu\text{m}$  obtained by conventional cutting. (f) and (g) SEM images of the rhombohedral pattern obtained using the 3D ultrasonic elliptical vibration texturing method. (h) Anisotropic wettability of the fabricated rhombohedral patterns with different pitches. (d)–(h) Reprinted from [196], © 2020 Elsevier Ltd. All rights reserved.

cold imprinting. Wang *et al* [98] used the surface of a silicon-based regular pyramid array as the mold, and then pressed the metal base and the mold together with a 50 ton hydraulic press (figure 17(i)). After separation, an iron surface with an inverted pyramid array was obtained, as shown in figure 17(j), and using this method, the inverted pyramid arrays could be

copied onto various metals, such as nickel, copper, zinc, and aluminum alloys.

Formative manufacturing method, mainly involving template and imprinting methods, has become an efficient and high-precision fabrication strategy for MAAs. These approaches are well suited for the large-scale production

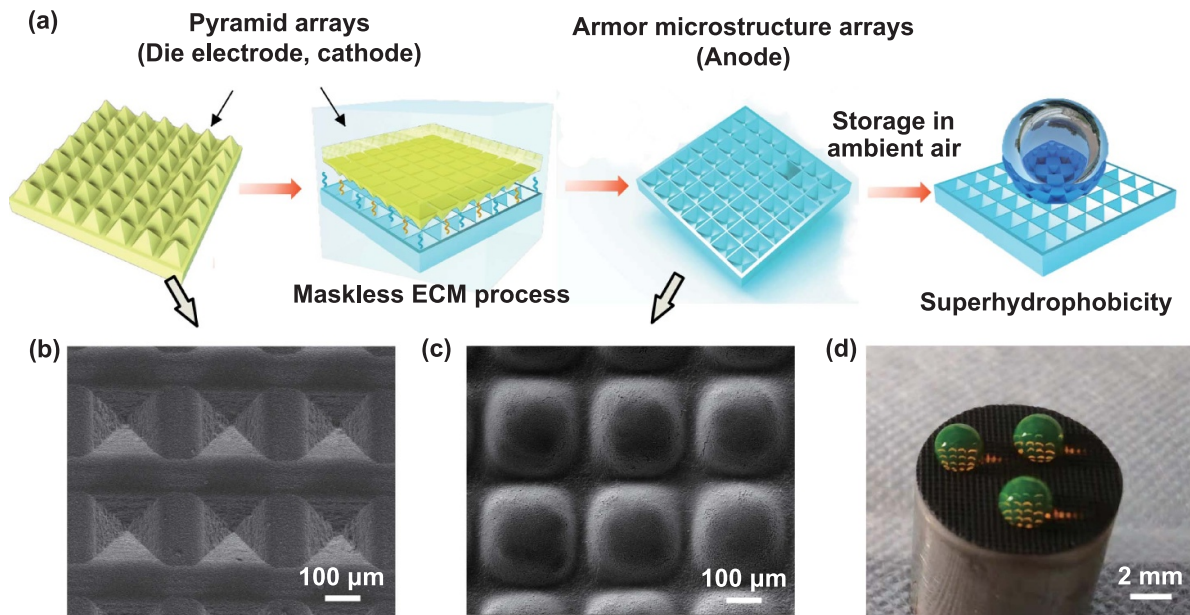


**Figure 15.** Superhydrophobic MAAs fabricated using electrochemical machining. (a) Fabrication process of the superhydrophobic square macro pit arrays. (b) SEM image of pyramid structure arrays on the cathode surface. (c) SEM image of square macro pit arrays on the anode surface. (d) Optical image of water droplets on the superhydrophobic square macro pit arrays. Reprinted from [201], © 2023 Published by Elsevier B.V.

of MAAs. However, formative manufacturing method requires additional mold processing steps, and fabricating MAAs with different morphologies requires different molds, placing higher requirements on mold design and manufacturing. In recent years, 3D printing technology has been gradually applied to mold manufacturing. This technology has significantly addressed the shortcomings of traditional mold manufacturing, such as complex process, high cost, and low efficiency, creating opportunities for the mold manufacturing industry.

In this section, we consolidated a few commonly used methods for the fabrication of bio-inspired MAAMs-SW into three categories: additive manufacturing, subtractive manufacturing, and formative manufacturing. These methods offer unique advantages but still have certain limitations (table 2). A single processing strategy can typically meet the fabrication requirements of common MAAs (groove arrays, column arrays, and hole arrays). However, some single technologies cannot obtain complex structure arrays, such as re-entrant structure arrays. As a result, researchers have proposed hybrid technologies to fabricate complex structure arrays [80]. Overall, the fabrication methods for bio-inspired MAAMs-SW are diverse, with relatively mature formation mechanisms of the macrostructures. Several fabrication methods have been applied, achieving various economic and social benefits. The development of low-cost, efficient, and environmentally friendly methods for the large-scale fabrication of bio-inspired MAAMs-SW remains a popular subject. Nevertheless, because bio-inspired MAAMs-SW with poor mechanical and chemical stability cannot be implemented into practical applications, the strength and durability of fabricated surfaces should be fully considered when selecting the fabrication method.

## 5. Application of bio-inspired MAAMs-SW

Substantial progress has been made in recent years on MAAMs-SW research. In addition to exploring basic theory and fabrication technology, researchers have conducted a significant amount of work on studying the application fields and values of bio-inspired MAAMs-SW. As a result, an increasing number of applications of MAAMs-SW have emerged. This section introduces a few typical applications of bio-inspired MAAMs-SW, including liquid/droplet manipulation, water collection, oil–water separation, drag reduction, anti-icing, heat transfer, oil repellency, underwater air retention, smart wettability, and mechanical stability.

### 5.1. Liquid/droplet manipulation

Liquid/droplet manipulation technology has been widely used in many fields due to its diverse transport methods, high efficiency, and low losses, with applications in biology, chemistry, materials, and energy applications [16, 122, 219–221]. Liquid/droplet manipulation can be divided into active and passive strategies. In this section, we present the liquid/droplet manipulation of bio-inspired MAAMs-SW based on active and passive strategies.

#### 5.1.1. Liquid/droplet manipulation using active strategies.

An active strategy can realize programmable droplet manipulation with relatively fast and long-distance droplet transport by applying various external fields, such as electric, magnetic, or light fields [45, 222–229]. Zhang *et al* [230] fabricated a slippery macro ratchet array by using femtosecond laser ablation, which was combined with a vibration platform



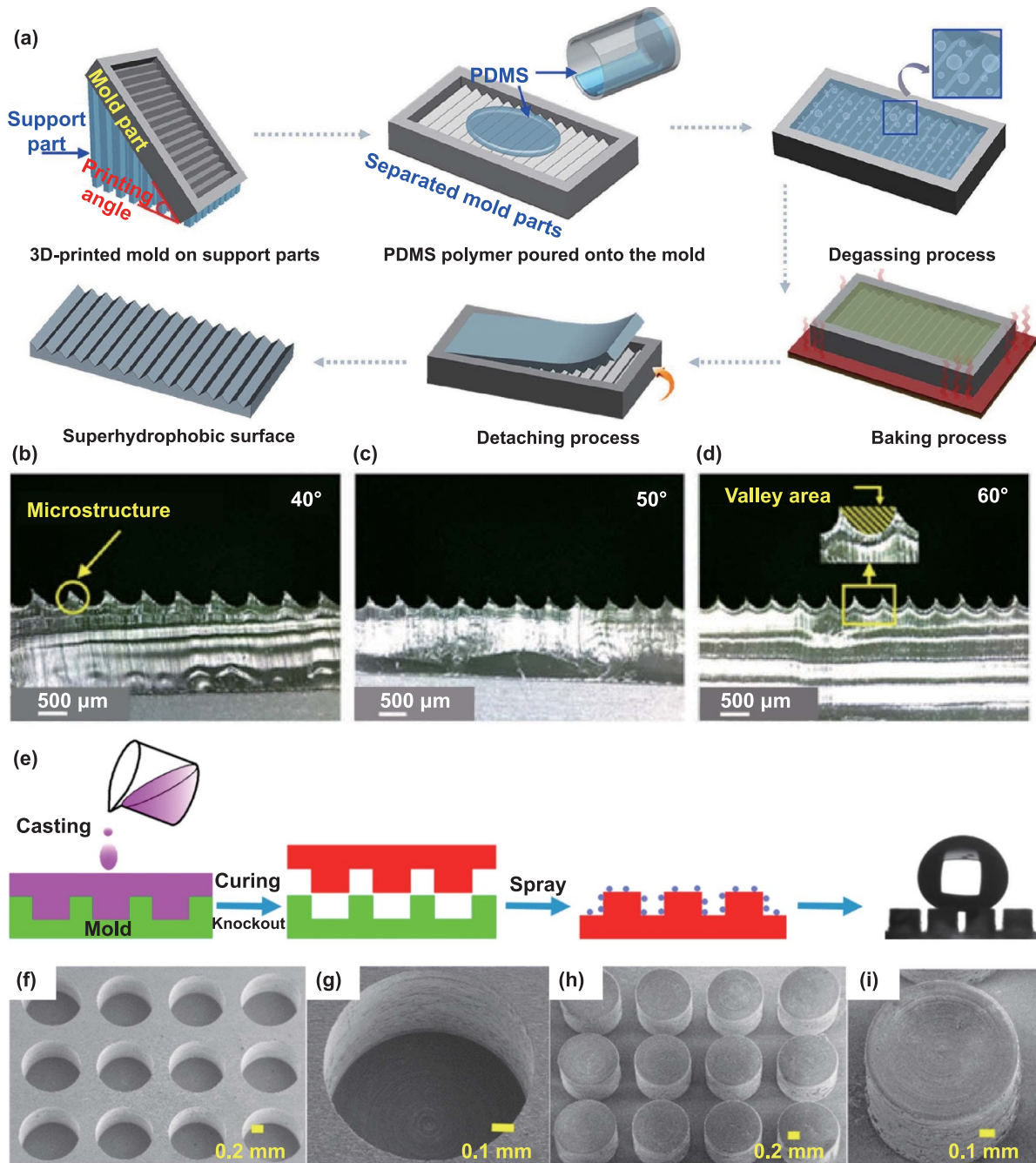


**Figure 16.** Superhydrophobic MAAs fabricated using the template method. (a) Schematic diagram of the fabrication process of a superhydrophobic polymer surface based on the template method. (b)–(d) Optical images of the polymer surface cast from the 3D-printed mold as a function of the printing angle from  $40^\circ$  to  $60^\circ$ . (a)–(d) Reproduced from [209], with permission from Springer Nature. (e) Fabrication process of the superhydrophobic pillar arrays using the template method. (f) and (g) SEM images of the blind hole arrays. (h) and (i) SEM images of the superhydrophobic pillar arrays. (e)–(i) Reprinted with permission from [210]. Copyright (2017) American Chemical Society.

to form a vibration-actuated omni-droplet rectifier (VAODR) (figure 18(a)). Water droplets ( $6 \mu\text{l}$ ) were placed on the VAODR and driven by horizontal vibrations for directional droplet transport with a climb angle of  $3.5^\circ$  (figure 18(b)). Figure 18(c) shows the SEM images of the macro ratchet arrays, where the depth  $D$  of each inclined ratchet was  $\sim 134 \mu\text{m}$ , the width  $W$  of the groove was  $\sim 174 \mu\text{m}$ , the period  $P$  was  $\sim 220 \mu\text{m}$ , and the oblique angle  $\gamma$  of each ratchet

was  $\sim 45^\circ$ . Subsequently, the ratchet arrays were infused with lubricant (silicone oil) to achieve slippery characteristics. Figure 18(d) shows the optical images of the slippery ratchet arrays with different oil film thicknesses. With a thin oil film, the lubricant partially covered the ratchet arrays, resulting in significant asymmetry of the VAODR. By contrast, with a thick oil film, the lubricant completely covered the ratchet arrays, and asymmetry was eliminated, which impaired the



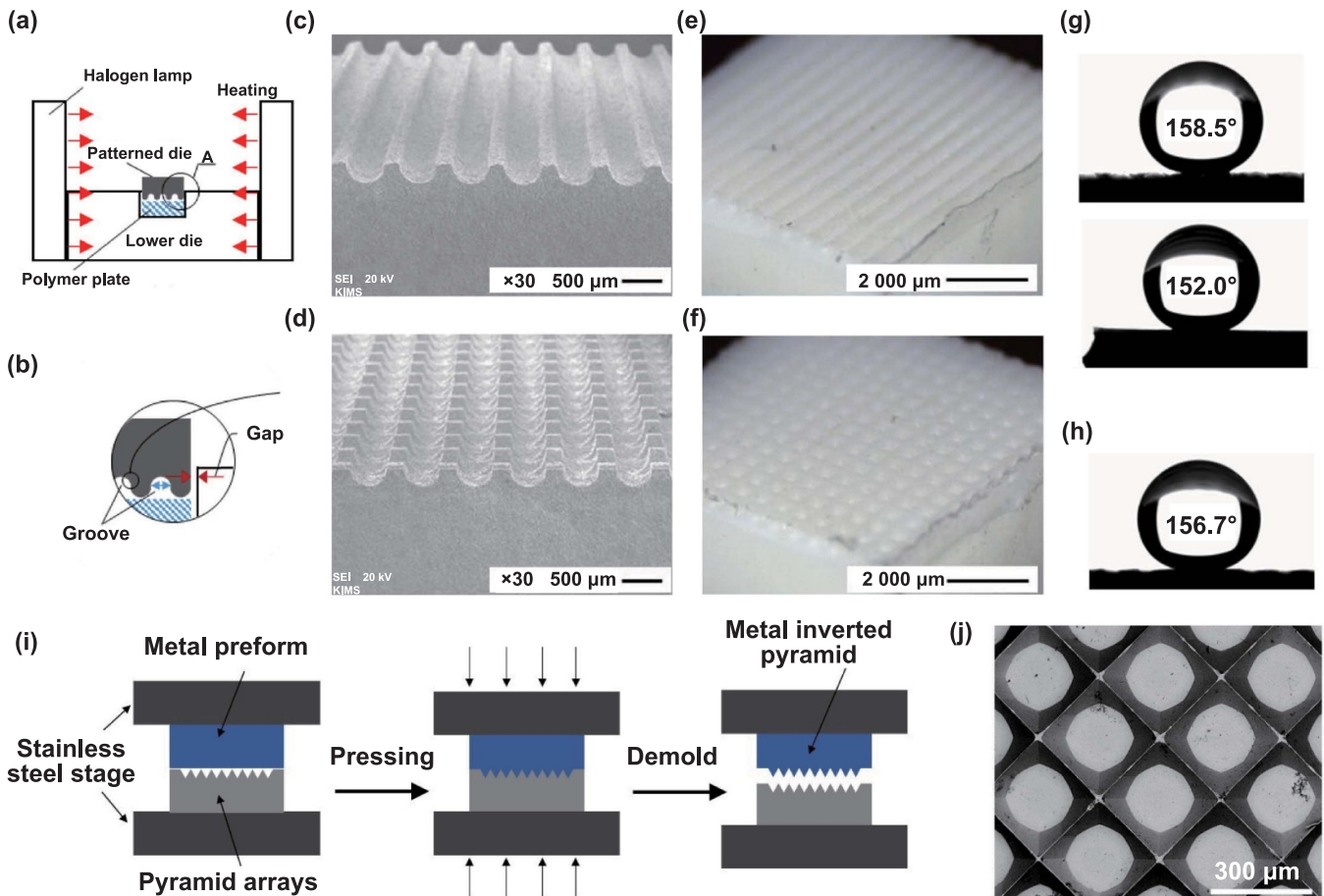


**Figure 17.** Superhydrophobic MAAs fabricated by imprinting method. (a) Schematic diagram of hot imprinting process. (b) Detailed view of 'A' in (a). (c) and (d) SEM images of the 2D/3D patterned dies. (e) and (f) Optical images of superhydrophobic PTFE polymer surfaces with 2D/3D patterns fabricated by hot imprinting. (g) Contact angles of the 2D patterned surface in parallel and perpendicular directions. (h) Contact angle of the 3D patterned surface. (a)–(h) Reproduced from [218], with permission from Springer Nature. (i) Fabrication process scheme of the inverted pyramid arrays. (j) SEM image of the inverted pyramid arrays on an iron substrate. (i) and (j) Reproduced from [98], with permission from Springer Nature.

directional transport of the droplets. By adjusting the thickness of the lubricant film from 10% to 93%, directional transport of droplets ((4–24)  $\mu\text{l}$ ) with different transport speeds was achieved (figure 18(e)).

External fields can also stimulate changes in the surface morphology to achieve droplet manipulation [103, 231–234]. Shao *et al* [235] proposed a slippery magnetic-responsive macro plate array with micro grooves for multi-substance transport, where the length  $L$ , height  $H$ , and thickness  $W$  of the macro plate array were  $\sim 4$  mm,  $\sim 1$  mm, and  $\sim 95$   $\mu\text{m}$ , respectively. In addition, the spacing  $D$  between the two macro plates was 400  $\mu\text{m}$  (figure 19(a)), and the micro groove spacing  $m$  and radius  $n$  were  $\sim 100$   $\mu\text{m}$  and  $\sim 50$   $\mu\text{m}$ , respectively. After injection with dimethyl silicone oil, the surface exhibited slippery characteristics, where the underwater sliding angle of the air bubble was 31.2°, and the sliding angle of the water droplet was 6.3°. The macro plate array could bend along the direction of the magnetic field due to the internal carbonyl iron particle chains. Under the action of a magnetic field, the slippery surface realized the on-demand transport of air bubble (under water), water droplet (in air), and

glass-ball (in air) (figures 19(b)–(d)). Jing *et al* [228] reported a superhydrophobic magnetic macro pillar array for multi-dimensional droplet manipulation under a low magnetic field (figure 19(e)) and analyzed the transport mechanism and state of the water droplet under weak/strong magnetic fields and different magnetic field velocities (figure 19(f)). As shown in figure 19(g), to validate the model of the droplet transport, the real-time dynamic behaviors of the water droplet under different magnetic field velocities were studied. Finally, operating platforms based on the magnetic macro pillar array were established to demonstrate their precise 3D droplet manipulation capabilities.

### 5.1.2. Liquid/droplet manipulation using passive strategies.

On a surface with uniform structure and wettability, a liquid/droplet will not move. However, on an anisotropic surface, unbalanced interfacial tension will form between the liquid/droplet and the solid surface, causing the liquid/droplet to move [236]. Based on this passive strategy, bio-inspired geometrical anisotropic surfaces with MAAs have been

**Table 2.** Summary of various fabrication methods applied to bio-inspired MAAMs-SW.

| Strategies                |                                     | Efficiency | Cost  | Processing precision | Structural diversity | 3D processing flexibility | Scale flexibility | Applicable materials            |
|---------------------------|-------------------------------------|------------|-------|----------------------|----------------------|---------------------------|-------------------|---------------------------------|
| Additive manufacturing    | Fused deposition molding            | ☆☆☆        | ☆☆☆☆☆ | ☆☆☆☆                 | ☆☆☆☆                 | ☆☆☆☆                      | ☆☆☆☆☆             | Polymer, metal, ceramics        |
|                           | Selective laser sintering/melting   | ☆☆☆☆       | ☆☆    | ☆☆☆                  | ☆☆☆☆                 | ☆☆☆☆                      | ☆☆☆☆☆             | Polymer, metal, ceramics        |
|                           | Direct ink writing                  | ☆☆☆        | ☆☆☆☆  | ☆☆☆☆☆                | ☆☆☆☆                 | ☆☆☆☆☆                     | ☆☆☆               | Polymer, metal, ceramics        |
|                           | Stereolithography                   | ☆☆☆☆       | ☆☆☆☆  | ☆☆☆☆☆                | ☆☆☆☆☆                | ☆☆☆☆☆                     | ☆☆☆☆☆             | Polymer, ceramics               |
|                           | Projection micro stereolithography  | ☆☆☆☆       | ☆☆☆   | ☆☆☆☆                 | ☆☆☆☆☆                | ☆☆☆☆                      | ☆☆☆               | Polymer, metal, ceramics        |
| Subtractive manufacturing | Femtosecond laser                   | ☆☆         | ☆☆☆   | ☆☆☆☆☆                | ☆☆☆☆                 | ☆☆                        | ☆☆☆               | Polymer, metal, ceramics, glass |
|                           | Nanosecond laser                    | ☆☆☆☆       | ☆☆☆☆  | ☆☆☆                  | ☆☆☆☆                 | ☆☆                        | ☆☆☆☆              | Metal, ceramics                 |
|                           | Wire electrical discharge machining | ☆☆☆☆       | ☆☆☆   | ☆☆☆☆                 | ☆☆☆                  | ☆☆☆                       | ☆☆☆☆              | Metal, semiconductor            |
|                           | Micro-mechanical cutting machining  | ☆☆☆☆       | ☆☆☆☆  | ☆☆☆☆                 | ☆☆☆☆                 | ☆☆☆☆                      | ☆☆☆☆☆             | Polymer, metal                  |
|                           | Mask electrochemical machining      | ☆☆         | ☆☆☆☆  | ☆☆☆                  | ☆☆                   | ☆                         | ☆☆☆               | Metal                           |
|                           | Maskless electrochemical machining  | ☆☆☆☆       | ☆☆☆   | ☆☆☆☆                 | ☆☆☆☆                 | ☆☆☆                       | ☆☆☆☆              | Metal                           |
| Formative manufacturing   | Template method                     | ☆☆☆☆       | ☆☆☆☆☆ | ☆☆☆☆                 | ☆☆☆☆                 | ☆☆☆                       | ☆☆☆☆              | Polymer, metal                  |
|                           | Imprinting method                   | ☆☆☆        | ☆☆☆☆  | ☆☆☆☆                 | ☆☆☆                  | ☆☆☆                       | ☆☆☆☆              | Polymer, metal, glass           |

Notes: more stars mean higher efficiency/lower cost/higher processing precision/better structural diversity/higher 3D processing flexibility/higher scale flexibility, and the same number of stars indicates similar efficiency/cost/processing precision/structural diversity/3D processing flexibility/scale flexibility.

widely used for liquid/droplet manipulation. For example, Li *et al* [133] fabricated a peristome-mimicking surface with macro cavity arrays using high-resolution stereo-lithography (figures 20(a) and (b)). The macro cavity structure had a length of 700  $\mu\text{m}$ , width of 250  $\mu\text{m}$ , and depth of 150  $\mu\text{m}$ , and was periodically arranged along the axial direction. As shown in figure 20(c), when dyed water was continuously dropped onto the peristome-mimicking surface, the water spread along the macro cavity arrays in one direction. Feng *et al* [70] used 3D printing technology to fabricate pine needle-inspired asymmetric arrays with a periodicity of 1.5 mm. The pine needle-inspired asymmetric arrays were composed of Janus pillars with a distance  $s$  of 300  $\mu\text{m}$  and a height gradient  $\alpha$  of 3.5°. After placing the arrays in a humid chamber, the water droplets automatically advanced after continuously coalescing due to

the TIF of the droplets on the Janus pillars. Subsequently, they [71] fabricated an Araucaria leaf-inspired surface using 3D printing technology. The macrostructure of the Araucaria leaf-inspired surface was composed of multiple rows of parallel ratchet arrays with a row-to-row width of approximately 1000  $\mu\text{m}$ , an interside-to-interside width of 400  $\mu\text{m}$ , and a tip-to-tip pitch of 750  $\mu\text{m}$  (figure 20(d)). On the Araucaria leaf-inspired surface, the transport directions of the water-ethanol mixtures with different mass fractions of ethanol ( $c$ ) differed. For example, a mixture with  $c = 40\%$  was transported forward (figure 20(e)), while a mixture with  $c = 10\%$  was transported backward (figure 20(f)).

In addition to investigating the directional transport of droplets, exploring the dynamic bouncing behavior of droplets holds significant potential for advancing droplet manipulation

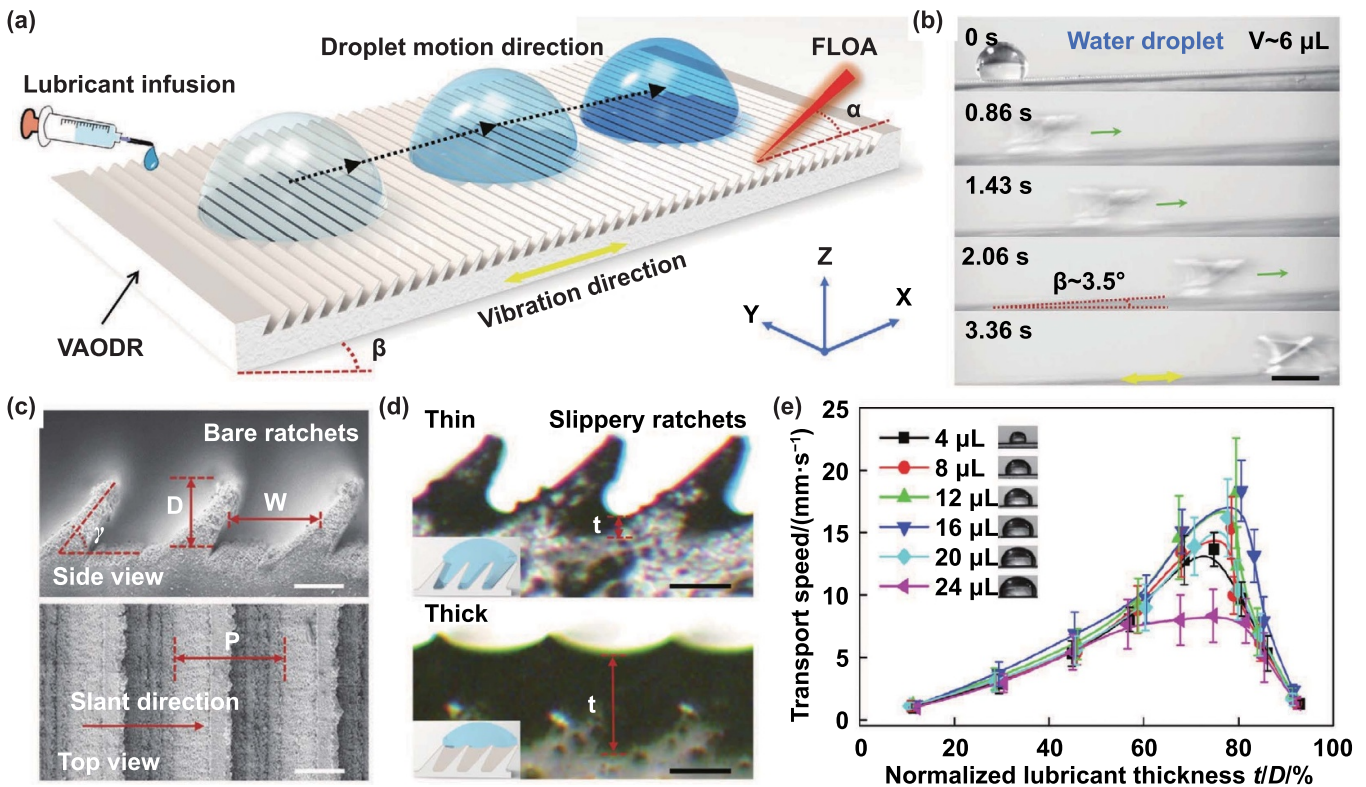


**Figure 18.** Unidirectional transport of water droplets on the VAODR. (a) Schematic illustration of the directional droplet transport process under vibration. (b) Water droplet transport on the slippery ratchets at a climbing angle of  $\sim 3.5^\circ$  (scale bar: 3 mm). (c) Side and top SEM images of anisotropic bare ratchets (scale bar: 100  $\mu\text{m}$ ). (d) Optical images of the slippery ratchet arrays with different oil film thicknesses, where the insets show the corresponding schematic diagrams of droplets on slippery ratchet arrays with different oil film thicknesses (scale bar: 50  $\mu\text{m}$ ). (e) Transport speed of the water droplets with different volumes and oil film thicknesses. [230] John Wiley & Sons. © 2022 Wiley-VCH GmbH.

based on passive strategies [237–239]. Superhydrophobic MAAs with reduced liquid-solid contact time offer significant potential applications in preventing icing on aircraft wings. Liu *et al* [99] fabricated a post surface using a wire cutting machine followed by chemical etching (figure 21(a)), where the center distance and height of the post were 200  $\mu\text{m}$  and 800  $\mu\text{m}$ , respectively. After chemical modification, the post surface demonstrated superhydrophobicity with a contact angle of greater than  $165^\circ$  (figure 21(b)). With a Weber (We) number of 7.1, the dynamic bouncing behavior of the water droplet on the post surface was normal, and the contact time was 16.5 ms (figure 21(c)). However, at a higher We (14.1), the droplet exhibited pancake-like bouncing behavior (figure 21(d)), and the contact time between the droplet and the post surface was significantly reduced. Song *et al* [100] used 3D printing technology to fabricate macro and micro anisotropic superhydrophobic surfaces and assessed their dynamic impact behavior. Impacts on the micro anisotropic superhydrophobic surface generated round-like spreading and recoiling (figure 21(e)). However, impacts on the macro anisotropic superhydrophobic surface showed more curved spreading, with a flying-eagle shape (figure 21(f)). The macro anisotropic superhydrophobic surface also reduced the contact time of the impact droplets by 40%–50%.

## 5.2. Water collection

With the extreme global scarcity of freshwater resources, the efficient and environmentally friendly acquisition of freshwater resources has become a significant concern. Recently, bio-inspired water collection materials have received increasing attention due to their cost effectiveness, long life, and environmentally friendly characteristics [61, 135, 240–244]. Zhou *et al* [114] fabricated desert beetle-inspired superhydrophobic–hydrophilic surfaces with macro/nano-structures. The top of the inspired macro pillars exhibited hydrophilicity, while the remaining surface areas exhibited superhydrophobicity. This combination of superhydrophobicity and hydrophilicity yielded excellent performance in accelerating droplet condensation and aggregation (figure 22(a)), endowing the surface with excellent water collection performance (figure 22(b)). Inspired by scallop shells, Bai *et al* [241] developed a superhydrophilic origami with multiple-paratactic and dual-asymmetric macro channels, which could guide the anti-gravity, directional, and spontaneous transport of water from the wide channel to the narrow channel (figures 22(c) and (d)). The synergistic effect of geometric gradients and superhydrophilicity significantly improved the water harvesting capacity. Park *et al* [90] combined the wetting properties of Namib Desert beetles,



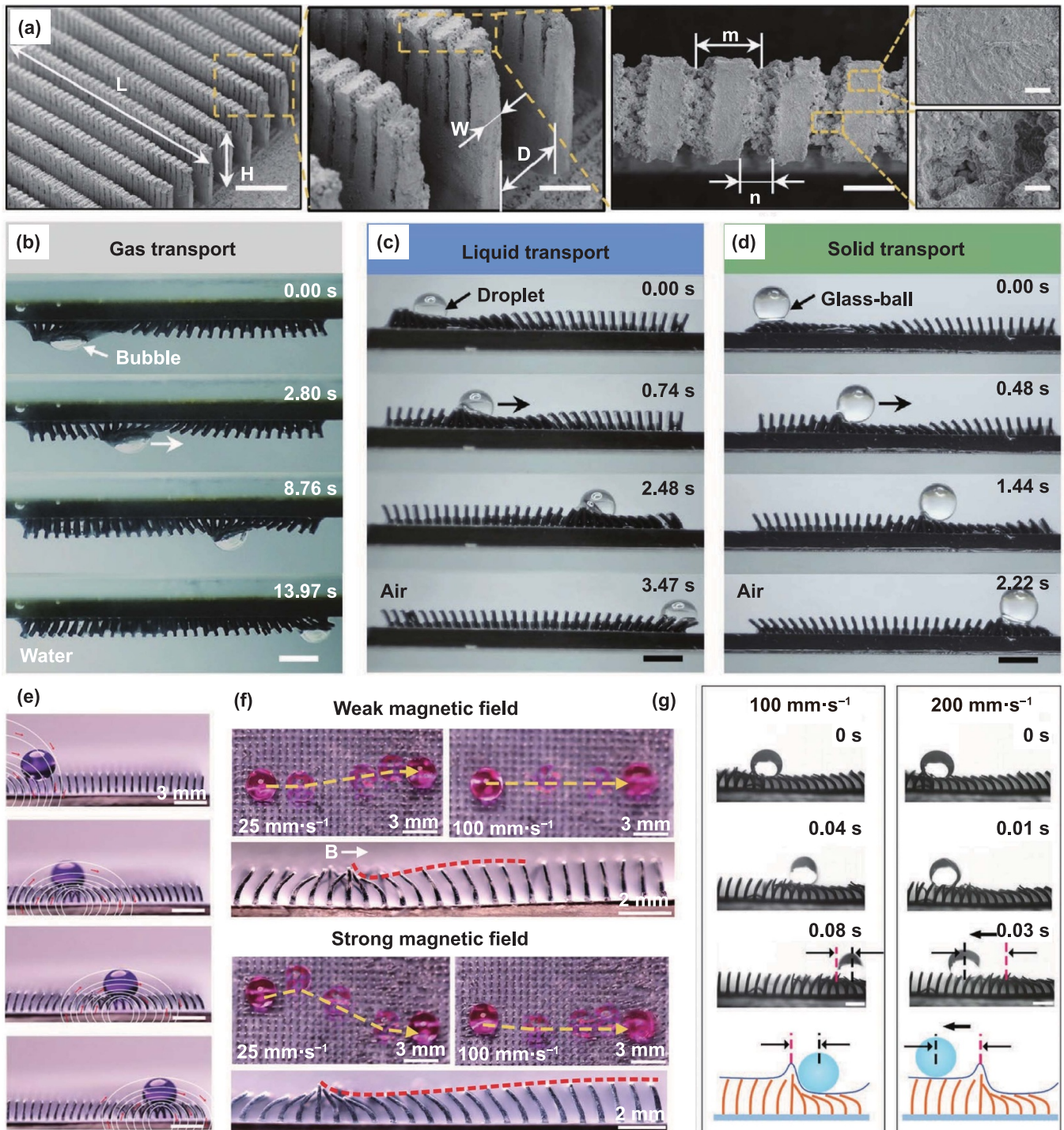


**Figure 19.** Droplet manipulation on MAAMs-SW under the action of a magnetic field. (a) SEM image of the macro plate array with micro grooves (scale bars from left to right: 700, 200, 70, and 10  $\mu\text{m}$ ). (b)–(d) Optical images showing on-demand transport of an air bubble (under water), water droplet (in air), and glass-ball (in air) (scale bar: 2 mm). (a)–(d) [235] John Wiley & Sons. © 2022 Wiley-VCH GmbH. (e) Optical images of droplet transport on a superhydrophobic magnetic macro pillar array in the horizontal direction. (f) Transport state of the water droplet under weak/strong magnetic fields and with different magnetic field velocities. (g) Real-time dynamic behaviors of a water droplet under different magnetic field velocities. (e)–(g) [228] John Wiley & Sons. © 2022 The Authors. Advanced Functional Materials published by Wiley-VCH GmbH.

cacti, and *Nepenthes* pitcher plants to fabricate a slippery surface with an asymmetric bump structure array (figure 22(e)). Previous studies showed that the bump structures on the desert beetle elytra surface promoted the rapid condensation of water

vapor into droplets. By combining the bumps with the slope structure of cactus spines, and coupling the slippery properties of *Nepenthes* pitcher plants to the slope surface, the droplets could grow quickly and quickly leave the slope surface. The

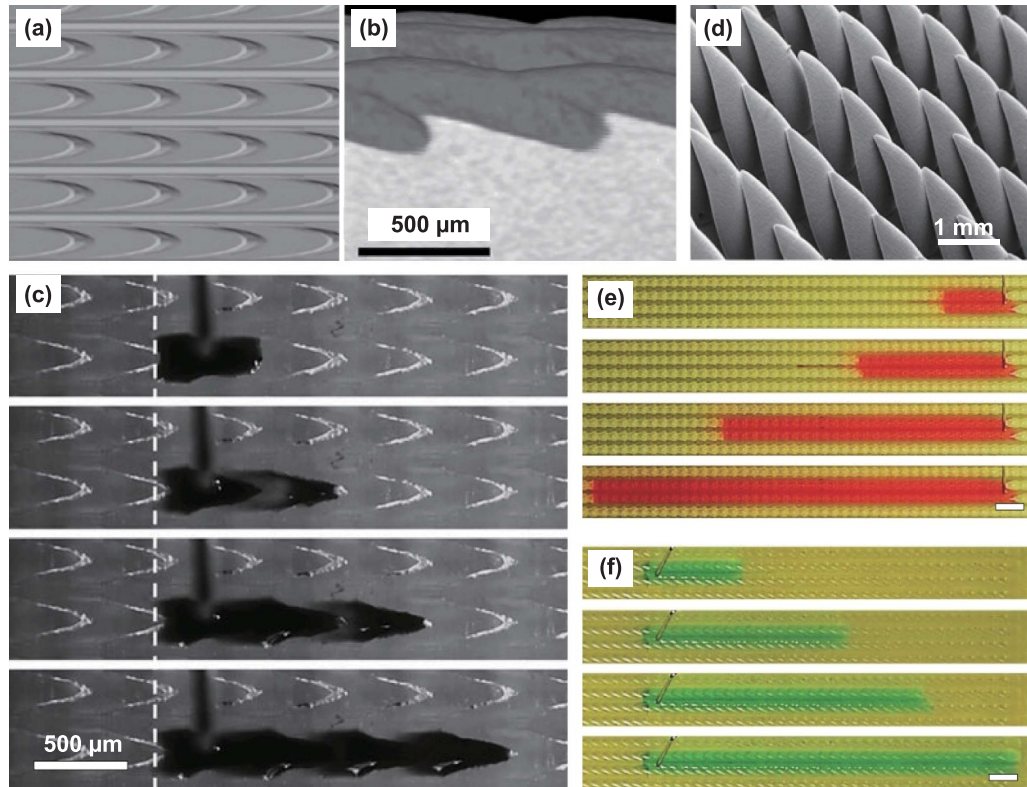


**Figure 20.** Liquid directional transport on MAAs based on the passive strategy. (a) and (b) Optical image and cross-sectional SEM image of the peristome-mimetic surface. (c) Unidirectional transport of dyed water on peristome-mimetic surface. (a)–(c) [133] John Wiley & Sons. © 2016 Wiley-VCH Verlag GmbH & Co. KGaA, Weinheim. (d) Macrostructures of the Araucaria leaf-inspired surface. (e) and (f) Transport of water–ethanol mixtures with  $c = 40\%$  (red liquid) and  $c = 10\%$  (green liquid) on the Araucaria leaf-inspired surface (scale bar: 2 mm). (d)–(f) Araucaria leaf: From [71]. Reprinted with permission from AAAS.

results showed that water collection on the slippery asymmetric bumps was significantly improved compared to flat slippery surfaces (figures 22(f) and (g)).

Special wettability behavior induced solely by MAAs has also been widely used for water collection. Tian *et al* [91] fabricated bio-inspired spindle-knot microfibers with cavity knots using a microfluidics method (figure 22(h)), and investigated the water collection performance of a typical single cavity-microfiber (figure 22(i)). The results showed that tiny water droplets increased in size due to continuous condensation and moved toward the spindle knot, forming a large water droplet, due to the difference in surface energy and Laplace pressure between the knots and joints. Over time, the water droplets collected on the knots moved toward the domain knot, and larger water droplets were collected (figure 22(j)). Subsequently, four fibers were assembled into a topological network for large-scale water collection (figure 22(k)), and the water collection volume of the network was 0.36 ml within 2 min under a fog flow of  $0.408 \text{ ml}\cdot\text{min}^{-1}$ . Shi *et al* [245] developed a hydrogel membrane with 3D macrostructures for all-day water collection. At night, the microstructures of the hydrogel membrane captured water droplets, while during the day, the hydrogel membrane acted as an interfacial solar steam generator, achieving a high evaporation rate (figure 22(l)). When this

membrane was used in a homemade rooftop water collection device, the volumes of water collected during day and night were  $\sim 170 \text{ ml}$  and  $\sim 70 \text{ ml}$ , respectively (figures 22(m) and (n)), demonstrating its potential for mitigating the issue of global water shortage.

### 5.3. Oil–water separation

Water is essential for human survival. However, increasing water pollution, especially due to oil leaks and oily sewage, has substantially harmed the environment and human health [246, 247]. Oil–water separation based on extreme wettability serves as an ideal strategy for solving these problems [59, 248–252]. Yang *et al* [77] used 3D printing technology to fabricate a superhydrophobic eggbeater structure inspired by *S. molesta* leaves, with the flat surface exhibiting hydrophilic and superoleophilic properties. After nanocoating, the flat surface demonstrated superhydrophobic and oleophobic properties, the 3D-printed pillar arrays exhibited hydrophobic and oleophilic properties (figure 23(a)), and the eggbeater structure arrays had superhydrophobic and oleophilic properties (figures 23(a) and (b)). Based on the unique wettability and morphology of the surface, the eggbeater structure arrays were used for oil–water separation, with dyed oil (6 mg)



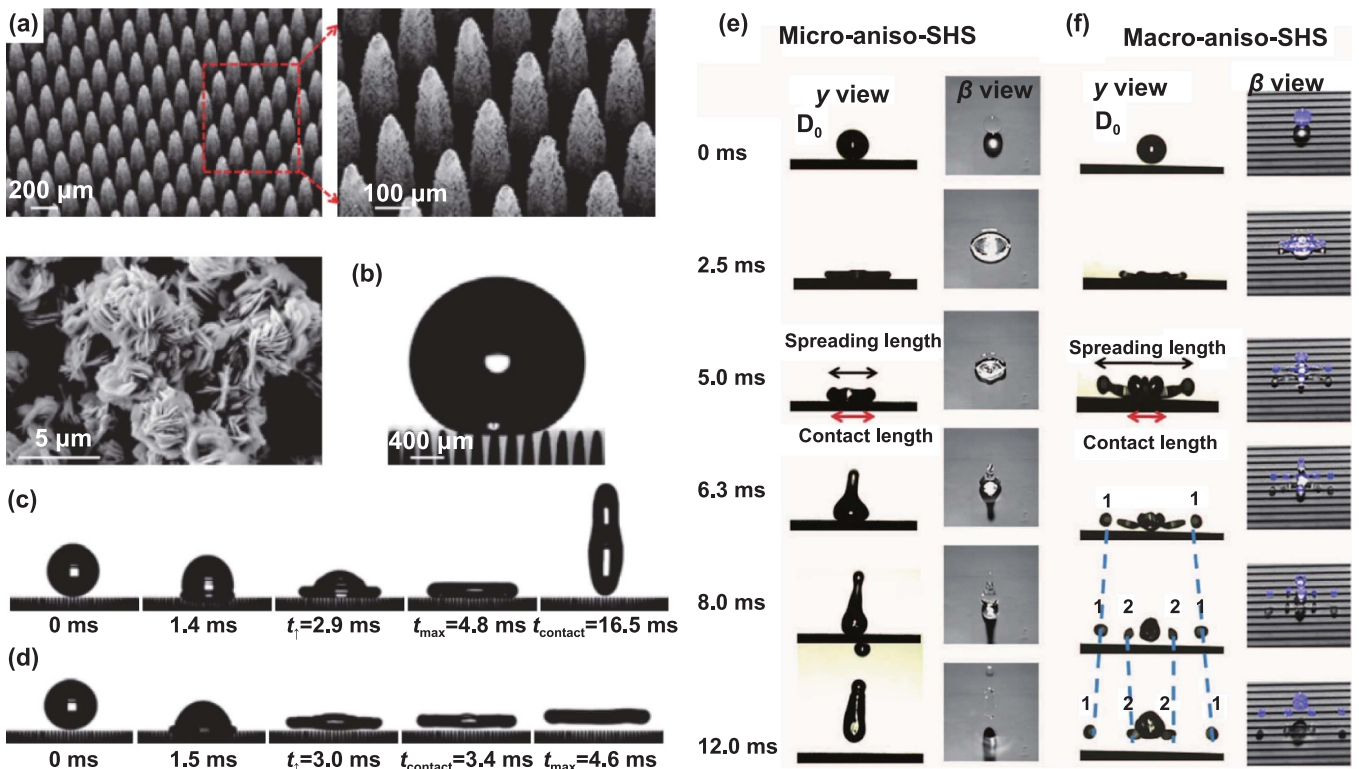


**Figure 21.** Dynamic bouncing behavior of droplets on superhydrophobic MAAs. (a) SEM images of a post surface. (b) Water droplet on the post surface with a contact angle of greater than  $165^\circ$ . (c) Water droplet impacting on a post surface at  $We = 7.1$ . (d) Water droplet impacting the post surface at  $We = 14.1$ . (a)–(d) Reproduced from [99], with permission from Springer Nature. (e) and (f) Impacts on the micro anisotropic superhydrophobic surface (micro-aniso-SHS) and macro anisotropic superhydrophobic surface (macro-aniso-SHS). (e)–(f) Reproduced from [100]. [CC BY 4.0](https://creativecommons.org/licenses/by/4.0/).

absorbed by the eggbeater structure within 1 s (figure 23(c)). When a droplet of the water/oil mixture was dropped onto the array, the wetting phase (oil) was merged into the eggbeater structure, and the non-wetting phase (water) remained on top, forming a spheroid shape (figure 23(d)). The oil–water separation efficiency, which was tested by thermogravimetric analysis, was 99.9%. Li *et al* [92] created an underwater cactus-inspired system and fabricated novel oleophilic PDMS needle arrays to separate oil droplets from an oil–water mixture, and figure 23(e) presents the SEM image of the PDMS needle arrays. The oil collection process on a single needle structure was analyzed, as shown in figure 23(f). The oil collection on the conical needle was achieved in three steps, namely, deposition, growth, and self-driving movement. The self-driving movement was caused by a Laplace pressure difference. As shown in figure 23(g), the oil–water mixture was successfully separated with the collection device. Figures 23(h)–(j) presents the images of the oil–water mixture, collected oil, and collected water before and after the separation experiment. The maximum collection efficiency of the PDMS needle arrays reached approximately 99%. In addition to the above studies, many sub-millimeter-scale holes [151, 253] or groove arrays [254] with special wettability have been used to separate oil–water mixtures. Therefore, bio-inspired MAAMs-SW may play an indispensable role in the field of oil–water separation.

#### 5.4. Drag reduction

The global energy crisis has intensified since the 1970s, resulting in the increasing development of various new energy conservation and emission reduction technologies [255]. Among these, drag reduction technology has shown significant application demand in underwater vehicles, ships, and long-distance pipeline transport [58, 141, 256]. Inspired by shark skin and fish scale surface structures and the superhydrophobicity of lotus leaf surfaces, researchers have developed numerous MAAMs-SW for drag reduction [94, 162, 257–261]. Kim *et al* [259] fabricated Salvinia-inspired surfaces using a conventional soft lithography method, supported by capillary-force-induced clustering (figures 24(a) and (b)). Macro pillars with a clustered structure were arrayed with a period of  $350 \mu\text{m}$ , and the contact angle was  $(174.9^\circ \pm 3.2^\circ)$  (figures 24(c) and (d)), resulting in excellent superhydrophobicity. The clustered surface structure could pull the meniscus of water, due to the hydrophilic tips of the polydopamine coating (figure 24(e)). To calculate the effective slip length and quantitatively evaluate the drag reduction effect of the Salvinia-inspired surface, the apparent viscosity of 40 wt% glycerol was measured on the surface and the reference plate (figure 24(f)). According to the results, the drag reduction of the Salvinia-inspired surface was  $\sim 82\%$ . According to the macro-morphology of *Sciaenops ocellatus* scales (figures 24(g) and (h)), Wang *et al*



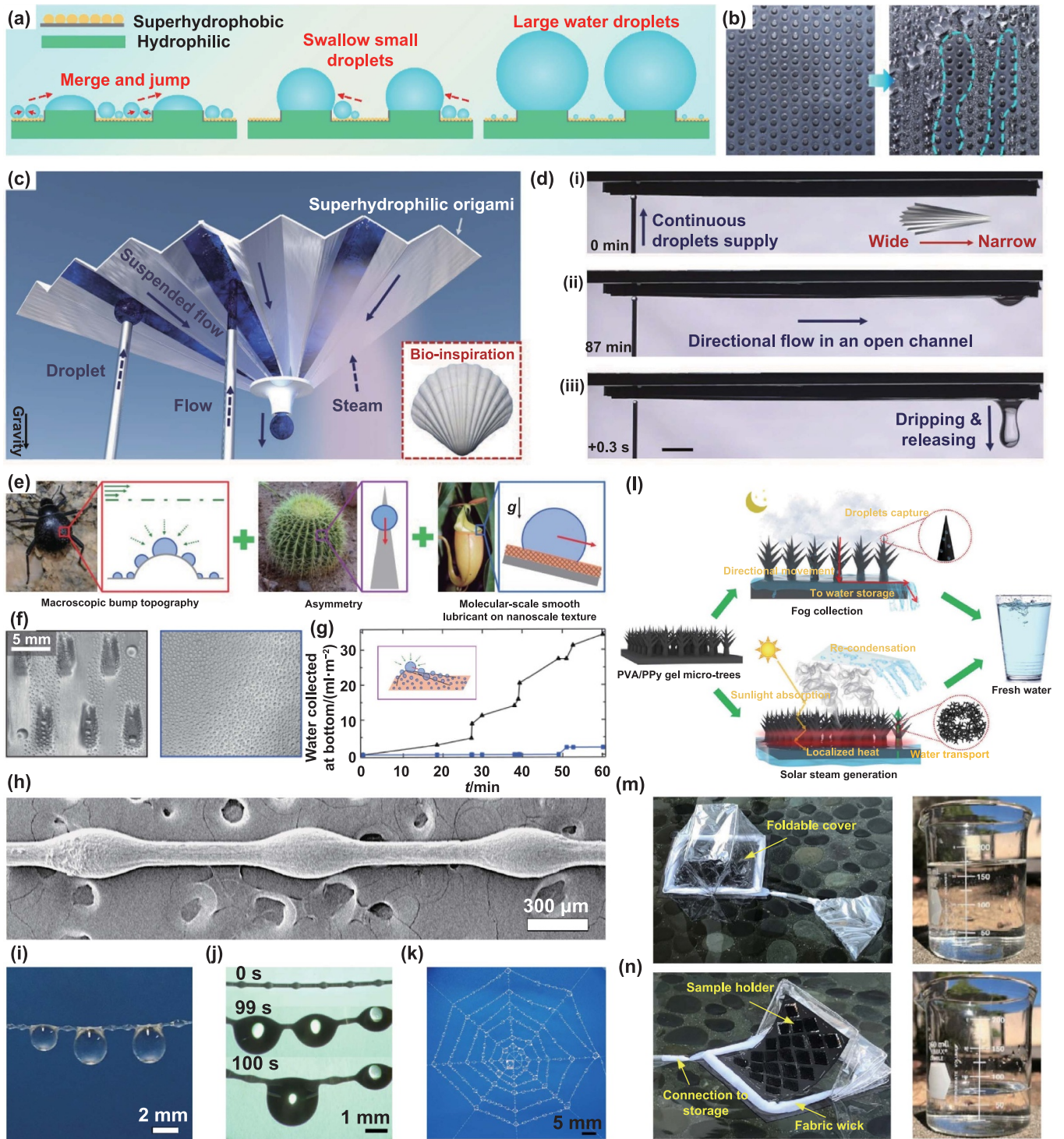


**Figure 22.** Water collection performances of bio-inspired MAAMs-SW. (a) Schematic diagram of the water collection mechanism on the inspired superhydrophobic–hydrophilic surface with macro pillars. (b) Water collection process on the superhydrophobic–hydrophilic surface. (a) and (b) Reprinted from [114], © 2022 Elsevier B.V. All rights reserved. (c) Schematic illustration of anti-gravity, directional, and spontaneous transport of water. (d) Directional liquid transport on superhydrophilic origami without leakage. (c) and (d) [241] John Wiley & Sons. © 2023 Wiley-VCH GmbH. (e) Design of a slippery surface with an asymmetric bump structure array. (f) and (g) Water collection images and curve of slippery asymmetric bumps (left image, black line in the plot) and flat slippery surface (right image, blue line in the plot). (e)–(g) Reproduced from [90], with permission from Springer Nature. (h) SEM image of a bio-inspired spindle-knot microfiber with cavity knots. (i) Optical image of water droplets collected on a single cavity-microfiber. (j) Water droplet on the knots moving toward a domain knot. (k) Topological network with four fibers for large-scale water collection. (h)–(k) Reproduced from [91]. CC BY 4.0. (l) Schematic diagram of all-day water collection of hydrogel membrane with macrostructures. (m) Daytime and (n) nighttime modes of a water collection prototype, and the corresponding collected water volume. (l)–(n) Reprinted from [245]. CC BY 4.0.



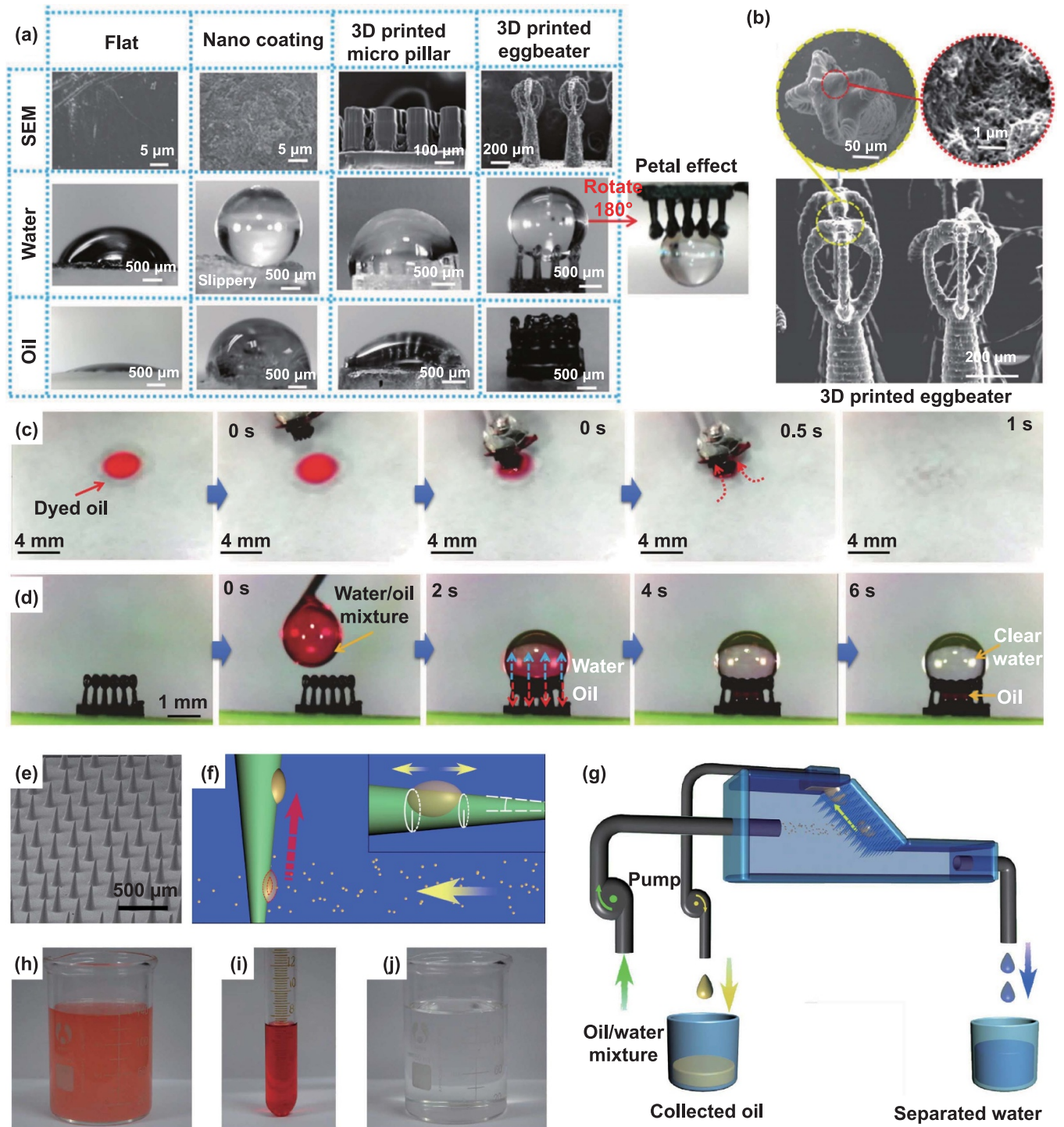


**Figure 23.** Oil–water separation performances of bio-inspired MAAMs-SW. (a) Water and oil on the flat surface, nanocoating surface, micro pillar surface, and eggbeater surface. (b) SEM images of 3D-printed eggbeater arrays. (c) Oil absorption of eggbeater structures. (d) Oil/water mixture separation of eggbeater structures. (a)–(d) [77] John Wiley & Sons. © 2018 WILEY-VCH Verlag GmbH & Co. KGaA, Weinheim. (e) SEM image of PDMS needle arrays. (f) Schematic diagram of the oil collection process. (g) Schematic diagram of the collection device. (h) Oil/water mixture. (i) Collected oil. (j) Separated water. (e)–(j) Reproduced from [92], with permission from Springer Nature.

[260] used a nanosecond laser to fabricate a bionic superhydrophobic fish-scale surface on an aluminum alloy, and figure 24(i) presents the morphology of the designed bionic fish-scale surface. Under the action of nanosecond laser, the morphology of *S. ocellatus* scales was successfully obtained

(the inset of figure 24(j)). The fabricated fish-scale surface exhibited excellent superhydrophobicity and low adhesion, and the experimental results showed that the drag reduction rate of the bionic fish-scale surface could reach ~4.8% under stratified conditions (figure 24(j)).

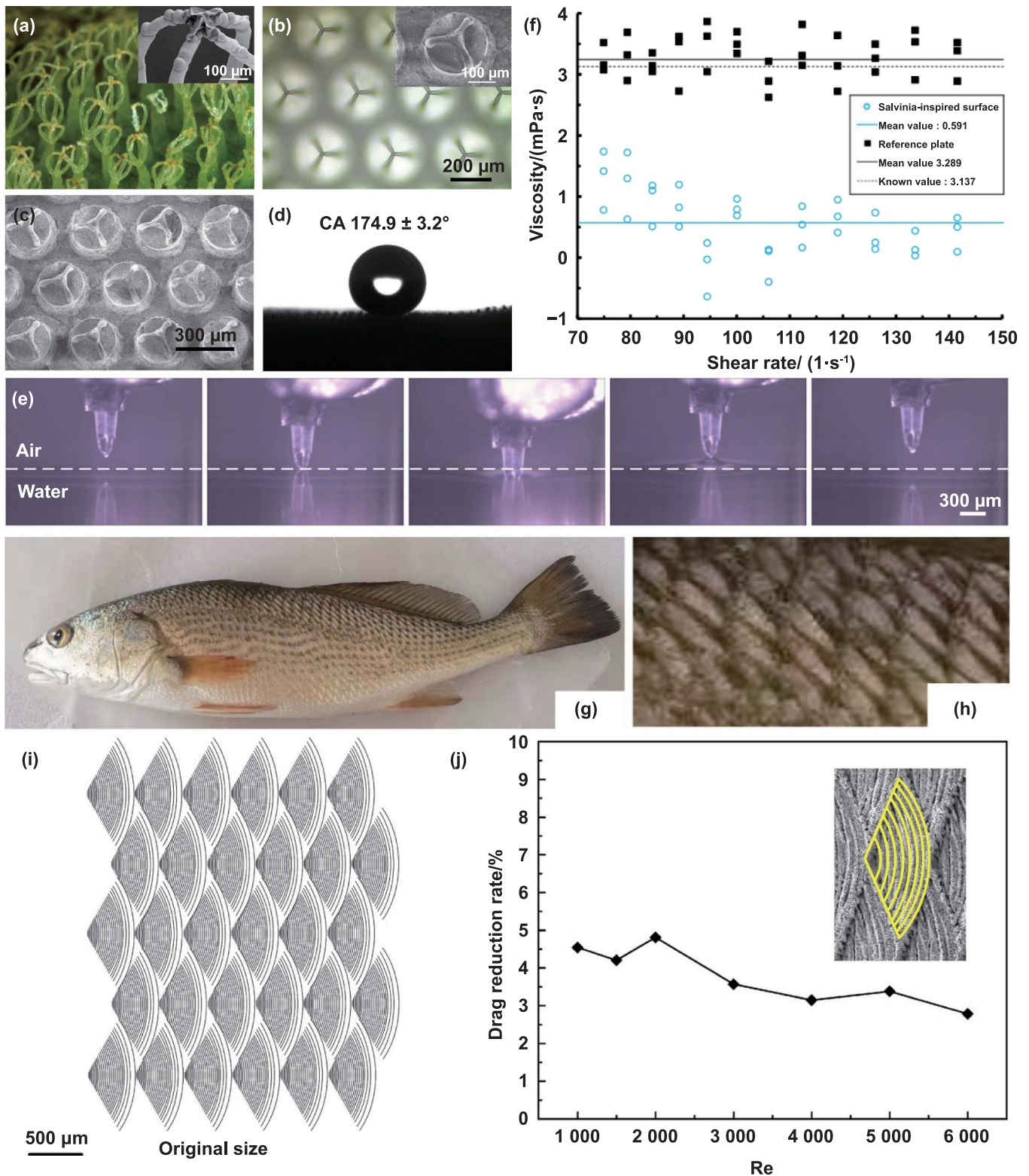


**Figure 24.** MAAMs-SW for drag reduction. (a) Salvinia leaves. (b) Salvinia-inspired macrostructures. (c) SEM image of the Salvinia-inspired surface. (d) Water droplet on the Salvinia-inspired surface showing superhydrophobicity. (e) Microscopic images of a single clustered structure pushing and pulling. (f) Apparent viscosity of 40 wt% glycerol on the reference plate and the Salvinia-inspired surface. (a)–(f) Reproduced from [259]. CC BY 4.0. (g) *Sciaenops ocellatus*. (h) Optical image of the scale arrangement of the fish. (i) Design of the morphology of the bionic fish-scale surface. (j) Experimental results on the drag reduction performance of the bionic fish-scale surface with different Re values. (g)–(j) Reprinted from [260], © 2021 Elsevier B.V. All rights reserved.



### 5.5. Anti-icing

Icing poses significant challenges across various domains, resulting in undesirable icing on the surfaces of power transmission equipment, aircraft, ships, roads, and other objects, leading to serious economic, energy, and security problems, as well as environmental hazards. Therefore, finding strategies to prevent icing has become an active research topic. Superhydrophobic materials have been widely used in the field of anti-icing [262–265]. For the study of superhydrophobic surfaces with MAAs, Guo *et al* [87] fabricated a macro/nanostructured surface (MN-surface), nanostructured surface (N-surface), macrostructured surface (M-surface), and smooth surface (S-surface). The MN-surface was composed of macro ratchet arrays with a period of 300  $\mu\text{m}$  and ZnO nanohairs with a diameter of 70–100 nm and a height of  $\sim 3 \mu\text{m}$  (figure 25(a)). The N-surface was composed of only ZnO nanohairs (figure 25(b)), and the M-surface was composed of only macro ratchet arrays with a period of 260  $\mu\text{m}$  (figure 25(c)). The S-surface was smooth without any additional structures (figure 25(d)). Figure 25(e) shows the ice formation processes on the MN-, N-, M- and S-surfaces at  $-10^\circ\text{C}$ , indicating that the MN-surface had robust anti-icing properties, which were significantly better than the anti-icing properties of the N-, M-, and S-surfaces. The time required for a droplet to freeze on the MN-surface was  $\sim 7220$  s, while the delay time on the N-surface was  $\sim 1740$  s. The inhibition of condensation frosting plays a critical role in anti-icing applications. Lu *et al* [266] reported a frost-free zone generated on a macro-ridged surface with hydrophobicity. Due to changes in the distribution of vapor diffusion flux, the designed macro ridge caused the condensate droplets to become arranged in a gradient based on their size during the condensation process (figures 25(f) and (g)), and this unique droplet distribution created a frost-free zone around the ridge corner. Based on this discovery, the macro ridge array was designed to achieve overall anti-frosting performance. The results showed that the middle area between the two ridges remained frost free on the surface of the macro ridge array with a period of 4 mm, while frost formed at a period of 5 mm (figures 25(h) and (i)). This strategy could serve as a new path for developing anti-icing surfaces.

### 5.6. Heat transfer

Improving heat transfer efficiency holds great significance for energy conservation and environmental protection. Dropwise condensation, known for its high heat transfer efficiency, has emerged as an attractive heat transfer method, with dropwise condensation on superhydrophobic surfaces gaining significant research attention [184, 267–270]. Droplets will show different states during condensation, and significantly different heat transfer effects on superhydrophobic surfaces with different structures and morphologies. Cheng *et al* [89] developed a macro-textured groove array on a high-purity copper plate through mechanical processing, and prepared nanostructures on an array via wet etching. Figure 26(a) shows an SEM image of the nanosheets distributed on the surface. The surface exhibited excellent superhydrophobicity

with a contact angle of  $154^\circ$ . Figures 26(b) and (c) shows the SEM images of the macro-textured groove array with opening angles of  $30^\circ$  and  $60^\circ$ , denoted as MGA30 and MGA60, respectively, and the heights of the grooves were 1.0 mm. As shown in figures 26(d) and (e), when the surface undercooling temperature ( $T$ ) was  $50.3^\circ\text{C}$ , the jumping departure modes of MGA30 and MGA60 were cut off and transformed into sweeping and sliding modes, respectively. The departure speed of sweeping on MGA30 was significantly larger than sliding on MGA60. Through experimentation, the study concluded that the introduction of macro-textured groove arrays realized preferential nucleation, and enabled the large droplets to propel themselves to detach from the surface, resulting in an approximately 50% decrease in the maximum diameter of the droplets on the condensation surface. In addition, the superhydrophilic surface could provide cooling liquid to the heating area under the action of strong capillary forces, thereby improving boiling heat transfer [271, 272]. Wang *et al* [272] fabricated a superhydrophilic macro/micro/nanostructured surface by combining hot embossing and hydrothermal treatment. The macro/micro/nanostructured surface was composed of macro groove arrays with a period of 1 mm (figure 26(f)), micro pyramid-channel arrays with a width of 100  $\mu\text{m}$  and a height of 173  $\mu\text{m}$ , and needle-shaped nanostructures with a length of several hundred nanometers. As shown in figure 26(g), the bubble behaviors of the different surfaces were analyzed. Based on figure 26(h), the contributions of the enhancement mechanisms of different surfaces based on the critical heat flux (CHF) and the experimental results showed that the macro/micro/nanostructured surface considerably improved the CHF and heat transfer coefficient. In addition, many MAAs with superhydrophobic–hydrophilic patterns have been used to enhance heat transfer [273, 274]. According to these studies, bio-inspired MAAMs-SW play an indispensable role in the field of heat transfer.

### 5.7. Oil repellency

Traditional superhydrophobic surfaces struggle to resist oil wetting [275], largely due to the low surface tension of oil, making it challenging to fabricate superoleophobic surfaces [107, 108]. The introduction of MAAs has been shown to increase oil repellency [276]. Yang *et al* [79] proposed a facile strategy for fabricating mushroom-like macrostructures based on the laser-induced self-growing method. As shown in figures 27(a) and (b), a re-entrant macro pillar was rapidly grown with continuous laser scanning within 0.36 s, corresponding to the intriguing growth of natural mushrooms. Figures 27(c) and (d) presents the fabricated re-entrant macro pillar array with good morphology uniformity, and after fluorination and spray coating, the surface exhibited oil repellency for hexadecane, olive oil, and ethylene glycol (figure 27(e)). Song *et al* [80] fabricated a superhydrophobic and superoleophobic macro-re-entrant structure using a mixed process of nanosecond laser ablation and liquid/gas interface shape-regulated electrochemical deposition. Figures 27(f) and (g) shows the SEM images of the macro-re-entrant structures

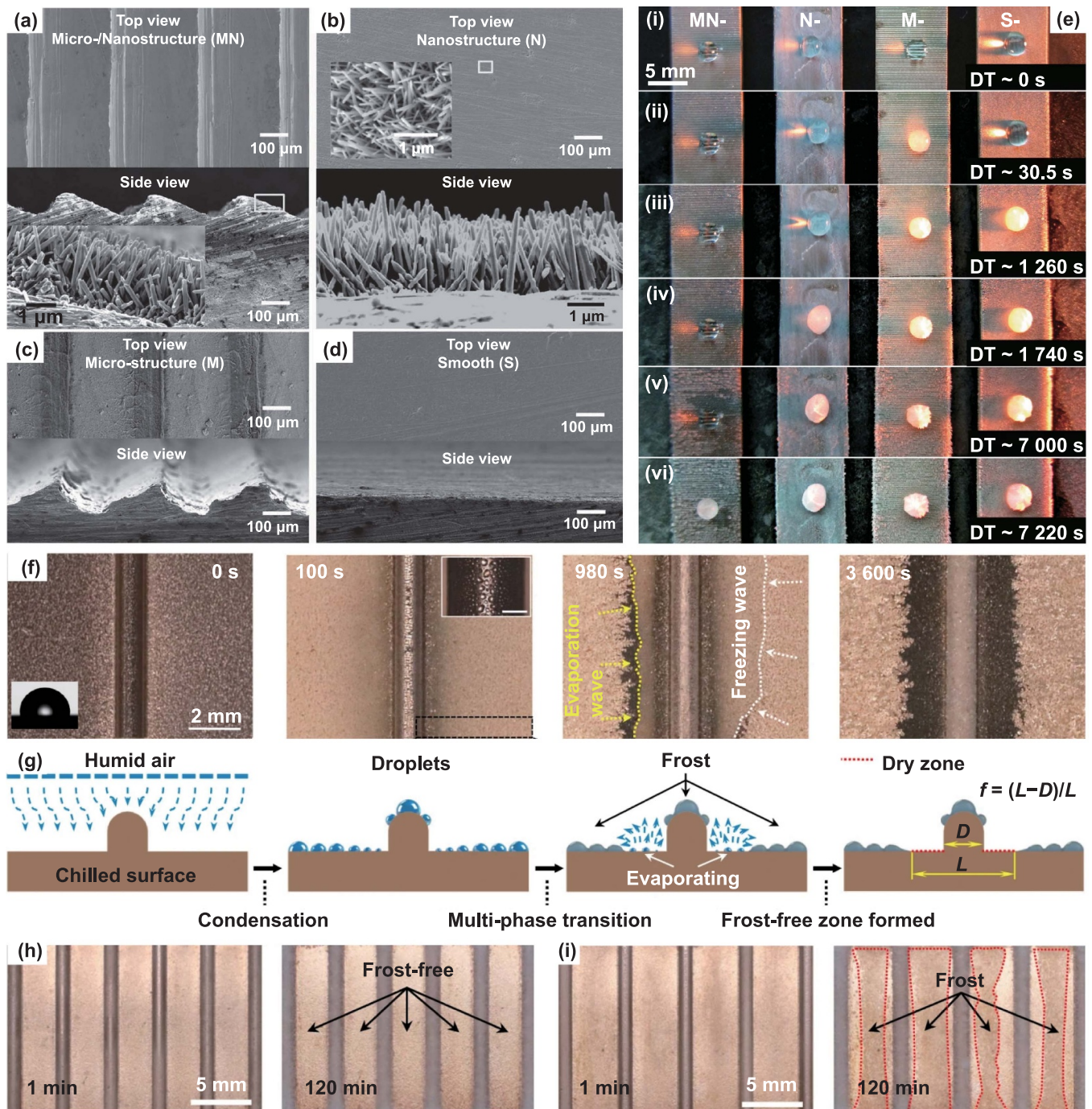


**Figure 25.** Anti-icing performances of MAAMs-SW. SEM images of different surfaces from top and side views. (a) MN-surface. (b) N-surface. (c) M-surface. (d) S-surface. (e) Ice formation processes on the MN-, N-, M-, and S-surfaces at  $-10^{\circ}\text{C}$  with delay time (DT). (a)–(e) [87] John Wiley & Sons. Copyright © 2012 WILEY-VCH Verlag GmbH & Co. KGaA, Weinheim. (f) Condensation frosting on a surface with a macro ridge. (g) Schematic diagram of the frost-free zone formed on a surface with a macro ridge at different stages. (h) and (i) Frosting results on the surfaces of macro ridge arrays with periods of 4 mm and 5 mm. (f)–(i) Reproduced from [266]. CC BY 4.0.

composed of roof-capped micropillars. After modification with low-surface-energy materials, the study observed that the contact angle of peanut oil droplets was  $156^{\circ}$  (figure 27(h)). However, when a peanut oil droplet was placed on the modified micropillar arrays without a roof structure, the droplet permeated into the spaces of the arrays, suggesting that the macro-re-entrant structure was essential for enhancing oil repellency (figure 27(i)). Yu *et al* [183] fabricated a macro

groove array via high-speed wire electrical discharge machining (figure 27(j)) and observed that the V-shaped groove array demonstrated enhanced oil repellency after immersion in a fluorosilane solution. The contact angles of glycerol and ethylene glycol increased from  $144.7^{\circ}$  and  $118.7^{\circ}$  to  $154.5^{\circ}$  and  $153.9^{\circ}$ , respectively (figure 27(k)), and the results showed that MAA helped to improve the oil repellency characteristics.



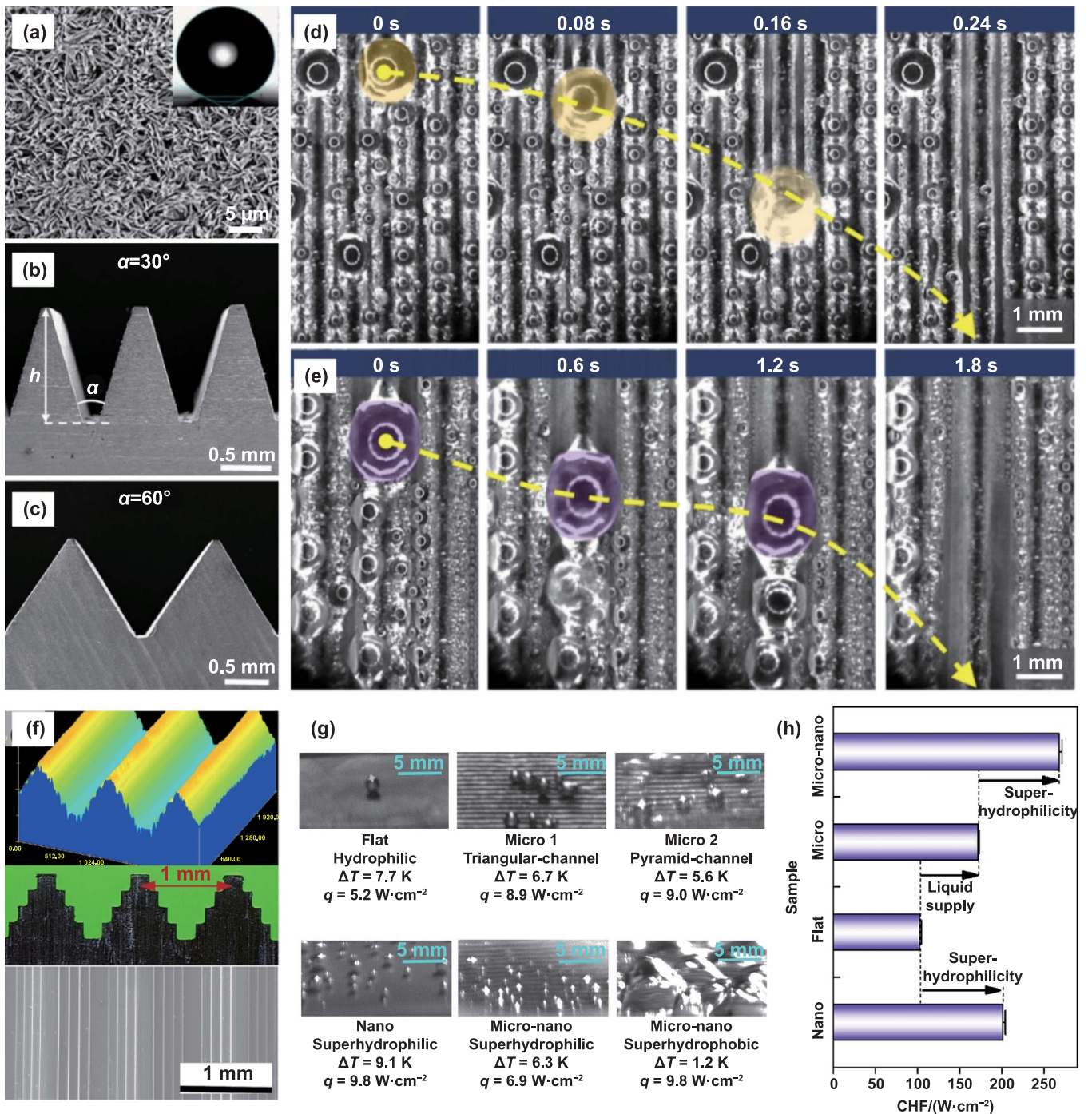


**Figure 26.** Condensation performances of MAAMs-SW. (a) SEM image of nanosheets distributed on the surface, where the inset shows the contact angle. (b) and (c) SEM images of MGA30 and MGA60. Vapor condensation on (d) MGA30 and (e) MGA60 with a high surface subcooling of 50.3 °C. (a)–(e) Reprinted from [89], © 2020 Elsevier B.V. All rights reserved. (f) Morphologies of fabricated macro groove arrays and micro pyramid-channel arrays. (g) Bubble behaviors of different surfaces. (h) CHF enhancement mechanisms of different surfaces. (f)–(h) Reprinted from [272], © 2023 Elsevier Ltd. All rights reserved.

5.8. Other applications

Apart from the above-mentioned applications, bio-inspired MAAMs-SW have demonstrated important applications in air retention under water [96, 277, 278], smart wettability [279–282], mechanical stability [98, 283, 284], and in other fields. Inspired by the long-term underwater air layer retention ability

of *S. molesta*, Zhang *et al* [96] developed a ‘top-constrained self-branching’ method to fabricate a superhydrophobic four-branch macrostructure, which was embedded with hydrophilic microspheres (figures 28(a)–(c)). The results showed that the fabricated *Salvinia*-inspired structure exhibited robust air retention and recovery abilities. Jiang *et al* [97] fabricated a Janus high aspect-ratio magnetically responsive microplate



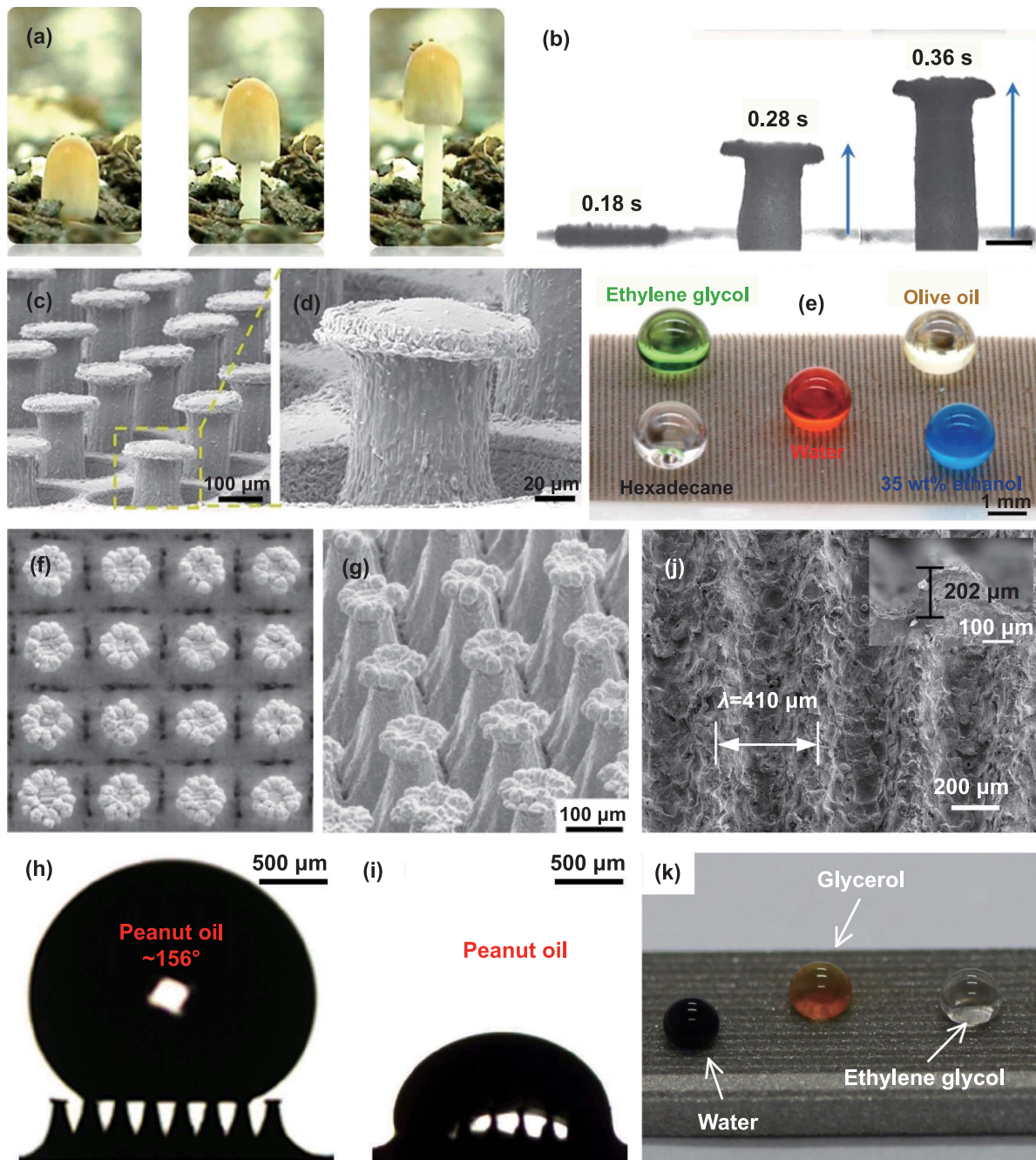


**Figure 27.** Enhanced oil repellency on MAAs. (a) and (b) Optical images of the growth of a re-entrant macro pillar corresponding to the growth process of a mushroom. (c) and (d) SEM images of the re-entrant macro pillar array. (e) Optical image of different liquid droplets on the re-entrant macro pillar array. (a)–(e) Reprinted with permission from [79]. Copyright (2021) American Chemical Society. (f) and (g) Top-view and side-view SEM images of macro-re-entrant structures. (h) Image of a peanut oil droplet on a superamphiphobic surface with roof structures. (i) Image of a peanut oil droplet on a superhydrophobic surface without roof structures. (f)–(i) Reprinted from [80], © 2020 Elsevier Ltd. All rights reserved. (j) SEM image of macro groove arrays. (k) Optical image of droplets of water, glycerol, and ethylene glycol on macro groove arrays. (j) and (k) Reprinted from [183], Copyright © 2015 Elsevier B.V. All rights reserved.

array (HAR-MMA) with smart wettability (figure 28(d)). The HAR-MMA had a height of  $\sim 940 \mu\text{m}$ , width of  $\sim 100 \mu\text{m}$ , length of  $\sim 2.1 \text{ mm}$ , and an interval of  $\sim 803 \mu\text{m}$ , and could switch between superhydrophobic ( $158^\circ$ ) and hydrophilic ( $40^\circ$ ) states by alternating the direction of the magnetic field (figure 28(e)). Based on the reversible switchable wettability,

a novel magnetically responsive water droplet switch was designed to realize the selective downward rolling or interception of water droplets (figure 28(f)). In addition, the HAR-MMA was used for dynamic color conversion and optical shutter driven by an external magnetic field (figures 28(g) and (h)). In practical applications, bio-inspired superhydrophobic

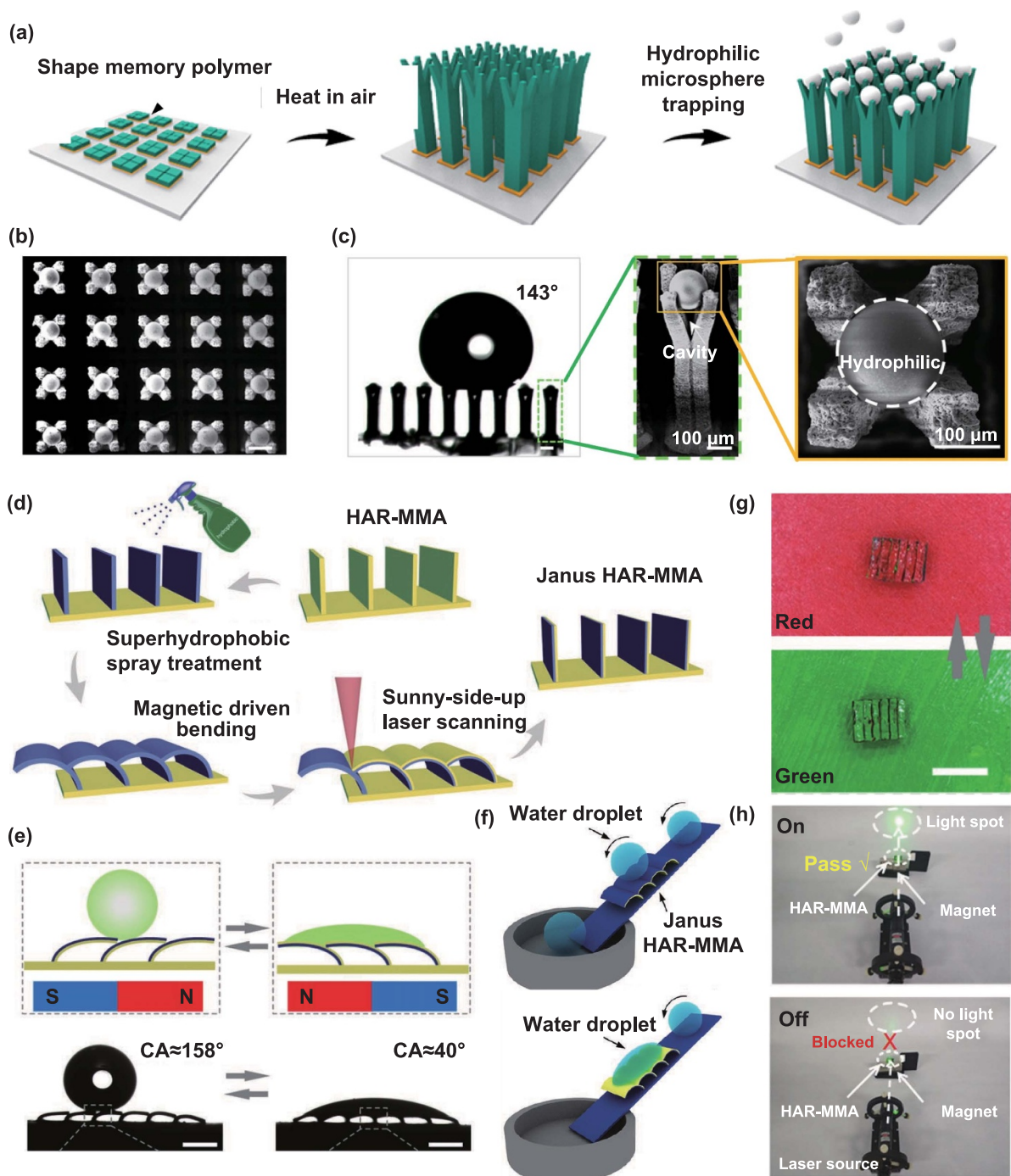


**Figure 28.** Air retention under water and smart wettability on MAAMs-SW. (a) Schematic diagram of the fabrication process of the Salvinia-inspired structures. (b) SEM image of Salvinia-inspired structures (scale bar: 200 μm). (c) Contact angle of the Salvinia-inspired structures and SEM images of a single *Salvinia*-inspired structure. (a)–(c) Reprinted with permission from [96]. Copyright (2022) American Chemical Society. (d) Schematic diagram of the fabrication process of a Janus HAR-MMA. (e) Schematic diagram and optical images of switchable wettability on the Janus HAR-MMA. (f) Schematic diagrams of the selective downward rolling or interception of water droplets on the Janus HAR-MMA. (g) Photographs of the dynamic color conversion between red and green of the Janus HAR-MMA (scale bar: 5 mm). (h) Photographs of optical shutters with light passing through and light blocked. (d)–(h) [97] John Wiley & Sons. © 2019 WILEY-VCH Verlag GmbH & Co. KGaA, Weinheim.

surfaces will inevitably come into direct contact with the surrounding environment, which produces mechanical wear, resulting in poor durability of the superhydrophobic properties [285–287]. Hence, Wang *et al* [98] designed and fabricated an

armored superhydrophobic surface combining macro/microstructures (size: 10–480 μm) with nanostructures. The macro/microstructures consisted of an interconnected frame, which acted as ‘armor’ to resist abrasion, while the nanostructures



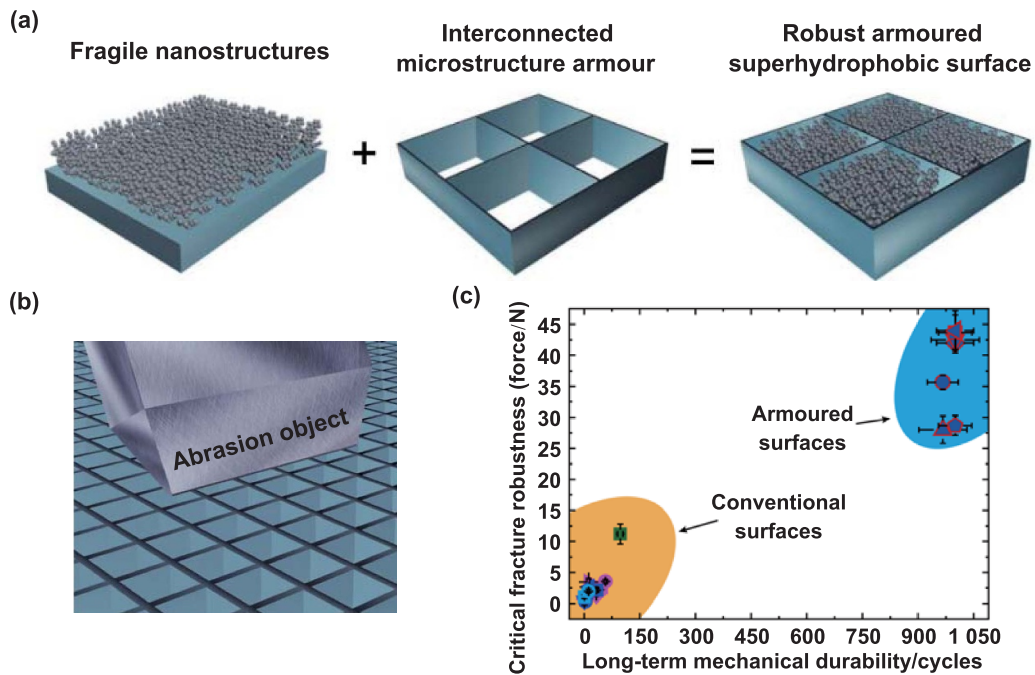


**Figure 29.** Mechanical stability of MAAMs-SW. (a) and (b) Schematic diagrams of the strategy for protecting water-repellent nanostructures using macro/microstructures as armor. (c) Comparison of the mechanical stability of various superhydrophobic surfaces. Reproduced from [98], with permission from Springer Nature.

provided water repellency (figures 29(a) and (b)). Through a comparison of the mechanical stabilities among different superhydrophobic surfaces, the armored superhydrophobic surface could withstand over 1000 wear cycles, which was 10 times more cycles than conventional superhydrophobic surfaces (figure 29(c)).

Despite the promising application prospects of bio-inspired MAAMs-SW, most of these studies remain in the laboratory stage, and further research is needed to implement these technologies to daily life. Current research and development efforts toward the application of bio-inspired MAAMs-SW are making notable progress. A summary and comparison of the various applications are listed in table 3. The applications of bio-inspired MAAMs-SW are evolving in diverse and intelligent directions. It is believed that bio-inspired MAAMs-SW will likely play significant roles in aviation, navigation, energy, environmental, and biomedical fields.

## 6. Summary and outlook

Bio-inspired MAAMs-SW represent an important and growing domain in materials science and engineering. In the present review, we summarized recent progress in the theory, design, fabrication, and application of bio-inspired MAAMs-SW. By studying the fundamental theory of special wettability and drawing inspiration from representative structures in nature, many bio-inspired MAAMs-SW have been fabricated using additive manufacturing, subtractive manufacturing, and formative manufacturing. These materials may be suitable for various applications such as oil repellency, liquid/droplet manipulation, anti-icing, heat transfer, water collection, oil–water separation, drag reduction, air retention

under water, smart wettability, and mechanical stability. However, despite the research progress made for bio-inspired MAAMs-SW over the past two decades, many challenges remain that need to be addressed.

- Researchers have mainly obtained desired bio-inspired MAAMs-SW using simple designs and assisted by processing methods to regulate the morphology of MAAs. However, while many high-performance bio-inspired MAAMs-SW have been fabricated, achieving the design of ideal geometric shapes with superior performance using systematic, scientific, and reasonable methods remains a challenge.
- Many fabrication methods still face problems with large-scale production (such as controllability, uniformity, cost, and efficiency). Therefore, mass-production technologies for the fabrication of MAAMs-SW are needed. Furthermore, due to the high geometric complexity of biological structures in nature, more advanced technologies or clever hybrid technologies must be developed to address the challenges posed by the design and manufacturing of biomimetic structures.
- The design and fabrication of stable and durable MAAMs-SW remains a substantial challenge. Functional MAAs are prone to damage when faced with significant wear, pressing, bending, or other effects. The emergence of armored structures provides a promising solution to this problem. However, the use of armored structures while maintaining original functionality, such as droplet manipulation, anti-icing, oil–water separation, and smart wettability, remains extremely challenging in functionalized design and fabrication.



**Table 3.** Summary of typical bio-inspired MAAMs-SW applied to various applications.

| Applications                | Wetting features   | Characteristics of MAAs  | Fabrication method of MAAs  | Advantages   | Challenges   | References                            |
|-----------------------------|--|--|---|--|--|---------------------------------------|
| Liquid/droplet manipulation | <ul style="list-style-type: none"> <li>• Superhydrophobicity</li> <li>• Anisotropic wettability</li> <li>• Slippery</li> <li>• Structure-induced self-driving of droplets/liquids</li> </ul>                           | <ul style="list-style-type: none"> <li>• Ratchet arrays</li> <li>• Plate arrays</li> <li>• Pillar arrays</li> <li>• Groove arrays</li> <li>• Peristome-inspired cavity arrays</li> <li>• Pine needle-inspired asymmetric arrays</li> <li>• <i>Araucaria</i> leaf-inspired parallel ratchet arrays</li> </ul> | <ul style="list-style-type: none"> <li>• Femtosecond laser ablation</li> <li>• Template method</li> <li>• 3D-printing</li> <li>• Wire electrical discharge machining</li> </ul>                 | <ul style="list-style-type: none"> <li>• Simple operation</li> <li>• Low energy consumption</li> <li>• High efficiency</li> </ul>  | <ul style="list-style-type: none"> <li>• Long-term stability</li> <li>• Integration and portability of manipulation platform</li> <li>• Programmable manipulation of multiple droplets</li> <li>• Manipulation of extremely small or large droplets</li> </ul> | [70, 71, 99, 100, 133, 228, 230, 235] |
| Water collection            | <ul style="list-style-type: none"> <li>• Superhydrophobic–hydrophilic patterns</li> <li>• Superhydrophilicity</li> <li>• Slippery</li> <li>• Structure- and surface energy-induced self-driving of droplets</li> </ul> | <ul style="list-style-type: none"> <li>• Beetle-inspired pillar arrays</li> <li>• Dual-asymmetric channel arrays</li> <li>• Spider silk-inspired spindle-knot/joint structure</li> <li>• Cactus-inspired spine arrays</li> <li>• Tree arrays</li> <li>• Groove arrays</li> </ul>                             | <ul style="list-style-type: none"> <li>• 3D-printing</li> <li>• Template method</li> <li>• Imprinting method</li> <li>• Wire electrical discharge machining</li> <li>• Laser etching</li> </ul> | <ul style="list-style-type: none"> <li>• High efficiency</li> <li>• Low economic cost</li> <li>• Environmental friendliness</li> <li>• Low energy consumption</li> </ul> | <ul style="list-style-type: none"> <li>• Improving the service life</li> <li>• Large-scale fabrication</li> <li>• Use in extreme environments (low humidity, low temperature, strong wind containing sand)</li> </ul>  | [90, 91, 114, 241, 245]               |
| Oil–water separation        | <ul style="list-style-type: none"> <li>• Superhydrophobicity and oleophilicity</li> <li>• Structure-induced self-driving of droplets</li> </ul>  | <ul style="list-style-type: none"> <li>• <i>Salvinia</i>-inspired eggbeater structure arrays</li> <li>• Cactus-inspired spine arrays</li> <li>• Hole arrays</li> <li>• Groove arrays</li> </ul>  | <ul style="list-style-type: none"> <li>• 3D-printing</li> <li>• Template method</li> <li>• Wire electrical discharge machining</li> <li>• Laser etching</li> </ul>                              | <ul style="list-style-type: none"> <li>• Highly efficient, high flux and high selectivity</li> <li>• Easily processed</li> </ul>   | <ul style="list-style-type: none"> <li>• Separation of miscible organic liquids, such as water and ethanol</li> <li>• Multiphase separation</li> </ul>   | [77, 92, 151, 253, 254]               |
| Drag reduction              | <ul style="list-style-type: none"> <li>• Superhydrophobic–hydrophilic patterns</li> <li>• Superhydrophobicity</li> <li>• Slippery</li> </ul>   | <ul style="list-style-type: none"> <li>• <i>Salvinia</i>-inspired eggbeater structure arrays</li> <li>• Sector-like scale arrays</li> </ul>  | <ul style="list-style-type: none"> <li>• Template method assisted with capillary-force-induced clustering</li> <li>• Laser etching</li> </ul>   | <ul style="list-style-type: none"> <li>• Better drag reduction effect and economy</li> <li>• Simultaneously anti-fouling</li> </ul>                                      | <ul style="list-style-type: none"> <li>• Long-term stability in liquid flow environments</li> <li>• Large-scale fabrication</li> </ul>   | [259–261]                             |
| Anti-icing                  | <ul style="list-style-type: none"> <li>• Superhydrophobicity</li> <li>• Structure-induced condensation droplets arranged in gradient according to size</li> </ul>  | <ul style="list-style-type: none"> <li>• Ratchet arrays</li> <li>• Ridge arrays</li> <li>• Pillar arrays</li> </ul>  | <ul style="list-style-type: none"> <li>• Micro-mechanical cutting machining</li> <li>• Wire electrical discharge machining</li> <li>• Laser etching</li> </ul>                                  | <ul style="list-style-type: none"> <li>• Significant delay in freezing</li> </ul>  | <ul style="list-style-type: none"> <li>• Improving mechanical and pressure stability</li> <li>• Large-scale fabrication</li> </ul>   | [87, 88, 266]                         |

(Continued.)

**Table 3.** (Continued.)

| Applications              | Wetting features  | Characteristics of MAAs   | Fabrication method of MAAs  | Advantages   | Challenges  | References         |
|---------------------------|---|---|---|--|---|--------------------|
| Heat transfer             | <ul style="list-style-type: none"> <li>• Superhydrophobic–hydrophilic patterns</li> <li>• Superhydrophobicity</li> <li>• Superhydrophilicity</li> </ul>               | <ul style="list-style-type: none"> <li>• Pillar arrays</li> <li>• Groove arrays</li> <li>• Multiple grooves and pores</li> </ul>          | <ul style="list-style-type: none"> <li>• Micro-mechanical cutting machining</li> <li>• Wire electrical discharge machining</li> <li>• Laser etching</li> </ul>  | <ul style="list-style-type: none"> <li>• Self-propelled effect</li> <li>• Highly efficient</li> <li>• Prevents nucleate-boiling phase</li> </ul> | <ul style="list-style-type: none"> <li>• Improving mechanical robustness</li> <li>• Achieving high-temperature tolerance</li> </ul> | [89, 269–274]      |
| Oil repellency            | <ul style="list-style-type: none"> <li>• Superoleophobicity</li> </ul>  | <ul style="list-style-type: none"> <li>• Re-entrant structure arrays</li> <li>• Hierarchical structures</li> </ul>                        | <ul style="list-style-type: none"> <li>• 3D-printing</li> <li>• Laser-induced self-growing method</li> <li>• Laser ablation and electro-chemical deposition</li> <li>• Wire electrical discharge machining</li> </ul> | <ul style="list-style-type: none"> <li>• Simple fabrication method</li> <li>• Suitable for large-scale fabrication</li> </ul>                    | <ul style="list-style-type: none"> <li>• Lower performance and poorer stability than micro/nano re-entrant structures</li> </ul>    | [79, 80, 183, 276] |
| Air retention under water | <ul style="list-style-type: none"> <li>• Superhydrophobic–hydrophilic patterns</li> <li>• Superhydrophobicity</li> </ul>  | <ul style="list-style-type: none"> <li>• Salvinia-inspired eggbeater structure arrays</li> <li>• Four-branch hollow structures</li> </ul> | <ul style="list-style-type: none"> <li>• 3D-printing</li> <li>• Top-constrained self-branching method</li> <li>• Imprinting method</li> </ul>   | <ul style="list-style-type: none"> <li>• Simple operation</li> <li>• High efficiency</li> </ul>  | <ul style="list-style-type: none"> <li>• Long-term stability</li> <li>• Stability in complex environments</li> </ul>                | [67, 96, 277, 278] |
| Smart wettability         | <ul style="list-style-type: none"> <li>• Superhydrophobic/hydrophilic properties</li> <li>• High/low adhesion</li> <li>• Anisotropic/isotropic wettability</li> </ul> | <ul style="list-style-type: none"> <li>• Groove arrays</li> <li>• Plate arrays</li> </ul>   | <ul style="list-style-type: none"> <li>• Template method</li> <li>• Laser etching</li> </ul>  | <ul style="list-style-type: none"> <li>• Simple and efficient</li> <li>• Easy operation</li> <li>• Good controllability</li> </ul>               | <ul style="list-style-type: none"> <li>• Improving physical and chemical durability</li> </ul>                                      | [97, 279–282]      |
| Mechanical stability      | <ul style="list-style-type: none"> <li>• Superhydrophobicity</li> </ul>   | <ul style="list-style-type: none"> <li>• Armored structures</li> <li>• Pillar arrays (protective structures)</li> </ul>                   | <ul style="list-style-type: none"> <li>• Laser shock/etching</li> <li>• Maskless electrochemical machining</li> <li>• Imprinting method</li> </ul>  | <ul style="list-style-type: none"> <li>• Improved mechanical stability</li> <li>• Easily processed</li> </ul>                                    | <ul style="list-style-type: none"> <li>• Robustness and durability of comprehensive evaluation</li> </ul>                           | [98, 283, 284]     |

• Finally, the industrialization and marketization process of these bio-inspired MAAMs-SW remains hindered. Most reported materials are still in the proof-of-concept stage, in terms of potential applications in relevant fields, with significant research still needed to achieve practical applications. Therefore, the controllability, durability, intelligence, and biosafety of the MAAMs-SW should be improved to convert these materials into commercial products.

Despite many development challenges, bio-inspired MAAMs-SW have promising prospects. To allow MAAMs-SW to transition from laboratory exploration to practical applications, the following research directions should be further explored.

(1) New theories and advanced methods must be explored to explain the complex wetting phenomena. Researchers still use wetting models that were proposed more than 70 or even 200 years ago. However, the classic Young’s equation, Wenzel model, and Cassie–Baxter model analyze wetting phenomena from macro and micro perspectives, making it necessary to develop new hypotheses at extreme scales (molecular or even atomic) to break through barriers in this field. However, although some wetting models have been proposed to explain the static wetting behavior, revealing the dynamic wetting behaviors of droplets on material surfaces remains difficult. In this regard, using advanced methods such as numerical simulations to accurately predict the impacts of structures on

dynamic wettability serves as an indispensable strategy for future research.

- (2) The mechanisms of special wettability in nature require further research for designing bio-inspired MAA materials that can be used in engineering systems. Therefore, advanced characterization and testing techniques must be developed to reveal a deeper understanding of nature. In addition, nature still contains many mysteries that can be explored, which may offer design principles for new MAAMs-SW.
- (3) Bio-inspired MAAMs-SW have shown good functionality, however, fabrication strategies for these materials still need to be improved, as some methods remain limited to basic research in the laboratory and are difficult to industrialize. Simple, efficient, low-cost, and green technologies that can fabricate large-area bio-inspired materials with MAAs using a scalable approach are essential for industrialization. Moreover, many strategies can fabricate complex MAAs with only a limited degree or aspect. Therefore, future studies on the fabrication of bio-inspired MAAMs-SW will likely consist of composite methods (selective combinations of different methods) and multi-dimensional (4D or 5D printing) fabrication.
- (4) Poor physical and chemical durability severely limits the practical application of bio-inspired MAAMs-SW. Many surfaces tend to lose their functionality with repeated use or exposure to harsh environments. Although some stable bio-inspired MAAMs-SW have been developed by regulating the surface chemistry or designing the surface morphology, there is an unmet need to obtain more durable MAAs. Many technologies, such as 3D printing, lasers, and WEDM, will cause substantial thermal damage to materials during the fabrication process, and in complex environments, such as friction and wear, tensile stress, and corrosion environments, this damage will be amplified, seriously affecting the durability of these materials. Therefore, more advanced or optimized technology must be proposed to fabricate bio-inspired MAAMs-SW. In addition, intelligent reparability is a highly desirable characteristic for MAAs, but will be very difficult to achieve.
- (5) Regarding functional applications, most current work has focused on the fabrication of MAAs with a single function, which cannot meet the demands of many practical applications. Bio-inspired materials with multifunction integration have attracted considerable attention. For example, integrating anti-icing performance into materials with water collection or drag reduction functions can achieve the functional requirements of these materials in low-temperature environments. Manipulating the behavior of small droplets through external fields can significantly improve the performance of materials during the process of water collection or oil–water separation. Therefore, developing bio-inspired MAA materials with multiple functions serves as an inevitable trend for the future.

Overall, bio-inspired MAAMs-SW stand as promising and advanced materials to address the growing global energy

and environmental crises. These materials can be obtained by understanding natural structures and replicating them in engineering applications using various technologies. The ongoing pursuit of continuous exploration of the theory, design, fabrication, and collaboration of various disciplines, ever-increasing, novel, bio-inspired MAAMs-SW will likely emerge. We hope that this review can provide guidance for promoting the development of bio-inspired MAAMs-SW.

## Acknowledgments


This work was supported by the National Defense Basic Scientific Research Project (No. JCKY2020210B001), the National Natural Science Foundation of China (No. U19A20103), the China Postdoctoral Science Foundation (No. 2019M661184), the Jilin Province Scientific and Technological Development Program (No. YDZJ202101ZYTS025), the Jilin Province Young Science and Technology Talent Lift Project (No. QT202030), and the Science and Technology Innovation Fund of CUST (No. XJLJG-2019-05).

## ORCID iDs

Zhongxu Lian  <https://orcid.org/0000-0003-0675-7947>

Faze Chen  <https://orcid.org/0000-0003-2282-4548>

Jinkai Xu  <https://orcid.org/0000-0002-5373-4564>

Huadong Yu  <https://orcid.org/0000-0003-0756-512X>

## References

- [1] Tonna S, El-Osta A, Cooper M E and Tikellis C 2010 Metabolic memory and diabetic nephropathy: potential role for epigenetic mechanisms *Nat. Rev. Nephrol.* **6** 332–41
- [2] Benga G, Porutiu D, Ghiran I, Kuchel P W, Gallagher C H and Cox G C 1992 Scanning electron microscopy of red blood cells from eleven species of marsupial *Comp. Haematol. Int.* **2** 227–30
- [3] Chu F, Anex D S, Jones A D and Hart B R 2020 Automated analysis of scanning electron microscopic images for assessment of hair surface damage *R. Soc. Open Sci.* **7** 191438
- [4] Rajakumar R, Koch S, Couture M, Favé M J, Lilloco-Ouachour A, Chen T, De Blasis G, Rajakumar A, Ouellette D and Abouheif E 2018 Social regulation of a rudimentary organ generates complex worker-caste systems in ants *Nature* **562** 574–7
- [5] Khoshnevisan K, Maleki H and Baharifar H 2021 Nanobiocide based-silver nanomaterials upon coronaviruses: approaches for preventing viral infections *Nanoscale Res. Lett.* **16** 100
- [6] Chen Y *et al* 2021 Achieving a sub-10 nm nanopore array in silicon by metal-assisted chemical etching and machine learning *Int. J. Extrem. Manuf.* **3** 035104
- [7] Kawata S, Sun H B, Tanaka T and Takada K 2001 Finer features for functional microdevices *Nature* **412** 697–8
- [8] Ren W F, Xu J K, Lian Z X, Sun X Q, Xu Z M and Yu H D 2022 Localized electrodeposition micro additive manufacturing of pure copper microstructures *Int. J. Extrem. Manuf.* **4** 015101



- [9] Scotho A, Förster R and Menz W 2005 Micro wire EDM for high aspect ratio 3D microstructuring of ceramics and metals *Microsyst. Technol.* **11** 250–3
- [10] Liu M J, Wang S T and Jiang L 2017 Nature-inspired superwettability systems *Nat. Rev. Mater.* **2** 17036
- [11] Zhang C Q, Macdams I I D A and Grunlan J C 2016 Nano/micro-manufacturing of bioinspired materials: a review of methods to mimic natural structures *Adv. Mater.* **28** 6292–321
- [12] Si Y F, Dong Z C and Jiang L 2018 Bioinspired designs of superhydrophobic and superhydrophilic materials *ACS Cent. Sci.* **4** 1102–12
- [13] Han Z W, Mu Z Z, Yin W, Li W, Niu S C, Zhang J Q and Ren L Q 2016 Biomimetic multifunctional surfaces inspired from animals *Adv. Colloid Interface Sci.* **234** 27–50
- [14] Ueda E and Levkin P A 2013 Emerging applications of superhydrophilic-superhydrophobic micropatterns *Adv. Mater.* **25** 1234–47
- [15] Barthlott W, Mail M, Bhushan B and Koch K 2017 Plant surfaces: structures and functions for biomimetic innovations *Nano-Micro Lett.* **9** 23
- [16] Xu J K, Xiu S Y, Lian Z X, Yu H D and Cao J J 2022 Bioinspired materials for droplet manipulation: principles, methods and applications *Droplet* **1** 11–37
- [17] Barthlott W and Neinhuis C 1997 Purity of the sacred lotus, or escape from contamination in biological surfaces *Planta* **202** 1–8
- [18] Feng L, Li S, Li Y, Li H, Zhang L, Zhai J, Song Y, Liu B, Jiang L and Zhu D 2002 Super-hydrophobic surfaces: from natural to artificial *Adv. Mater.* **14** 1857–60
- [19] Wisdom K M, Watson J A, Qu X P, Liu F J, Watson G S and Chen C H 2013 Self-cleaning of superhydrophobic surfaces by self-propelled jumping condensate *Proc. Natl Acad. Sci. USA* **110** 7992–7
- [20] Gao X, Yan X, Yao X, Xu L, Zhang K, Zhang J, Yang B and Jiang L 2007 The dry-style antifogging properties of mosquito compound eyes and artificial analogues prepared by soft lithography *Adv. Mater.* **19** 2213–7
- [21] Zheng Y M, Gao X F and Jiang L 2007 Directional adhesion of superhydrophobic butterfly wings *Soft Matter* **3** 178–82
- [22] Niu S C, Li B, Mu Z Z, Yang M, Zhang J Q, Han Z W and Ren L Q 2015 Excellent structure-based multifunction of *Morpho* butterfly wings: a review *J. Bionic Eng.* **12** 170–89
- [23] Gao X F and Jiang L 2004 Water-repellent legs of water striders *Nature* **432** 36
- [24] Wang Q B, Yao X, Liu H, Quéré D and Jiang L 2015 Self-removal of condensed water on the legs of water striders *Proc. Natl Acad. Sci. USA* **112** 9247–52
- [25] Liu M J, Wang S T, Wei Z X, Song Y L and Jiang L 2009 Bioinspired design of a superoleophobic and low adhesive water/solid interface *Adv. Mater.* **21** 665–9
- [26] Bixler G D and Bhushan B 2012 Bioinspired rice leaf and butterfly wing surface structures combining shark skin and lotus effects *Soft Matter* **8** 11271–84
- [27] Feng L, Zhang Y A, Xi J M, Zhu Y, Wang N, Xia F and Jiang L 2008 Petal effect: a superhydrophobic state with high adhesive force *Langmuir* **24** 4114–9
- [28] Jin H Y, Li Y F, Zhang P, Nie S C and Gao N K 2016 The investigation of the wetting behavior on the red rose petal *Appl. Phys. Lett.* **108** 151605
- [29] Liu K S, Du J X, Wu J T and Jiang L 2012 Superhydrophobic gecko feet with high adhesive forces towards water and their bio-inspired materials *Nanoscale* **4** 768–72
- [30] Murphy M P, Aksak B and Sitti M 2009 Gecko-inspired directional and controllable adhesion *Small* **5** 170–5
- [31] Vorobyev A Y and Guo C L 2013 Direct femtosecond laser surface nano/microstructuring and its applications *Laser Photon. Rev.* **7** 385–407
- [32] Zhang Y, Y, Jiao Y L, Li C Z, Chen C, Li J W, Hu Y L, Wu D and Chu J R 2020 Bioinspired micro/nanostructured surfaces prepared by femtosecond laser direct writing for multi-functional applications *Int. J. Extrem. Manuf.* **2** 032002
- [33] Darmanin T, de Givenchy E T, Amigoni S and Guittard F 2013 Superhydrophobic surfaces by electrochemical processes *Adv. Mater.* **25** 1378–94
- [34] Xia D Y, Johnson L M and López G P 2012 Anisotropic wetting surfaces with one-dimensional and directional structures: fabrication approaches, wetting properties and potential applications *Adv. Mater.* **24** 1287–302
- [35] Wang X F, Ding B, Yu J Y and Wang M R 2011 Engineering biomimetic superhydrophobic surfaces of electrospun nanomaterials *Nano Today* **6** 510–30
- [36] Yang Y, Song X, Li X J, Chen Z Y, Zhou C, Zhou Q F and Chen Y 2018 Recent progress in biomimetic additive manufacturing technology: from materials to functional structures *Adv. Mater.* **30** 1706539
- [37] Wang S T, Liu K S, Yao X and Jiang L 2015 Bioinspired surfaces with superwettability: new insight on theory, design, and applications *Chem. Rev.* **115** 8230–93
- [38] Dong Z Q and Levkin P A 2023 3D microprinting of super-repellent microstructures: recent developments, challenges, and opportunities *Adv. Funct. Mater.* **33** 2213916
- [39] Zhou H, Niu H T, Wang H X and Lin T 2023 Self-healing superwetting surfaces, their fabrications, and properties *Chem. Rev.* **123** 663–700
- [40] Su B, Tian Y and Jiang L 2016 Bioinspired interfaces with superwettability: from materials to chemistry *J. Am. Chem. Soc.* **138** 1727–48
- [41] Wen L P, Tian Y and Jiang L 2015 Bioinspired super-wettability from fundamental research to practical applications *Angew. Chem., Int. Ed.* **54** 3387–99
- [42] Yao L and He J H 2014 Recent progress in antireflection and self-cleaning technology—from surface engineering to functional surfaces *Prog. Mater. Sci.* **61** 94–143
- [43] Han Z W, Jiao Z B, Niu S C and Ren L Q 2019 Ascendant bioinspired antireflective materials: opportunities and challenges coexist *Prog. Mater. Sci.* **103** 1–68
- [44] Durán I R and Laroche G 2019 Current trends, challenges, and perspectives of anti-fogging technology: surface and material design, fabrication strategies, and beyond *Prog. Mater. Sci.* **99** 106–86
- [45] Han Z W, Feng X M, Guo Z G, Niu S C and Ren L Q 2018 Flourishing bioinspired antifogging materials with superwettability: progresses and challenges *Adv. Mater.* **30** 1704652
- [46] Dhyani A, Choi W, Golovin K and Tuteja A 2022 Surface design strategies for mitigating ice and snow accretion *Matter* **5** 1423–54
- [47] Zhang Z S and Liu X Y 2018 Control of ice nucleation: freezing and antifreeze strategies *Chem. Soc. Rev.* **47** 7116–39
- [48] Kreder M J, Alvarenga J, Kim P and Aizenberg J 2016 Design of anti-icing surfaces: smooth, textured or slippery? *Nat. Rev. Mater.* **1** 15003
- [49] Wang L Z, Tian Z, Jiang G C, Luo X, Chen C H, Hu X Y, Zhang H J and Zhong M L 2022 Spontaneous dewetting transitions of droplets during icing & melting cycle *Nat. Commun.* **13** 378
- [50] Gong X J, Gao X F and Jiang L 2017 Recent progress in bionic condensate microdrop self-propelling surfaces *Adv. Mater.* **29** 1703002

- [51] Liang X C, Kumar V, Ahmadi F and Zhu Y Y 2022 Manipulation of droplets and bubbles for thermal applications *Droplet* **1** 80–91
- [52] Dai H Y, Dong Z C and Jiang L 2020 Directional liquid dynamics of interfaces with superwettability *Sci. Adv.* **6** eabb5528
- [53] Leng X, Sun L C, Long Y J and Lu Y 2022 Bioinspired superwetting materials for water manipulation *Droplet* **1** 139–69
- [54] Li Y, He L L, Zhang X F, Zhang N and Tian D L 2017 External-field-induced gradient wetting for controllable liquid transport: from movement on the surface to penetration into the surface *Adv. Mater.* **29** 1703802
- [55] Yu C M, Zhang P P, Wang J M and Jiang L 2017 Superwettability of gas bubbles and its application: from bioinspiration to advanced materials *Adv. Mater.* **29** 1703053
- [56] Jin H C, Tian L M, Bing W, Zhao J and Ren L Q 2022 Bioinspired marine antifouling coatings: status, prospects, and future *Prog. Mater. Sci.* **124** 100889
- [57] Lishchynskyi O, Shymborska Y, Stetsyshyn Y, Raczkowska J, Skirtach A G, Peretiatio T and Budkowski A 2022 Passive antifouling and active self-disinfecting antiviral surfaces *Chem. Eng. J.* **446** 137048
- [58] Bhushan B and Jung Y C 2011 Natural and biomimetic artificial surfaces for superhydrophobicity, self-cleaning, low adhesion, and drag reduction *Prog. Mater. Sci.* **56** 1–108
- [59] Wang B, Liang W X, Guo Z G and Liu W M 2015 Biomimetic super-lyophobic and super-lyophilic materials applied for oil/water separation: a new strategy beyond nature *Chem. Soc. Rev.* **44** 336–61
- [60] Chu Z L, Feng Y J and Seeger S 2015 Oil/water separation with selective superant/wetting/superwetting surface materials *Angew. Chem., Int. Ed.* **54** 2328–38
- [61] Yu Z H, Zhu T X, Zhang J C, Ge M Z, Fu S H and Lai Y K 2022 Fog harvesting devices inspired from single to multiple creatures: current progress and future perspective *Adv. Funct. Mater.* **32** 2200359
- [62] Wang B, C X, Guo Z G and Liu W M 2021 Recent advances in atmosphere water harvesting: design principle, materials, devices, and applications *Nano Today* **40** 101283
- [63] Yue H, Zeng Q H, Huang J X, Guo Z G and Liu W M 2022 Fog collection behavior of bionic surface and large fog collector: a review *Adv. Colloid Interface Sci.* **300** 102583
- [64] Falde E J, Yohe S T, Colson Y L and Grinstaff M W 2016 Superhydrophobic materials for biomedical applications *Biomaterials* **104** 87–103
- [65] Chi J J, Zhang X X, Wang Y T, Shao C M, Shang L R and Zhao Y J 2021 Bio-inspired wettability patterns for biomedical applications *Mater. Horiz.* **8** 124–44
- [66] Jokinen V, Kankuri E, Hoshian S, Franssila S and Ras R H A 2018 Superhydrophobic blood-repellent surfaces *Adv. Mater.* **30** 1705104
- [67] Barthlott W *et al* 2010 The Salvinia paradox: superhydrophobic surfaces with hydrophilic pins for air retention under water *Adv. Mater.* **22** 2325–8
- [68] Parker A R and Lawrence C R 2001 Water capture by a desert beetle *Nature* **414** 33–34
- [69] Ju J, Bai H, Zheng Y M, Zhao T Y, Fang R C and Jiang L 2012 A multi-structural and multi-functional integrated fog collection system in cactus *Nat. Commun.* **3** 1247
- [70] Feng S L, Delannoy J, Malod A, Zheng H X, Quéré D and Wang Z K 2020 Tip-induced flipping of droplets on Janus pillars: from local reconfiguration to global transport *Sci. Adv.* **6** eabb4540
- [71] Feng S L, Zhu P A, Zheng H X, Zhan H Y, Chen C, Li J Q, Wang L Q, Yao X, Liu Y H and Wang Z K 2021 Three-dimensional capillary ratchet-induced liquid directional steering *Science* **373** 1344–8
- [72] Helbig R, Nickerl J, Neinhuis C and Werner C 2011 Smart skin patterns protect springtails *PLoS One* **6** e25105
- [73] Zheng Y M, Bai H, Huang Z B, Tian X L, Nie F Q, Zhao Y, Zhai J and Jiang L 2010 Directional water collection on wetted spider silk *Nature* **463** 640–3
- [74] Chen H W, Zhang P F, Zhang L W, Liu H L, Jiang Y, Zhang D Y, Han Z W and Jiang L 2016 Continuous directional water transport on the peristome surface of *Nepenthes alata* *Nature* **532** 85–89
- [75] Goodwyn P, P, Maezono Y, Hosoda N and Fujisaki K 2009 Waterproof and translucent wings at the same time: problems and solutions in butterflies *Naturwissenschaften* **96** 781–7
- [76] Wu D, Wang J N, Wu S Z, Chen Q D, Zhao S, Zhang H, Sun H B and Jiang L 2011 Three-level biomimetic rice-leaf surfaces with controllable anisotropic sliding *Adv. Funct. Mater.* **21** 2927–32
- [77] Yang Y, Li X J, Zheng X, Chen Z Y, Zhou Q F and Chen Y 2018 3D-printed biomimetic super-hydrophobic structure for microdroplet manipulation and oil/water separation *Adv. Mater.* **30** 1704912
- [78] Cao M Y, Ju J, Li K, Dou S X, Liu K S and Jiang L 2014 Facile and large-scale fabrication of a cactus-inspired continuous fog collector *Adv. Funct. Mater.* **24** 3235–40
- [79] Yang Y *et al* 2021 Femtosecond laser regulated ultrafast growth of mushroom-like architecture for oil repellency and manipulation *Nano Lett.* **21** 9301–9
- [80] Song J L, Pan W H, Wang K, Chen F Z and Sun Y W 2020 Fabrication of micro-reentrant structures by liquid/gas interface shape-regulated electrochemical deposition *Int. J. Mach. Tools Manuf.* **159** 103637
- [81] Li J Q, Zhou X F, Li J, Che L F, Yao J, McHale G, Chaudhury M K and Wang Z K 2017 Topological liquid diode *Sci. Adv.* **3** eaao3530
- [82] Feng S L, Wang Q Q, Xing Y, Hou Y P and Zheng Y M 2020 Continuous directional water transport on integrating tapered surfaces *Adv. Mater. Interfaces* **7** 2000081
- [83] Lee M, Oh J, Lim H and Lee J 2021 Enhanced liquid transport on a highly scalable, cost-effective, and flexible 3D topological liquid capillary diode *Adv. Funct. Mater.* **31** 2011288
- [84] Li X, Li J Q and Dong G N 2020 Bioinspired topological surface for directional oil lubrication *ACS Appl. Mater. Interfaces* **12** 5113–9
- [85] Weisensee P B, Torrealba E J, Raleigh M, Jacobi A M and King W P 2014 Hydrophobic and oleophobic re-entrant steel microstructures fabricated using micro electrical discharge machining *J. Micromech. Microeng.* **24** 095020
- [86] Cai Z X, Chen F Z, Tian Y L, Zhang D W, Lian Z X and Cao M Y 2022 Programmable droplet transport on multi-bioinspired slippery surface with tridirectionally anisotropic wettability *Chem. Eng. J.* **449** 137831
- [87] Guo P, Zheng Y M, Wen M X, Song C, Lin Y C and Jiang L 2012 Icephobic/anti-icing properties of micro/nanostructured surfaces *Adv. Mater.* **24** 2642–8
- [88] Pan W H, Wu S, Huang L and Song J L 2021 Large-area fabrication of superhydrophobic micro-conical pillar arrays on various metallic substrates *Nanoscale* **13** 14023–34
- [89] Cheng Y Q, Liu Y B, Ye X, Liu M J, Du B G, Jin Y K, Wen R F, Lan Z, Wang Z K and Ma X H 2021 Macrotextures-enabled self-propelling of large condensate droplets *Chem. Eng. J.* **405** 126901
- [90] Park K C, Kim P, Grinthal A, He N, Fox D, Weaver J C and Aizenberg J 2016 Condensation on slippery asymmetric bumps *Nature* **531** 78–82

- [91] Tian Y, Zhu P G, Tang X, Zhou C M, Wang J M, Kong T T, Xu M and Wang L Q 2017 Large-scale water collection of bioinspired cavity-microfibers *Nat. Commun.* **8** 1080
- [92] Li K, Ju J, Xue Z X, Ma J, Feng L, Gao S and Jiang L 2013 Structured cone arrays for continuous and effective collection of micron-sized oil droplets from water *Nat. Commun.* **4** 2276
- [93] Li Y X *et al* 2022 Directional and adaptive oil self-transport on a multi-bioinspired grooved conical spine *Adv. Funct. Mater.* **32** 2201035
- [94] Tuo Y J, Zhang H F, Rong W T, Jiang S Y, Chen W P and Liu X W 2019 Drag reduction of anisotropic superhydrophobic surfaces prepared by laser etching *Langmuir* **35** 11016–22
- [95] Yoo K J, Moon I Y, Lee H W, Oh Y S, Kim S J, Moon Y H and Kang S H 2021 Evaluation of air layer behavior on patterned PTFE surfaces under underwater environment conditions *J. Mech. Sci. Technol.* **35** 679–87
- [96] Zhang Y C *et al* 2022 Robust underwater air layer retention and restoration on *Salvinia*-inspired self-grown heterogeneous architectures *ACS Nano* **16** 2730–40
- [97] Jiang S J *et al* 2019 Multifunctional Janus microplates arrays actuated by magnetic fields for water/light switches and bio-inspired assimilatory coloration *Adv. Mater.* **31** 1807507
- [98] Wang D H *et al* 2020 Design of robust superhydrophobic surfaces *Nature* **582** 55–59
- [99] Liu Y H, Moevius L, Xu X P, Qian T Z, Yeomans J M and Wang Z K 2014 Pancake bouncing on superhydrophobic surfaces *Nat. Phys.* **10** 515–9
- [100] Song M R, Liu Z H, Ma Y J, Dong Z C, Wang Y L and Jiang L 2017 Reducing the contact time using macro anisotropic superhydrophobic surfaces—effect of parallel wire spacing on the drop impact *NPG Asia Mater.* **9** e415
- [101] Young T 1805 An essay on the cohesion of fluids *Proc. Trans. R. Soc.* **95** 65–87
- [102] Kota A K, Kwon G and Tuteja A 2014 The design and applications of superomniphobic surfaces *NPG Asia Mater.* **6** e109
- [103] Yong J L, Chen F, Yang Q, Huo J L and Hou X 2017 Superoleophobic surfaces *Chem. Soc. Rev.* **46** 4168–217
- [104] Wenzel R N 1936 Resistance of solid surfaces to wetting by water *Ind. Eng. Chem.* **28** 988–94
- [105] Cassie A B D and Baxter S 1944 Wettability of porous surfaces *Trans. Faraday Soc.* **40** 546–51
- [106] Wong T S, Kang S H, Tang S K Y, Smythe E J, Hatton B D, Grinthal A and Aizenberg J 2011 Bioinspired self-repairing slippery surfaces with pressure-stable omniphobicity *Nature* **477** 443–7
- [107] Tuteja A, Choi W, Ma M L, Mabry J M, Mazzella S A, Rutledge G C, McKinley G H and Cohen R E 2007 Designing superoleophobic surfaces *Science* **318** 1618–22
- [108] Tuteja A, Choi W, Mabry J M, McKinley G H and Cohen R E 2008 Robust omniphobic surfaces *Proc. Natl Acad. Sci. USA* **105** 18200–5
- [109] Ju J, Zheng Y M and Jiang L 2014 Bioinspired one-dimensional materials for directional liquid transport *Acc. Chem. Res.* **47** 2342–52
- [110] Zhu H, Huang Y, Lou X and Xia F 2019 Beetle-inspired wettable materials: from fabrications to applications *Mater. Today Nano* **6** 100034
- [111] Guo J, Huang W, Guo Z G and Liu W M 2022 Design of a venation-like patterned surface with hybrid wettability for highly efficient fog harvesting *Nano Lett.* **22** 3104–11
- [112] Yin K, Du H F, Dong X R, Wang C, Duan J A and He J 2017 A simple way to achieve bioinspired hybrid wettability surface with micro/nanopatterns for efficient fog collection *Nanoscale* **9** 14620–6
- [113] Gam-Derouich S, Pinson J, Lamouri A, Decorse P, Bellync S, Herbaut R, Royon L and Mangeney C 2018 Micro-patterned anti-icing coatings with dual hydrophobic/hydrophilic properties *J. Mater. Chem. A* **6** 19353–7
- [114] Zhou W L, Wu T, Du Y, Zhang X H, Chen X C, Li J B, Xie H and Qu J P 2023 Efficient fabrication of desert beetle-inspired micro/nano-structures on polypropylene/graphene surface with hybrid wettability, chemical tolerance, and passive anti-icing for quantitative fog harvesting *Chem. Eng. J.* **453** 139784
- [115] Li H Y, Mu P, Li J and Wang Q T 2021 Inverse desert beetle-like ZIF-8/PAN composite nanofibrous membrane for highly efficient separation of oil-in-water emulsions *J. Mater. Chem. A* **9** 4167–75
- [116] Tao X L, Chen X Y, Cai S, Yan F, Li S Q, Jin S W and Zhu H 2023 A multifunctional heterogeneous superwetable coating for water collection, oil/water separation and oil absorption *J. Hazard. Mater.* **443** 130166
- [117] Xu Y, Wang G, Zhu L J, Deng W S, Wang C T, Ren T H, Zhu B K and Zeng Z X 2022 Desert beetle-like microstructures bridged by magnetic Fe<sub>3</sub>O<sub>4</sub> grains for enhancing oil-in-water emulsion separation performance and solar-assisted recyclability of graphene oxide *Chem. Eng. J.* **427** 130904
- [118] Liu C C, Xue Y, Chen Y and Zheng Y M 2015 Effective directional self-gathering of drops on spine of cactus with splayed capillary arrays *Sci. Rep.* **5** 17757
- [119] Lorenceau É and Quéré D 2004 Drops on a conical wire *J. Fluid Mech.* **510** 29–45
- [120] Renvoisé P, Bush J W M, Prakash M and Quéré D 2009 Drop propulsion in tapered tubes *Europhys. Lett.* **86** 64003
- [121] Chaudhury M K and Whitesides G M 1992 How to make water run uphill *Science* **256** 1539–41
- [122] Daniel S, Chaudhury M K and Chen J C 2001 Fast drop movements resulting from the phase change on a gradient surface *Science* **291** 633–6
- [123] Nickerl J, Helbig R, Schulz H J, Werner C and Neinhuis C 2013 Diversity and potential correlations to the function of Collembola cuticle structures *Zoomorphology* **132** 183–95
- [124] Hensel R, Helbig R, Aland S, Braun H G, Voigt A, Neinhuis C and Werner C 2013 Wetting resistance at its topographical limit: the benefit of mushroom and serif T structures *Langmuir* **29** 1100–12
- [125] Liu Y, Shao Z Z and Vollrath F 2005 Relationships between supercontraction and mechanical properties of spider silk *Nat. Mater.* **4** 901–5
- [126] Vollrath F 2000 Strength and structure of spiders' silks *Rev. Mol. Biotechnol.* **74** 67–83
- [127] Vollrath F and Edmonds D T 1989 Modulation of the mechanical properties of spider silk by coating with water *Nature* **340** 305–7
- [128] Bai H, Ju J, Sun R Z, Chen Y, Zheng Y M and Jiang L 2011 Controlled fabrication and water collection ability of bioinspired artificial spider silks *Adv. Mater.* **23** 3708–11
- [129] Tian X L, Chen Y, Zheng Y M, Bai H and Jiang L 2011 Controlling water capture of bioinspired fibers with hump structures *Adv. Mater.* **23** 5486–91
- [130] Wang L F, Yang S Y, Wang J, Wang C F and Chen L 2011 Fabrication of superhydrophobic TPU film for oil-water separation based on electrospinning route *Mater. Lett.* **65** 869–72
- [131] Wang Y F, Lai C L, Wang X W, Liu Y, Hu H W, Guo Y J, Ma K K, Fei B and Xin J H 2016 Beads-on-string structured nanofibers for smart and reversible oil/water separation with outstanding antifouling property *ACS Appl. Mater. Interfaces* **8** 25612–20
- [132] Zhang L W, Liu G, Chen H W, Liu X L, Ran T, Zhang Y, Gan Y and Zhang D Y 2021 Bioinspired unidirectional



- liquid transport micro-nano structures: a review *J. Bionic Eng.* **18** 1–29
- [133] Li C X, Li N, Zhang X S, Dong Z C, Chen H W and Jiang L 2016 Uni-directional transportation on peristome-mimetic surfaces for completely wetting liquids *Angew. Chem., Int. Ed.* **55** 14988–92
- [134] Xiao X, Li S K, Zhu X D, Xiao X, Zhang C H, Jiang F M, Yu C M and Jiang L 2021 Bioinspired two-dimensional structure with asymmetric wettability barriers for unidirectional and long-distance gas bubble delivery underwater *Nano Lett.* **21** 2117–23
- [135] Li C X, Yu C L, Zhou S, Dong Z C and Jiang L 2020 Liquid harvesting and transport on multiscaled curvatures *Proc. Natl Acad. Sci. USA* **117** 23436–42
- [136] Zhang S N, Huang J Y, Chen Z and Lai Y K 2017 Bioinspired special wettability surfaces: from fundamental research to water harvesting applications *Small* **13** 1602992
- [137] Li Z M, Zhang D Y, Wang D Y, Zhang L W, Feng L and Zhang X Y 2019 A bioinspired flexible film fabricated by surface-tension-assisted replica molding for dynamic control of unidirectional liquid spreading *ACS Appl. Mater. Interfaces* **11** 48505–11
- [138] Zhang P F, Chen H W, Li L, Liu H L, Liu G, Zhang L W, Zhang D Y and Jiang L 2017 Bioinspired smart peristome surface for temperature-controlled unidirectional water spreading *ACS Appl. Mater. Interfaces* **9** 5645–52
- [139] Zou M M, Zhang Y, Cai Z R, Li C X, Sun Z Y, Yu C L, Dong Z C, Wu L and Song Y L 2021 3D printing a biomimetic bridge-arch solar evaporator for eliminating salt accumulation with desalination and agricultural applications *Adv. Mater.* **33** 2102443
- [140] Prum R O, Quinn T and Torres R H 2006 Anatomically diverse butterfly scales all produce structural colours by coherent scattering *J. Exp. Biol.* **209** 748–65
- [141] Bixler G D and Bhushan B 2013 Fluid drag reduction and efficient self-cleaning with rice leaf and butterfly wing bioinspired surfaces *Nanoscale* **5** 7685–710
- [142] Tofail S A M, Koumoulos E P, Bandyopadhyay A, Bose S, O'Donoghue L and Charitidis C 2018 Additive manufacturing: scientific and technological challenges, market uptake and opportunities *Mater. Today* **21** 22–37
- [143] Keating S and Oxman N 2013 Compound fabrication: a multi-functional robotic platform for digital design and fabrication *Robot. Comput. Integr. Manuf.* **29** 439–48
- [144] Apsite I, Biswas A, Li Y Q and Ionov L 2020 Microfabrication using shape-transforming soft materials *Adv. Funct. Mater.* **30** 1908028
- [145] Huang S H, Liu P, Mokasdar A and Hou L 2013 Additive manufacturing and its societal impact: a literature review *Int. J. Adv. Manuf. Technol.* **67** 1191–203
- [146] Gao W, Zhang Y B, Ramanujan D, Ramani K, Chen Y, Williams C B, Wang C C L, Shin Y C, Zhang S and Zavattieri P D 2015 The status, challenges, and future of additive manufacturing in engineering *Comput. Aided Des.* **69** 65–89
- [147] Conner B P, Manogharan G P, Martof A N, Rodomsky L M, Rodomsky C M, Jordan D C and Limperos J W 2014 Making sense of 3D printing: creating a map of additive manufacturing products and services *Addit. Manuf.* **1–4** 64–76
- [148] Liu Y, Zhang H, Wang P, He Z Y and Dong G N 2022 3D-printed bionic superhydrophobic surface with petal-like microstructures for droplet manipulation, oil-water separation, and drag reduction *Mater. Des.* **219** 110765
- [149] Truby R L and Lewis J A 2016 Printing soft matter in three dimensions *Nature* **540** 371–8
- [150] Wallin T J, Pikul J and Shepherd R F 2018 3D printing of soft robotic systems *Nat. Rev. Mater.* **3** 84–100
- [151] Wu L, Dong Z C, Cai Z R, Ganapathy T, Fang N X, Li C X, Yu C L, Zhang Y and Song Y L 2020 Highly efficient three-dimensional solar evaporator for high salinity desalination by localized crystallization *Nat. Commun.* **11** 521
- [152] Ge Q, Li Z Q, Wang Z L, Kowsari K, Zhang W, He X N, Zhou J L and Fang N X 2020 Projection micro stereolithography based 3D printing and its applications *Int. J. Extrem. Manuf.* **2** 022004
- [153] Zhang L B, Wu J B, Hedhili M N, Yang X L and Wang P 2015 Inkjet printing for direct micropatterning of a superhydrophobic surface: toward biomimetic fog harvesting surfaces *J. Mater. Chem. A* **3** 2844–52
- [154] Xie M Z, Zhan Z H, Zhang C Q, Xu W Q, Zhang C, Chen Y P, Dong Z C and Wang Z L 2023 Programmable microfluidics enabled by 3D printed bionic Janus porous matrices for microfluidic logic chips *Small* **19** 2300047
- [155] Li N *et al* 2023 Solar-powered interfacial evaporation and deicing based on a 3D-printed multiscale hierarchical design *Small* **19** 2301474
- [156] Amin M, Singh M and Ravi K R 2023 Fabrication of superhydrophobic PLA surfaces by tailoring FDM 3D printing and chemical etching process *Appl. Surf. Sci.* **626** 157217
- [157] Lee K M, Park H, Kim J and Chun D M 2019 Fabrication of a superhydrophobic surface using a fused deposition modeling (FDM) 3D printer with poly lactic acid (PLA) filament and dip coating with silica nanoparticles *Appl. Surf. Sci.* **467–468** 979–91
- [158] Wu C J, Wei X Y, Chen Y T, Liu J, Guo C F, Wang Q B and Liang S Y 2022 Surface wettability analysis and preparation of hydrophobic microcylindrical arrays by  $\mu$ -SLA 3D printing *J. Manuf. Process.* **83** 14–26
- [159] Sun J F, Wang W Q, Liu Z, Li B, Xing K F and Yang Z 2020 Study on selective laser melting 316L stainless steel parts with superhydrophobic surface *Appl. Surf. Sci.* **533** 147445
- [160] Ling Q, Yang L, Tang S Y, Fan Z T, Liu X W and Jiang W M 2022 Direct ink writing of hierarchically porous  $\text{Al}_2\text{O}_3$  matrix composites with enhanced wettability of Al J. *Manuf. Process.* **84** 1580–8
- [161] Wang Y L and Willenbacher N 2022 Phase-change-enabled, rapid, high-resolution direct ink writing of soft silicone *Adv. Mater.* **34** 2109240
- [162] Li Y R, Mao H C, Hu P, Hermes M, Lim H, Yoon O, Luhar M, Chen Y and Wu W 2019 Bioinspired functional surfaces enabled by multiscale stereolithography *Adv. Mater. Technol.* **4** 1800638
- [163] Sun J, Qin X Z, Song Y X, Xu Z Y, Zhang C, Wang W, Wang Z K, Wang B and Wang Z K 2023 Selective liquid directional steering enabled by dual-scale reentrant ratchets *Int. J. Extrem. Manuf.* **5** 025504
- [164] Wang X L, Cai X B, Guo Q Q, Zhang T Y, Kobe B and Yang J 2013 i3DP, a robust 3D printing approach enabling genetic post-printing surface modification *Chem. Commun.* **49** 10064–6
- [165] Dong Z Q, Vuckovac M, Cui W J, Zhou Q, Ras R H A and Levkin P A 2021 3D printing of superhydrophobic objects with bulk nanostructure *Adv. Mater.* **33** 2106068
- [166] Sugioka K and Cheng Y 2014 Ultrafast lasers—reliable tools for advanced materials processing *Light Sci. Appl.* **3** e149
- [167] Yong J L, Fang Y, Chen F, Huo J L, Yang Q, Bian H, Du G Q and Hou X 2016 Femtosecond laser ablated durable superhydrophobic PTFE films with micro-through-holes for oil/water separation: separating oil from water and corrosive solutions *Appl. Surf. Sci.* **389** 1148–55
- [168] Yong J L, Yang Q, Huo J L, Hou X and Chen F 2022 Underwater gas self-transportation along femtosecond laser-written open superhydrophobic surface

- microchannels ( $< 00 \mu\text{m}$ ) for bubble/gas manipulation *Int. J. Extrem. Manuf.* **4** 015002
- [169] Fang Y, Yong J L, Chen F, Huo J L, Yang Q, Zhang J Z and Hou X 2018 Bioinspired fabrication of Bi/tridirectionally anisotropic sliding superhydrophobic PDMS surfaces by femtosecond laser *Adv. Mater. Interfaces* **5** 1701245
- [170] Ta D V, Dunn A, Wasley T J, Kay R W, Stringer J, Smith P J, Connaughton C and Shephard J D 2015 Nanosecond laser textured superhydrophobic metallic surfaces and their chemical sensing applications *Appl. Surf. Sci.* **357** 248–54
- [171] Menon D M N, Giardino M and Janner D 2023 Tunable pulsed nanosecond laser texturing: from environment friendly superhydrophobic to superamphiphobic surfaces *Appl. Surf. Sci.* **610** 155356
- [172] Yang Z, Liu X P and Tian Y L 2018 Insights into the wettability transition of nanosecond laser ablated surface under ambient air exposure *J. Colloid Interface Sci.* **533** 268–77
- [173] Trdan U, Hočevnar M and Gregorčič P 2017 Transition from superhydrophilic to superhydrophobic state of laser textured stainless steel surface and its effect on corrosion resistance *Corros. Sci.* **123** 21–26
- [174] Lian Z X, Xu J K, Yu Z J, Yu P and Yu H D 2019 A simple two-step approach for the fabrication of bio-inspired superhydrophobic and anisotropic wetting surfaces having corrosion resistance *J. Alloys Compd.* **793** 326–35
- [175] Tran N G and Chun D M 2021 Green manufacturing of extreme wettability contrast surfaces with superhydrophilic and superhydrophobic patterns on aluminum *J. Mater. Process. Technol.* **297** 117245
- [176] Zhang J J, Yang D H, Rosenkranz A, Zhang J G, Zhao L, Song C W, Yan Y D and Sun T 2019 Laser surface texturing of stainless steel-effect of pulse duration on texture's morphology and frictional response *Adv. Eng. Mater.* **21** 1801016
- [177] Zhao W Q, Mei X S and Yang Z X 2022 Simulation and experimental study on group hole laser ablation on  $\text{Al}_2\text{O}_3$  ceramics *Ceram. Int.* **48** 4474–83
- [178] Subasi L, Gokler M I and Yaman U 2022 A process modeling approach for micro drilling of aerospace alloys with a waterjet guided laser system *Opt. Laser Technol.* **148** 107682
- [179] Shi Y, Cao J and Ehmann K F 2020 Generation of surfaces with isotropic and anisotropic wetting properties by curved water jet-guided laser micromachining *J. Micro Nano-Manuf.* **8** 041001
- [180] Shi Y, Jiang Z L, Cao J and Ehmann K F 2019 Texturing of metallic surfaces for superhydrophobicity by water jet guided laser micro-machining *Appl. Surf. Sci.* **500** 144286
- [181] Ho K H, Newman S T, Rahimifard S and Allen R D 2004 State of the art in wire electrical discharge machining (WEDM) *Int. J. Mach. Tools Manuf.* **44** 1247–59
- [182] Bae W G, Song K Y, Rahmawan Y, Chu C N, Kim D, Chung D K and Suh K Y 2012 One-step process for superhydrophobic metallic surfaces by wire electrical discharge machining *ACS Appl. Mater. Interfaces* **4** 3685–91
- [183] Yu H D, Lian Z X, Wan Y L, Weng Z K, Xu J K and Yu Z J 2015 Fabrication of durable superamphiphobic aluminum alloy surfaces with anisotropic sliding by HS-WEDM and solution immersion processes *Surf. Coat. Technol.* **275** 112–9
- [184] Chen S H, Wang R, Wu F F, Zhang H L, Gao X F and Jiang L 2021 Copper-based high-efficiency condensation heat transfer interface consisting of superhydrophobic hierarchical microgroove and nanocone structure *Mater. Today Phys.* **19** 100407
- [185] Zhou C L, Wu X Y, Lu Y J, Wu W, Zhao H and Li L J 2018 Fabrication of hydrophobic  $\text{Ti}_3\text{SiC}_2$  surface with micro-grooved structures by wire electrical discharge machining *Ceram. Int.* **44** 18227–34
- [186] Lian Z X, Cheng Y, Xu J K, Xu J L, Ren W F, Tian Y L and Yu H D 2023 Green fabrication of anti-friction slippery liquid-infused metallic surface with sub-millimeter-scale asymmetric bump arrays and its application *Int. J. Precis. Eng. Man-Green Technol.* **10** 1281–98
- [187] Prasad K K, Roy T, Goud M M, Karar V and Mishra V 2021 Diamond turned hierarchically textured surface for inducing water repellency: analytical model and experimental investigations *Int. J. Mech. Sci.* **193** 106140
- [188] Yan J W, Oowada T, Zhou T F and Kuriyagawa T 2009 Precision machining of microstructures on electroless-plated NiP surface for molding glass components *J. Mater. Process. Technol.* **209** 4802–8
- [189] Boswell B, Islam M N and Davies I J 2018 A review of micro-mechanical cutting *Int. J. Adv. Manuf. Technol.* **94** 789–806
- [190] Yu H D, Zhang X R, Wan Y L, Xu J K, Yu Z J and Li Y Q 2016 Superhydrophobic surface prepared by micromilling and grinding on aluminium alloy *Surf. Eng.* **32** 108–13
- [191] Song H, Liu Z Q, Shi Z Y and Cai Y K 2016 Micro-end milling and hydrophobic properties of machined surface for microgroove and microarray *J. Mech. Eng.* **52** 206–12
- [192] Musavi S H, Adibi H and Rezaei S M 2022 Development of an innovative grinding process for producing functional surfaces *Tribol. Int.* **173** 107652
- [193] Zhang S J, To S, Zhu Z W and Zhang G Q 2016 A review of fly cutting applied to surface generation in ultra-precision machining *Int. J. Mach. Tools Manuf.* **103** 13–27
- [194] Yu H Q, Han J G, Li S Y, Han X Z, Liu Y H, Wang J H and Lin J Q 2022 Multi-objective optimization design and performance evaluation of a novel flexure-based tri-axial servo cutting system *J. Manuf. Process.* **84** 1133–49
- [195] Zhang G Q, Ma S, Wang J P, Jiang J K, Luo T and Wang H T 2022 Offset-tool-servo diamond end flycutting multi-layer hierarchical microstructures *Int. J. Mech. Sci.* **233** 107645
- [196] Kurniawan R, Ali S and Ko T J 2020 Measurement of wettability on rhombohedral pattern fabricated by using 3D-UEVT *Measurement* **160** 107784
- [197] Saxena K K, Qian J and Reynaerts D 2018 A review on process capabilities of electrochemical micromachining and its hybrid variants *Int. J. Mach. Tools Manuf.* **127** 28–56
- [198] Xu Z Y and Wang Y D 2021 Electrochemical machining of complex components of aero-engines: developments, trends, and technological advances *Chin. J. Aeronaut.* **34** 28–53
- [199] Zhan D P, Han L H, Zhang J, He Q F, Tian Z-W and Tian Z-Q 2017 Electrochemical micro/nano-machining: principles and practices *Chem. Soc. Rev.* **46** 1526–44
- [200] Yang X L, Song J L, Xu W J, Liu X, Lu Y and Wang Y P 2013 Anisotropic sliding of multiple-level biomimetic rice-leaf surfaces on aluminium substrates *Micro Nano Lett.* **8** 801–4
- [201] Lian Z X, Cheng Y, Liu Z M, Cai Q Q, Tao J, Xu J K, Tian Y L and Yu H D 2023 Scalable fabrication of superhydrophobic armor microstructure arrays with enhanced tribocorrosion performance via maskless electrochemical machining *Surf. Coat. Technol.* **461** 129427
- [202] Sharma V and Chandraprakash C 2022 Quasi-superhydrophobic microscale two-dimensional phononic crystals of stainless steel 304 *J. Appl. Phys.* **131** 184901

- [203] Sato O, Kubo S and Gu Z Z 2009 Structural color films with lotus effects, superhydrophilicity, and tunable stop-bands *Acc. Chem. Res.* **42** 1–10
- [204] Feng L, Li S H, Li H J, Zhai J, Song Y L, Jiang L and Zhu D B 2002 Super-hydrophobic surface of aligned polyacrylonitrile nanofibers *Angew. Chem., Int. Ed.* **41** 1269–71
- [205] Gong D W, Long J Y, Jiang D F, Fan P X, Zhang H J, Li L and Zhong M L 2016 Robust and stable transparent superhydrophobic polydimethylsiloxane films by duplicating via a femtosecond laser-ablated template *ACS Appl. Mater. Interfaces* **8** 17511–8
- [206] Song J L, Huang L, Zhao C L, Wu S, Liu H, Lu Y, Deng X, Carmalt C J, Parkin I P and Sun Y W 2019 Robust superhydrophobic conical pillars from syringe needle shape to straight conical pillar shape for droplet pancake bouncing *ACS Appl. Mater. Interfaces* **11** 45345–53
- [207] Sung J, Lee H M, Yoon G H, Bae S and So H 2023 One-step fabrication of superhydrophobic surfaces with wettability gradient using three-dimensional printing *Int. J. Precis. Eng. Manuf. -Green Technol.* **10** 85–96
- [208] Wang W and Xie Z W 2021 Fabrication of a biomimetic controllable adhesive surface by ultraprecision multistep and layered scribing and casting molding *Sci. China Technol. Sci.* **64** 1814–26
- [209] Kang B, Sung J and So H 2021 Realization of superhydrophobic surfaces based on three-dimensional printing technology *Int. J. Precis. Eng. Manuf.-Green Technol.* **8** 47–55
- [210] Song J L, Gao M Q, Zhao C L, Lu Y, Huang L, Liu X, Carmalt C J, Deng X and Parkin I P 2017 Large-area fabrication of droplet pancake bouncing surface and control of bouncing state *ACS Nano* **11** 9259–67
- [211] Chen L X, Wang X Y, Lu W H, Wu X Q and Li J H 2016 Molecular imprinting: perspectives and applications *Chem. Soc. Rev.* **45** 2137–211
- [212] Guo L J 2004 Recent progress in nanoimprint technology and its applications *J. Phys. D: Appl. Phys.* **37** R123–41
- [213] Becker H and Heim U 2000 Hot embossing as a method for the fabrication of polymer high aspect ratio structures *Sens. Actuators A* **83** 130–5
- [214] Hecke M, Bacher W and Müller K D 1998 Hot embossing—the molding technique for plastic microstructures *Microsyst. Technol.* **4** 122–4
- [215] Yi P Y, Wu H, Zhang C P, Peng L F and Lai X M 2015 Roll-to-roll UV imprinting lithography for micro/nanostructures *J. Vac. Sci. Technol. B* **33** 060801
- [216] Campos L M, Meinel I, Guino R G, Schierhorn M, Gupta N, Stucky G D and Hawker C J 2008 Highly versatile and robust materials for soft imprint lithography based on thiol-ene click chemistry *Adv. Mater.* **20** 3728–33
- [217] van de Groep J, Spinelli P and Polman A 2015 Single-step soft-imprinted large-area nanopatterned antireflection coating *Nano Lett.* **15** 4223–8
- [218] Moon I Y, Kim B H, Lee H W, Oh Y S, Kim J H and Kang S H 2020 Superhydrophobic polymer surface with hierarchical patterns fabricated in hot imprinting process *Int. J. Precis. Eng. Manuf.-Green Technol.* **7** 493–503
- [219] Li A, Li H Z, Li Z, Zhao Z P, Li K X, Li M Z and Song Y L 2020 Programmable droplet manipulation by a magnetic-actuated robot *Sci. Adv.* **6** eaay5808
- [220] You I, Kang S M, Lee S, Cho Y O, Kim J B, Lee S B, Nam Y S and Lee H 2012 Polydopamine microfluidic system toward a two-dimensional, gravity-driven mixing device *Angew. Chem., Int. Ed.* **51** 6126–30
- [221] Dai H Y, Gao C, Sun J H, Li C X, Li N, Wu L, Dong Z C and Jiang L 2019 Controllable high-speed electrostatic manipulation of water droplets on a superhydrophobic surface *Adv. Mater.* **31** 1905449
- [222] Sun Q Q *et al* 2019 Surface charge printing for programmed droplet transport *Nat. Mater.* **18** 936–41
- [223] Xu W H, Jin Y K, Li W B, Song Y X, Gao S W, Zhang B P, Wang L L, Cui M M, Yan X T and Wang Z K 2022 Triboelectric wetting for continuous droplet transport *Sci. Adv.* **8** eade2085
- [224] Jin Y K, Xu W H, Zhang H H, Li R R, Sun J, Yang S Y, Liu M J, Mao H Y and Wang Z K 2022 Electrostatic tweezer for droplet manipulation *Proc. Natl Acad. Sci. USA* **119** e2105459119
- [225] Wang F, Liu M J, Liu C, Zhao Q L, Wang T, Wang Z A K and Du X M 2022 Light-induced charged slippery surfaces *Sci. Adv.* **8** eabp9369
- [226] Sun L Y, Bian F K, Wang Y, Wang Y T, Zhang X X and Zhao Y J 2020 Bioinspired programmable wettability arrays for droplets manipulation *Proc. Natl Acad. Sci. USA* **117** 4527–32
- [227] Zhang J Q, Wang X J, Wang Z Y, Pan S F, Yi B, Ai L Q, Gao J, Mugele F and Yao X 2021 Wetting ridge assisted programmed magnetic actuation of droplets on ferrofluid-infused surface *Nat. Commun.* **12** 7136
- [228] Jing X S, Chen H W, Zhang L W, Zhao S, Wang Y, Wang Z L L and Zhou Y 2023 Accurate magneto-driven multi-dimensional droplet manipulation *Adv. Funct. Mater.* **33** 2210883
- [229] Nasirimarekani V, Benito-Lopez F and Basabe-Desmonts L 2021 Tunable superparamagnetic ring (tSPRing) for droplet manipulation *Adv. Funct. Mater.* **31** 2100178
- [230] Zhang Y Y *et al* 2022 A biocompatible vibration-actuated omni-droplets rectifier with large volume range fabricated by femtosecond laser *Adv. Mater.* **34** 2108567
- [231] Song Y G *et al* 2020 Cross-species bioinspired anisotropic surfaces for active droplet transportation driven by unidirectional microcolumn waves *ACS Appl. Mater. Interfaces* **12** 42264–73
- [232] Cao M Y, Jin X, Peng Y, Yu C M, Li K, Liu K S and Jiang L 2017 Unidirectional wetting properties on multi-bioinspired magnetocontrollable slippery microcilia *Adv. Mater.* **29** 1606869
- [233] Lee S H, Seong M, Kwak M K, Ko H, Kang M, Park H W, Kang S M and Jeong H E 2018 Tunable multimodal drop bouncing dynamics and anti-icing performance of a magnetically responsive hair array *ACS Nano* **12** 10693–702
- [234] Jiang S J *et al* 2020 Three-dimensional multifunctional magnetically responsive liquid manipulator fabricated by femtosecond laser writing and soft transfer *Nano Lett.* **20** 7519–29
- [235] Shao K X, Jiang S J, Hu Y L, Zhang Y Y, Li C Z, Zhang Y X, Li J W, Wu D and Chu J R 2022 Bioinspired lubricated slippery magnetic responsive microplate array for high performance multi-substance transport *Adv. Funct. Mater.* **32** 2205831
- [236] Lv C J, Chen C, Chuang Y C, Tseng F G, Yin Y J, Grey F and Zheng Q S 2014 Substrate curvature gradient drives rapid droplet motion *Phys. Rev. Lett.* **113** 026101
- [237] Bird J C, Dhiman R, Kwon H M and Varanasi K K 2013 Reducing the contact time of a bouncing drop *Nature* **503** 385–8
- [238] Li H Z, Fang W, Li Y A, Yang Q, Li M Z, Li Q Y, Feng X Q and Song Y L 2019 Spontaneous droplets gyrating via asymmetric self-splitting on heterogeneous surfaces *Nat. Commun.* **10** 950
- [239] Tao R, Liang G Q, Dou B H, Wu J, Li B and Hao C L 2022 Oblique pancake bouncing *Cell Rep. Phys. Sci.* **3** 100721
- [240] Zhang X X, Sun L Y, Wang Y, Bian F K, Wang Y T and Zhao Y J 2019 Multibioinspired slippery surfaces with wettability bump arrays for droplets pumping *Proc. Natl Acad. Sci. USA* **116** 20863–8



- [241] Bai H Y, Wang X S, Li Z, Wen H Y, Yang Y F, Li M Q and Cao M Y 2023 Improved liquid collection on a dual-asymmetric superhydrophilic origami *Adv. Mater.* **35** 2211596
- [242] Li D K, Fan Y F, Han G C and Guo Z G 2021 Multibioinspired Janus membranes with superwetable performance for unidirectional transportation and fog collection *Chem. Eng. J.* **404** 126515
- [243] Zhang M, Zheng Z Y, Zhu Y Q, Zhu Z Q, Si T and Xu R X 2022 Combinational biomimetic microfibers for high-efficiency water collection *Chem. Eng. J.* **433** 134495
- [244] Liu H Y, Wang Y Y, Yin W, Yuan H, Guo T and Meng T 2022 Highly efficient water harvesting of bioinspired spindle-knotted microfibers with continuous hollow channels *J. Mater. Chem. A* **10** 7130–7
- [245] Shi Y, Ilic O, Atwater H A and Greer J R 2021 All-day fresh water harvesting by microstructured hydrogel membranes *Nat. Commun.* **12** 2797
- [246] Shannon M A, Bohn P W, Elimelech M, Georgiadis J G, Mariñas B J and Mayes A M 2008 Science and technology for water purification in the coming decades *Nature* **452** 301–10
- [247] Lin Q Q, Zeng G Y, Pu S Y, Yan G L, Luo J Q, Wan Y H and Zhao Z Y 2022 A dual regulation strategy for MXene-based composite membrane to achieve photocatalytic self-cleaning properties and multi-functional applications *Chem. Eng. J.* **443** 136335
- [248] Gupta R K, Dunderdale G J, England M W and Hozumi A 2017 Oil/water separation techniques: a review of recent progresses and future directions *J. Mater. Chem. A* **5** 16025–58
- [249] Yang Y, Ren Z Y, Zhou C H, Lin Y X, Hou L X, Shi L W and Zhong S C 2023 3D-printed robust dual superlyophobic Ti-based porous structure for switchable oil/water emulsion separations *Adv. Funct. Mater.* **33** 2212262
- [250] Shi Z *et al* 2023 Constructing superhydrophobicity by self-assembly of SiO<sub>2</sub>@polydopamine core-shell nanospheres with robust oil-water separation efficiency and anti-corrosion performance *Adv. Funct. Mater.* **33** 2213042
- [251] Li C X, Wu L, Yu C L, Dong Z C and Jiang L 2017 Peristome-mimetic curved surface for spontaneous and directional separation of micro water-in-oil drops *Angew. Chem., Int. Ed.* **56** 13623–8
- [252] Chen Y, Quan Z J, Song W D, Wang Z, Li B, Mu Z Z, Niu S C, Zhang J Q, Han Z W and Ren L Q 2022 Hierarchically structured biomimetic membrane with mechanically/chemically durability and special wettability for highly efficient oil-water separation *Sep. Purif. Technol.* **300** 121860
- [253] Qin Z L, Xiang H Q, Liu J G and Zeng X Y 2019 High-performance oil-water separation polytetrafluoroethylene membranes prepared by picosecond laser direct ablation and drilling *Mater. Des.* **184** 108200
- [254] Bae W G, Kim D, Song K Y, Jeong H E and Chu C N 2015 Engineering stainless steel surface via wire electrical discharge machining for controlling the wettability *Surf. Coat. Technol.* **275** 316–23
- [255] Tian G Z, Fan D L, Feng X M and Zhou H G 2021 Thriving artificial underwater drag-reduction materials inspired from aquatic animals: progresses and challenges *RSC Adv.* **11** 3399–428
- [256] Lee C, Choi C H and Kim C J 2016 Superhydrophobic drag reduction in laminar flows: a critical review *Exp. Fluids* **57** 176
- [257] Qin L G, Hafezi M, Yang H, Dong G N and Zhang Y L 2019 Constructing a dual-function surface by microcasting and nanospraying for efficient drag reduction and potential antifouling capabilities *Micromachines* **10** 490
- [258] Abolghasemibizaki M, Robertson C J, Fergusson C P, McMasters R L and Mohammadi R 2018 Rolling viscous drops on a non-wettable surface containing both micro- and macro-scale roughness *Phys. Fluids* **30** 023105
- [259] Kim M, Yoo S, Jeong H E and Kwak M K 2022 Fabrication of *Salvinia*-inspired surfaces for hydrodynamic drag reduction by capillary-force-induced clustering *Nat. Commun.* **13** 5181
- [260] Wang Y H, Zhang Z B, Xu J K and Yu H D 2021 One-step method using laser for large-scale preparation of bionic superhydrophobic & drag-reducing fish-scale surface *Surf. Coat. Technol.* **409** 126801
- [261] Rong W T, Zhang H F, Zhang T J, Mao Z G, Liu X W and Song K G 2021 Drag reduction using lubricant-impregnated anisotropic slippery surfaces inspired by bionic fish scale surfaces containing micro-/nanostructured arrays *Adv. Eng. Mater.* **23** 2000821
- [262] Mishchenko L, Hatton B, Bahadur V, Taylor J A, Krupenkin T and Aizenberg J 2010 Design of ice-free nanostructured surfaces based on repulsion of impacting water droplets *ACS Nano* **4** 7699–707
- [263] Chen H Y, Wang F F, Fan H Z, Hong R Y and Li W H 2021 Construction of MOF-based superhydrophobic composite coating with excellent abrasion resistance and durability for self-cleaning, corrosion resistance, anti-icing, and loading-increasing research *Chem. Eng. J.* **408** 127343
- [264] Chen C H, Tian Z, Luo X, Jiang G C, Hu X Y, Wang L Z, Peng R, Zhang H J and Zhong M L 2022 Cauliflower-like micro-nano structured superhydrophobic surfaces for durable anti-icing and photothermal de-icing *Chem. Eng. J.* **450** 137936
- [265] Wang L Z, Jiang G C, Tian Z, Chen C H, Hu X Y, Peng R, Zhang H J, Fan P X and Zhong M L 2023 Superhydrophobic microstructures for better anti-icing performances: open-cell or closed-cell? *Mater. Horiz.* **10** 209–20
- [266] Lu C G, Liu C, Yuan Z C, Zhan H Y, Zhao D Y, Zhao L, Feng S L and Liu Y H 2022 Gradient droplet distribution promotes spontaneous formation of frost-free zone *Commun. Mater.* **3** 80
- [267] Ma C, Chen L, Wang L, Tong W, Chu C L, Yuan Z P, Lv C J and Zheng Q S 2022 Condensation droplet sieve *Nat. Commun.* **13** 5381
- [268] Miljkovic N, Enright R, Nam Y, Lopez K, Dou N, Sack J and Wang E N 2013 Jumping-droplet-enhanced condensation on scalable superhydrophobic nanostructured surfaces *Nano Lett.* **13** 179–87
- [269] Mulroe D M, Srijanto B R, Ahmadi S F, Collier C P and Boreyko J B 2017 Tuning superhydrophobic nanostructures to enhance jumping-droplet condensation *ACS Nano* **11** 8499–510
- [270] Li Z L, Li W W, Xun M and Yuan M C 2023 WEDM one-step preparation of miniature heat sink with superhydrophobic and efficient heat transfer performance *Int. J. Adv. Manuf. Technol.* **127** 1873–85
- [271] Du J Y, Li Y Z, Wang X, Wu X X and Min Q 2023 Dynamics and heat transfer of water droplets impacting on heated surfaces: the role of surface structures in Leidenfrost point *Int. J. Heat Mass Transfer* **212** 124241
- [272] Wang X L, Xu J, Jiang H P, Liu Y D, Li X R, Shan D B and Guo B 2023 Achieving robust and enhanced pool boiling heat transfer using micro-nano multiscale structures *Appl. Therm. Eng.* **227** 120441
- [273] Tang Y, Yang X L, Wang L G, Li Y M and Zhu D 2023 Dropwise condensate comb for enhanced heat transfer *ACS Appl. Mater. Interfaces* **15** 21549–61

- [274] Wan Z P, Hu X S, Wang X W and He Z C 2023 Experimental study on the boiling/condensation heat transfer performance of a finned tube with a hydrophilic/hydrophobic surface *Appl. Therm. Eng.* **229** 120494
- [275] Feng L, Zhang Z Y, Mai Z H, Ma Y M, Liu B Q, Jiang L and Zhu D B 2004 A super-hydrophobic and super-oleophilic coating mesh film for the separation of oil and water *Angew. Chem., Int. Ed.* **43** 2012–4
- [276] Kim D H, Kim S, Park S R, Fang N X and Cho Y T 2021 Shape-deformed mushroom-like reentrant structures for robust liquid-repellent surfaces *ACS Appl. Mater. Interfaces* **13** 33618–26
- [277] Zhao Y, Qin M L, Wang A J and Kim D 2013 Bioinspired superhydrophobic carbonaceous hairy microstructures with strong water adhesion and high gas retaining capability *Adv. Mater.* **25** 4561–5
- [278] Han X, Liu J N, Wang M Y, Upmanyu M and Wang H L 2022 Second-level microgroove convexity is critical for air plastron restoration on immersed hierarchical superhydrophobic surfaces *ACS Appl. Mater. Interfaces* **14** 52524–34
- [279] Wang J N, Liu Y Q, Zhang Y L, Feng J and Sun H B 2018 Pneumatic smart surfaces with rapidly switchable dominant and latent superhydrophobicity *NPG Asia Mater.* **10** e470
- [280] Wang H J, Zhang Z H, Zheng J, Zhao J, Liang Y H, Li X J and Ren L Q 2021 Multifunctional superhydrophobic surface with dynamically controllable micro/nanostructures for droplet manipulation and friction control *Chem. Eng. J.* **417** 127944
- [281] Jiao Y L, Li C Z, Ji J W, Wang Z C, Tao T T, Zhang T and Liu K 2021 Femtosecond laser-induced shape memory polymer micropillar with tunable wettability and reversible adhesion for underwater oil droplet lossless transfer *Appl. Phys. Lett.* **118** 033701
- [282] Bai X, Yang Q, Fang Y, Yong J L, Bai Y K, Zhang J W, Hou X and Chen F 2020 Anisotropic, adhesion-switchable, and thermal-responsive superhydrophobicity on the femtosecond laser-structured shape-memory polymer for droplet manipulation *Chem. Eng. J.* **400** 125930
- [283] Zhang X H, Liu J, Xia M and Hu Y W 2023 Laser shock peening enables 3D gradient metal structures: a case study on manufacturing self-armored hydrophobic surfaces *Int. J. Mach. Tools Manuf.* **185** 103993
- [284] Huovinen E, Takkunen L, Korpela T, Suvanto M, Pakkanen T T and Pakkanen T A 2014 Mechanically robust superhydrophobic polymer surfaces based on protective micropillars *Langmuir* **30** 1435–43
- [285] Verho T, Bower C, Andrew P, Franssila S, Ikkala O and Ras R H A 2011 Mechanically durable superhydrophobic surfaces *Adv. Mater.* **23** 673–8
- [286] Jiao Z B *et al* 2020 Underwater writable and heat-insulated paper with robust fluorine-free superhydrophobic coatings *Nanoscale* **12** 8536–45
- [287] Chen F Z, Wang Y Q, Tian Y L, Zhang D W, Song J L, Crick C R, Carmalt C J, Parkin I P and Lu Y 2022 Robust and durable liquid-repellent surfaces *Chem. Soc. Rev.* **51** 8476–583